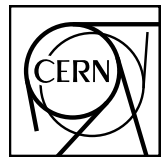


EUROPEAN ORGANIZATION FOR NUCLEAR RESEARCH

1



ALICE-ANA-2020-1008
April 20, 2020

2

3

First measurement of coherent J/ Ψ polarisation in Pb–Pb UPC events at $\sqrt{s_{\text{NN}}} = 5.02 \text{ TeV}$

4

5

Simone Ragoni¹, Orlando Villalobos Baillie¹

6

1. University of Birmingham, United Kingdom

7

Email: simone.ragoni@cern.ch; orlando.villalobos.baillie@cern.ch

8

Abstract

9

10

11

12

In this document we describe the measurement of the polarisation of coherent J/ Ψ in Pb–Pb UPC events at $\sqrt{s_{\text{NN}}} = 5.02 \text{ TeV}$. This will be possible thanks to the Forward Muon Spectrometer. The analysis is done in two reference frames, Helicity and Collins-Soper, by studying the process $J/\Psi \rightarrow \mu^+ \mu^-$.

13 Contents

14	1 Physics Motivation	3
15	2 Analysis Summary	5
16	2.1 Analysis rationale and strategy	5
17	2.2 Datasets	5
18	2.3 Monte Carlo	5
19	2.4 Detectors Included	5
20	3 Datasets and Event Selection	6
21	3.1 Pb–Pb analysis: dataset	6
22	3.2 Monte Carlo in Pb–Pb	7
23	3.3 Trigger selections	7
24	3.4 Track selections	7
25	4 Invariant Mass Fits	9
26	5 Invariant Mass Fits for 1D signal extraction in the Helicity frame	10
27	5.1 CosTheta	10
28	5.2 Phi	15
29	5.3 TildePhi	20
30	5.4 Combined fits	25
31	6 Invariant Mass Fits for 1D signal extraction in the Collins-Soper frame	26
32	6.1 CosTheta	26
33	6.2 Phi	30
34	6.3 TildePhi	35
35	6.4 Combined fits	40
36	7 Systematics for the 1D analysis	41
37	7.1 Helicity Frame	41
38	7.2 Collins Soper Frame	44
39	8 Conclusions	47
40	A Invariant Mass Fits for 2D signal extraction in the Helicity frame	49
41	A.1 Yield extraction for the 2D analysis	52

42	B Invariant Mass Fits for 2D signal extraction in the Collins-Soper frame	66
43	B.1 Yield extraction for the 2D analysis	70

44 **1 Physics Motivation**

45 In ultraperipheral collisions (UPC), two nuclei pass close to each other, but with an impact parameter
 46 larger than the sum of their radii. A photon emitted by one of the nuclei can fluctuate into a $q\bar{q}$ pair
 47 with very low virtuality [1], and this interacts with the other nucleus without breaking it up. The $q\bar{q}$ pair
 48 becomes a J/Ψ, which is expected to have the same polarization as the original photon, namely transverse
 49 polarization. While there have been some studies of vector meson polarization in the analogous process
 50 of exclusive vector meson production in ep interactions, there are as yet no results from UPC in heavy
 51 ions.

52 This analysis note describes the details of a measurement of the coherent J/Ψ polarisation, in Pb–Pb UPC
 53 events at a centre-of-mass-energy of $\sqrt{s_{NN}} = 5.02$ TeV, where we have close to twentytwo thousand
 54 coherent J/Ψ candidates [2].

55 The photon has quantum numbers $J^{PC} = 1^{--}$. In virtue of the Generalised Vector Dominance Model
 56 (GVDM), together with the Colour Dipole view, the photon is favoured to transition to a vector meson.
 57 As a vector meson, the J/Ψ can be produced in three states of the total angular momentum J with third
 58 component J_z [3]:

$$|J, J_z\rangle [\text{J}/\Psi] = b_{-1} \cdot |1, -1\rangle + b_0 \cdot |1, 0\rangle + b_{+1} \cdot |1, +1\rangle , \quad (1)$$

59 where two main states are possible:

- 60 – $b_0 = 1$ and $b_{\pm 1} = 0$ if longitudinally polarised;
 61 – $b_0 = 0$ and $b_{-1}^2 + b_{+1}^2 = 1$ if transversely polarised.

62 In this analysis, two reference frames will be used, which differ in their z -axis definition:

- 63 – **Helicity frame:** flight direction of the J/Ψ in the laboratory frame;
 64 – **Collins-Soper:** the bisector of the angle between the beam and the opposite of the other beam in
 65 the J/Ψ rest frame.

66 In both cases, the y -axis is perpendicular to the plane formed by the collision axis and the direction of
 67 the J/Ψ in the laboratory frame, while the x -axis is chosen accordingly as to have a right-handed triplet
 68 [4].

69 The distributions obtained with these definitions are corrected for acceptance and efficiency ($A \times \epsilon$), and
 70 then fitted with the following function (in case of a 2D fit) [5]:

$$W(\cos(\theta), \phi) \propto \frac{1}{3 + \lambda_\theta} \cdot [1 + \lambda_\theta \cdot \cos^2 \theta + \lambda_\phi \cdot \sin^2 \theta \cdot \cos(2\phi) + \lambda_{\theta\phi} \cdot \sin(2\phi)] . \quad (2)$$

The analysis can also be done with the 1D projections. However, in this case it would be more difficult
 to obtain the third parameter $\lambda_{\theta\phi}$. To get round this, a third variable, $\tilde{\phi}$, is defined as follows [3]:

$$\tilde{\phi} = \begin{cases} \phi - \frac{3}{4} \cdot \pi & \text{if } \cos \theta < 0, \\ \phi - \frac{1}{4} \cdot \pi & \text{otherwise.} \end{cases}$$

71 When $\tilde{\phi}$ is less than zero, 2π is added to the value.

⁷² The three distributions in $\cos \theta$, ϕ and $\tilde{\phi}$ are obtained and corrected for the corresponding $A \times \epsilon$, and are
⁷³ then fitted with the corresponding 1D functions [3]:

$$\begin{aligned} W(\cos \theta) &\propto \frac{1}{3 + \lambda_\theta} \cdot [1 + \lambda_\theta \cdot \cos^2 \theta] \\ W(\phi) &\propto 1 + \frac{2\lambda_\phi}{3 + \lambda_\theta} \cdot \cos 2\phi \\ W(\tilde{\phi}) &\propto 1 + \frac{\sqrt{2}\lambda_{\theta\phi}}{3 + \lambda_\theta} \cdot \cos \tilde{\phi}. \end{aligned} \quad (3)$$

⁷⁴ Three cases are of particular interest and are summarised here:

- ⁷⁵ – $(\lambda_\theta, \lambda_\phi, \lambda_{\theta\phi}) = (0, 0, 0,)$ —> no polarisation at all;
- ⁷⁶ – $(\lambda_\theta, \lambda_\phi, \lambda_{\theta\phi}) = (-1, 0, 0,)$ —> longitudinal polarisation;
- ⁷⁷ – $(\lambda_\theta, \lambda_\phi, \lambda_{\theta\phi}) = (1, 0, 0,)$ —> transverse polarisation.

⁷⁸ As the p_T threshold for the analysis is at 0.25 GeV/c i.e. only dimuons with $p_T < 0.25$ GeV/c are
⁷⁹ considered. Note that in exclusive photoproduction the process being considered is $\gamma N \rightarrow J/\psi N$, so,
⁸⁰ formally, the directions of the photon and the nucleus should be evaluated in this frame to determine the
⁸¹ y axis (both helicity and Collins-Soper frames), and the γ and the nucleus used to determine the z axis
⁸² (Collins-Soper frame). In ALICE, the direction of the incoming photon is not known; however, as the p_T
⁸³ of the photon with respect to the beam axis is very small, the gamma and the emitting nucleus will have
⁸⁴ similar directions, as will the γ and the J/ψ . As a result, in these circumstances the two sets of axes give
⁸⁵ similar distributions.

86 **2 Analysis Summary**

87 **2.1 Analysis rationale and strategy**

88 This analysis note describes the strategy and techniques used to measure the coherent J/ Ψ polarisation in
89 Pb–Pb UPC events at $\sqrt{s_{\text{NN}}} = 5.02$ TeV. The analysis mainly uses the Forward Muon Spectrometer to
90 study the angular distributions of the muons resulting from the decay of the vector meson.

91

92 **2.2 Datasets**

- 93 – Pb–Pb dataset;
94 – LHC15o_muoncalo_pass1 (nanoAODs): collected in 2015;
95 – LHC18q_muoncalo_pass3 (nanoAODs): collected in 2018;
96 – LHC18r_muoncalo_pass3 (nanoAODs): collected in 2018

97 **2.3 Monte Carlo**

- 98 – Monte Carlo for Pb–Pb generated with STARlight: LHC16b2 and LHC18I7, anchored to the cor-
99 responding runs.

100 **2.4 Detectors Included**

- 101 – **SPD**;
102 – **Forward Muon Spectrometer**;
103 – **V0**;
104 – **AD**;
105 – **ZDC**.

¹⁰⁶ **3 Datasets and Event Selection**

¹⁰⁷ **3.1 Pb–Pb analysis: dataset**

¹⁰⁸ The relevant detectors are as follows: AD, V0, ZDC, SPD, MTR, MTK. Information on the muon QA
¹⁰⁹ can be found elsewhere, e.g. <https://twiki.cern.ch/twiki/bin/view/ALICE/MuonPbPbQA2015>.
¹¹⁰ A few runs were discarded because of low voltage trips in the MUON chambers. Since the information
¹¹¹ regarding a LV trip is not propagated, one would end up with the Monte Carlo simulation not reproducing
¹¹² the data. This could be recovered in future passes by killing the concerned regions, both in raw data
¹¹³ reconstruction and in Monte Carlo generated data. A total number of 361 runs from LHC15o, LHC18q
¹¹⁴ and LHC18r periods have been considered. They are as follows:

¹¹⁵ – **LHC15o:**

```
116
118 244980, 244982, 244983, 245064, 245066, 245068, 245145, 245146, 245151,
119 245152, 245231, 245232, 245233, 245253, 245259, 245343, 245345, 245346,
120 245347, 245353, 245401, 245407, 245409, 245410, 245446, 245450, 245496,
121 245501, 245504, 245505, 245507, 245535, 245540, 245542, 245543, 245554,
122 245683, 245692, 245700, 245705, 245729, 245731, 245738, 245752, 245759,
123 245766, 245775, 245785, 245793, 245829, 245831, 245833, 245949, 245952,
124 245954, 245963, 245996, 246001, 246003, 246012, 246036, 246037, 246042,
125 246048, 246049, 246053, 246087, 246089, 246113, 246115, 246148, 246151,
126 246152, 246153, 246178, 246181, 246182, 246217, 246220, 246222, 246225,
127 246272, 246275, 246276, 246390, 246391, 246392, 246424, 246428, 246431,
128 246433, 246434, 246487, 246488, 246493, 246495, 246675, 246676, 246750,
129 246751, 246755, 246757, 246758, 246759, 246760, 246763, 246765, 246804,
130 246805, 246806, 246807, 246808, 246809, 246844, 246845, 246846, 246847,
131 246851, 246855, 246859, 246864, 246865, 246867, 246871, 246930, 246937,
132 246942, 246945, 246948, 246949, 246980, 246982, 246984, 246989, 246991,
133 246994
135
```

¹³⁶ – **LHC18q:**

```
137
138 295585, 295586, 295587, 295588, 295589, 295612, 295615, 295665, 295666,
139 295667, 295668, 295671, 295673, 295675, 295676, 295677, 295714, 295716,
140 295717, 295718, 295719, 295723, 295725, 295753, 295754, 295755, 295758,
141 295759, 295762, 295763, 295786, 295788, 295791, 295816, 295818, 295819,
142 295822, 295825, 295826, 295829, 295831, 295854, 295855, 295856, 295859,
143 295860, 295861, 295863, 295881, 295908, 295909, 295910, 295913, 295936,
144 295937, 295941, 295942, 295943, 295945, 295947, 296061, 296062, 296063,
145 296065, 296066, 296068, 296123, 296128, 296132, 296133, 296134, 296135,
146 296142, 296143, 296191, 296192, 296194, 296195, 296196, 296197, 296198,
147 296241, 296242, 296243, 296244, 296246, 296247, 296269, 296270, 296273,
148 296279, 296280, 296303, 296304, 296307, 296309, 296312, 296377, 296378,
149 296379, 296380, 296381, 296383, 296414, 296419, 296420, 296423, 296424,
150 296433, 296472, 296509, 296510, 296511, 296514, 296516, 296547, 296548,
151 296549, 296550, 296551, 296552, 296553, 296615, 296616, 296618, 296619,
152 296622, 296623
153
```

¹⁵⁶ – **LHC18r:**

```

157
159 296690, 296691, 296694, 296749, 296750, 296781, 296784, 296785, 296786,
160 296787, 296791, 296793, 296794, 296799, 296836, 296838, 296839, 296848,
161 296849, 296850, 296851, 296852, 296890, 296894, 296899, 296900, 296903,
162 296930, 296931, 296932, 296934, 296935, 296938, 296941, 296966, 296967,
163 296968, 296969, 296971, 296975, 296976, 296979, 297029, 297031, 297035,
164 297085, 297117, 297118, 297119, 297123, 297124, 297128, 297129, 297132,
165 297133, 297193, 297194, 297196, 297218, 297219, 297221, 297222, 297278,
166 297310, 297312, 297315, 297317, 297363, 297366, 297367, 297372, 297379,
167 297380, 297405, 297408, 297413, 297414, 297415, 297441, 297442, 297446,
168 297450, 297451, 297452, 297479, 297481, 297483, 297512, 297537, 297540,
169 297541, 297542, 297544, 297558, 297588, 297590, 297595
170

```

172 3.2 Monte Carlo in Pb–Pb

173 The Monte Carlo productions dedicated to the Pb–Pb data used in the analysis are the following:

```

174
175 LHC16b2, LHC1817
176
177

```

179 3.3 Trigger selections

180 The following trigger classes were used in the analysis:

```

181 CMUP10-B-NOPF-MUFAST = OMSL & !OUBA & !OUBC & !OVBA - runs 244980-245542
182 CMUP11-B-NOPF-MUFAST = OMUL & !OUBA & !OUBC & !OVBA - runs 245543-297595
183 CMUP13-B-NOPF-MUFAST = OMUL & !OUBA & !OUBC - runs 246844-246994
184 CMUP26-B-NOPF-MUFAST = OMUL & !OUBA & !OUBC & !OVBA - runs 295585-297595
185 CMUP6-B-NOPF-MUFAST = OMUL & !OVBA - runs 295585-297595

```

186 where

- 187 – OMSL: low- p_T single muon trigger;
- 188 – OMUL: low- p_T unlike-single dimuon trigger;
- 189 – OVBA: at least one cell in V0A with beam-beam timing;
- 190 – OUBA: at least one quarter in ADA with beam-beam timing;
- 191 – OUBC: at least one quarter in ADC with beam-beam timing;

192 The low- p_T trigger threshold for single muon tracks was set to 1 GeV/c (i.e. 1 GeV/c corresponds to
193 about 50% trigger efficiency).

194 3.4 Track selections

195 The global selections applied to the candidate events, triggered by CMUP10 or CMUP11 triggers, are
196 as follows. The AD detectors on either side are vetoed offline to improve the quality of the online
197 trigger. The offline decisions for the V0 detectors are that the V0A (opposite direction to the Muon
198 Spectrometer) was empty, and that the V0C (in front of the muon arm) was either empty or had any
199 remaining activity with timing corresponding to beam-beam events. This is because the rapidity range of
200 the muon spectrometer is slightly wider than that of V0C, so it is possible for muons to miss the V0C but
201 still be detected in the muon arm. There should be a maximum of two hits in the V0C since there should

only be two muons. We apply a requirement that there can be no tracklets in the SPD, since we expect no activity in the central region. The inefficiency for this veto is significant (8.3%-9.5%). Therefore it was chosen to perform two analyses: without SPD tracklet cut (leaving possible non-UPC contribution) and with SPD tracklet cut to keep the sample clean, with the inefficiency taken into account later with the eff_{veto} correction to the final cross section. The final global selection applied is that there should be exactly two muons detected in the muon spectrometer.

Requirements are also applied for individual tracks. The pseudorapidity of each muon track should be within the range $-4.0 < \eta_{\mu} < -2.5$ so that it is in the acceptance region of the muon spectrometer. The radial position of each track at the entrance to the absorber, R_{abs} , should lie within the range $17.5 \text{ cm} < R_{\text{abs}} < 89.5 \text{ cm}$ to ensure that they pass through the absorber's homogeneous region. Each track detected in the muon tracking chamber should be matched to a track detected in the muon trigger chamber. The momentum multiplied by the distance of closest approach of each track to the interaction point, $p \times \text{DCA}$, should be below the set threshold to remove beam-induced background. Selections made for dimuons, i.e. a pair of tracks, are the following. The two tracks should have opposite electric charges, as expected for both $J/\Psi \rightarrow \mu^+ \mu^-$ and $\gamma\gamma \rightarrow \mu^+ \mu^-$. The rapidity of the dimuon should be in the range $-4.0 < y_{\mu\mu} < -2.5$ so that it is in the acceptance region of the muon spectrometer. The dimuon should have a transverse momentum of $p_T < 250 \text{ MeV}/c$, since coherent events are expected to produce J/Ψ with transverse momenta generally lower than this, whilst the majority of the incoherent events, which have on average higher transverse momenta, are removed by this cut.

The selections are summarised as follows:

- ADA, ADC offline veto;
- V0A offline veto;
- V0C empty or in beam timing;
- Maximum of two hits in the V0C;
- Zero SPD tracklets (in case of analysis with SPD tracklet cut);
- Exactly two muons;
- Opposite-sign muons;
 - $-4.0 < \eta_{\mu} < -2.5$;
 - $17.5 \text{ cm} < R_{\text{abs}} < 89.5 \text{ cm}$;
- Muon track matched to muon trigger;
- $p \times \text{DCA}$ criterion for each muon passed;
 - $-4.0 < y_{\mu\mu} < -2.5$;
 - $p_T^{\mu\mu} < 0.25 \text{ GeV}/c$;

235 **4 Invariant Mass Fits**

236 The effective mass distributions are fitted using three functions. The two resonances, the J/Ψ and the
 237 Ψ(2S), were fitted using the Crystal Ball function [6]:

$$CB(M_{\mu\mu}) = \begin{cases} |M_{\mu\mu} - M_1|^{-n} & \text{if } M_{\mu\mu} < M_0 - \sigma \cdot \alpha, \\ \frac{1}{\sqrt{2\pi}\cdot\sigma} \cdot \exp\left[-\frac{(M_{\mu\mu} - M_0)^2}{2\sigma^2}\right] & \text{otherwise.} \end{cases} \quad (4)$$

238 where σ is the width parameter and α the number of widths below the resonance peak that the function
 239 changes form. In fitting the J/Ψ and Ψ(2S) peaks in the data, the α and n parameters were fixed from fits
 240 to the respective generated data sets produced using the STARlight generator. The M_0 parameter for J/Ψ
 241 was left free in the fit to data. The parameter σ was left free for the J/Ψ, and was fixed for the Ψ(2S) to
 242 σ for the J/Ψ multiplied by the ratio of the widths of the Ψ(2S) to the J/Ψ in STARlight (approximately
 243 1.09). It is justifiable to use these functions on the raw versions of these spectra as they cover relatively
 244 narrow intervals in $\mu^+\mu^-$ effective mass over which there should be negligible changes in acceptance
 245 and efficiency.

246 At high effective masses, the shape of the background is essentially exponential, as expected if it is
 247 dominated by the process $\gamma\gamma \rightarrow \mu^+\mu^-$. However, at masses below the J/Ψ it does not follow this
 248 shape, as the distribution is strongly influenced by the trigger condition. In order to model this, the
 249 whole background distribution has been fitted using a template made from generated and reconstructed
 250 STARlight events corresponding to the process $\gamma\gamma \rightarrow \mu^+\mu^-$, with the trigger conditions applied. The
 251 results of the fit are used in a fourth-order polynomial with a specific template considered for each
 252 polarisation bin, which fits smoothly onto the exponential tail as from 4 GeV/c, i.e.

$$P(M_{\mu\mu}) = \begin{cases} \exp(b \cdot M_{\mu\mu}) \cdot [1 + a_2 \cdot (M_{\mu\mu} - M_{th})^2 + a_3 \cdot (M_{\mu\mu} - M_{th})^3 + a_4 \cdot (M_{\mu\mu} - M_{th})^4 +] & \text{if } M_{\mu\mu} < M_{th}, \\ \exp(b \cdot M_{\mu\mu}) & \text{otherwise.} \end{cases}$$

253 where $M_{th} = 4$ GeV/c.

254 The coefficients a_i of the polynomial are fitted using a sample of $\gamma\gamma \rightarrow \mu^+\mu^-$ events generated by
 255 STARlight, subject to the UPC trigger conditions. These coefficients are then kept fixed in the fit to the
 256 experimental data. Only the slope b of the exponential term is left free, and the fitted slope is found to
 257 be very close in value to that found in the generated sample.

258 **5 Invariant Mass Fits for 1D signal extraction in the Helicity frame**

259 **5.1 CosTheta**

260 The binning for this analysis was chosen so as to have well populated bins and to mitigate the bin
 261 migration effect. The bin migration effect is evaluated using STARlight data, as shown in Fig. 1. The
 262 plot shows the $\cos \theta_{\text{reconstructed}} \text{ vs } \cos \theta_{\text{generated}}$. The purity is plotted as well. As expected, the purity
 263 increases as the binning gets coarser. To achieve a purity at the level of at least 80% for the analysis,
 264 twenty five equal sized bins have been chosen for each of the $\cos \theta$, ϕ and $\tilde{\phi}$ distributions.

265 The yields are extracted using the formalism introduced earlier in this document. Note that out of the
 266 twenty five bins, only fifteen bins could undergo the procedure due to acceptance problems, as shown in
 267 Figs. 2(a), 2(b), 2(c), 2(d), 2(e), 2(f), 2(g), 2(h), 2(i), 3(a), 3(b), 3(c), 3(d), 3(e), 3(f).

268 Fig. 4 shows the raw distribution, Fig. 5 shows the $A \times \varepsilon$ for the $\cos \theta$ distribution, and the corrected
 269 shape is shown in Fig. 6.

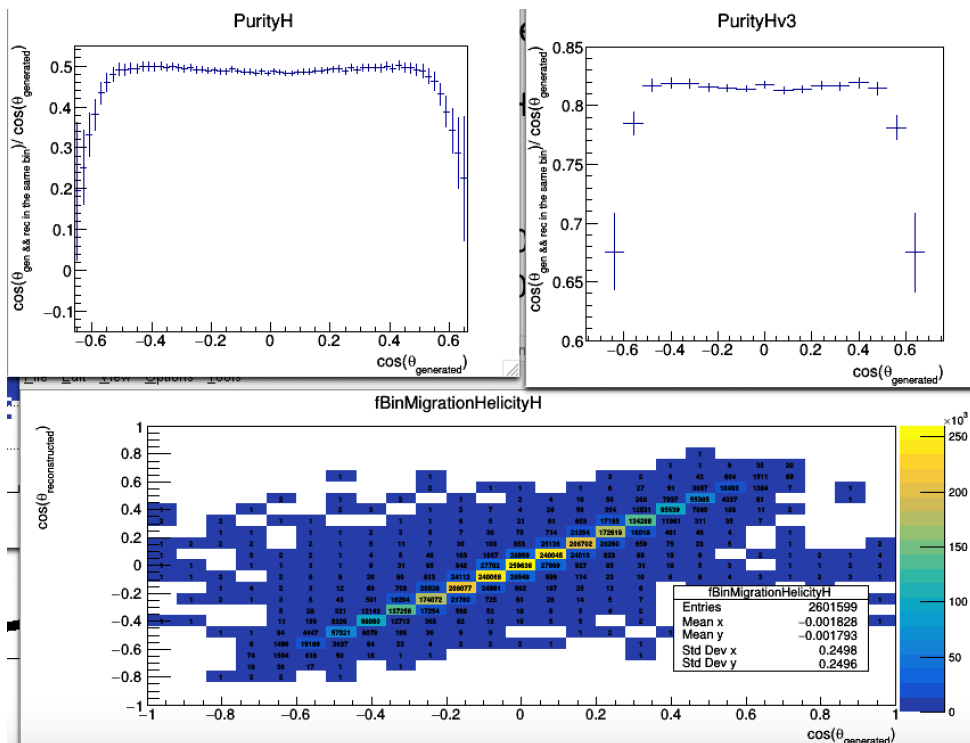


Fig. 1: Bin migration effects. The upper panels show the purity. In particular, the upper right panel shows the adopted binning for the analysis.

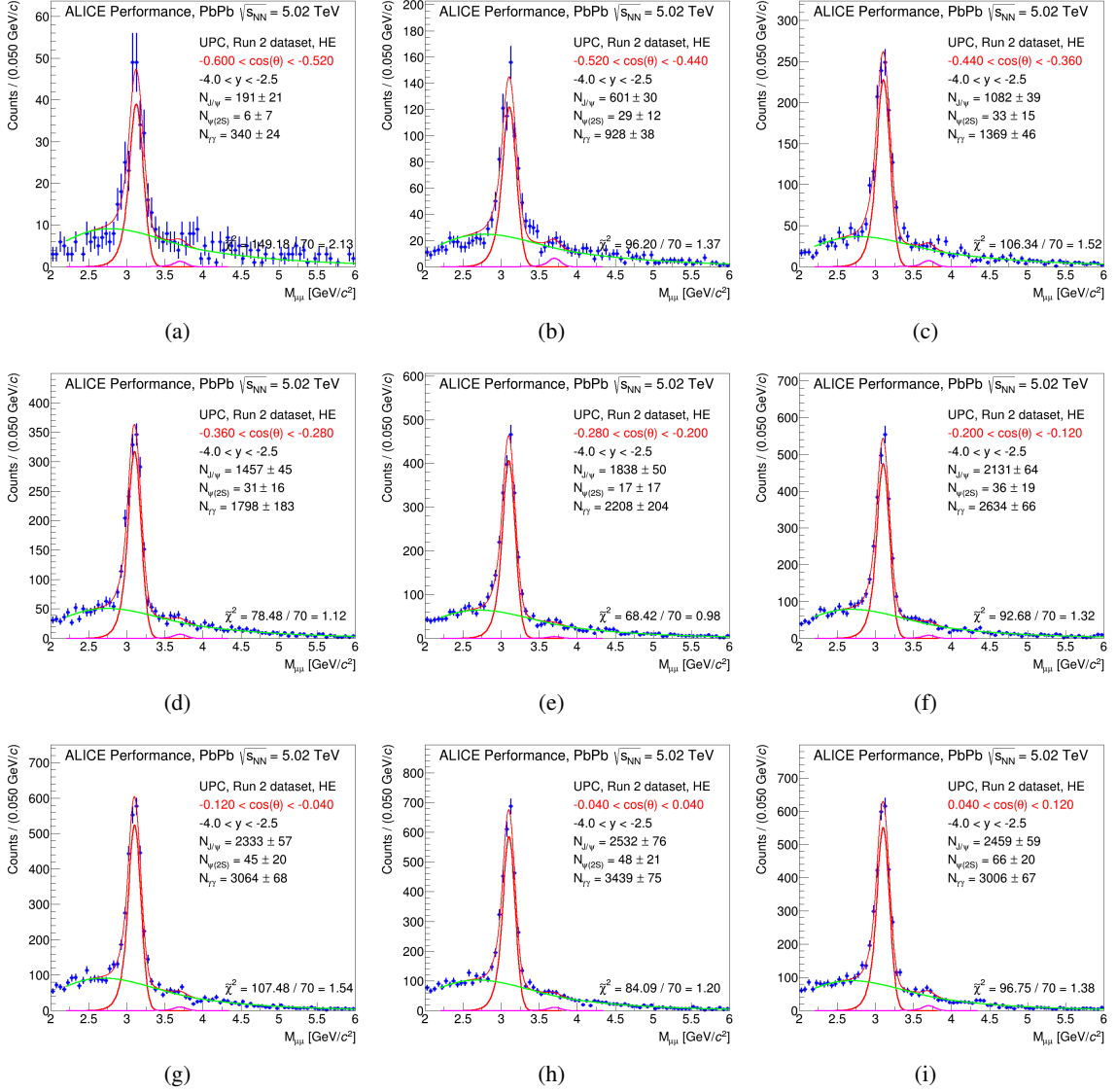


Fig. 2: Signal extraction in $\cos \theta$. From the upper left to the lower right panel, increasing bin in $\cos \theta$, $-0.6 < \cos \theta < 0.12$

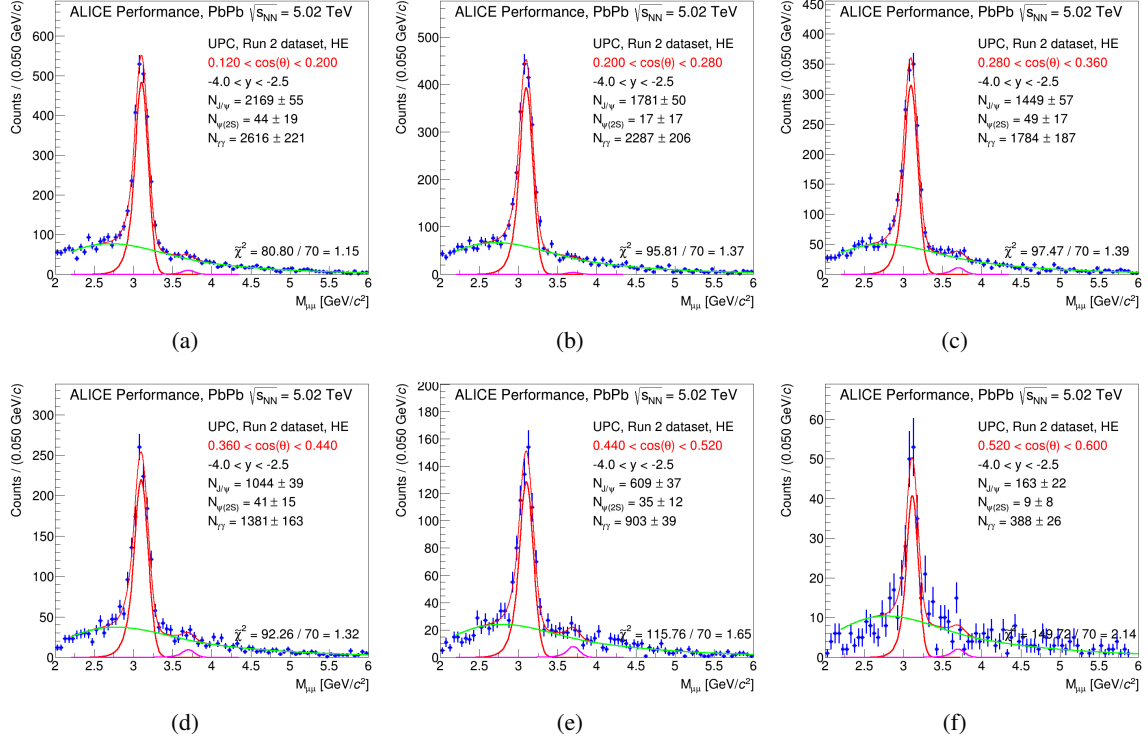


Fig. 3: Signal extraction in $\cos \theta$. From the upper left to the lower right panel, increasing bin in $\cos \theta$, $0.12 < \cos \theta < 0.6$

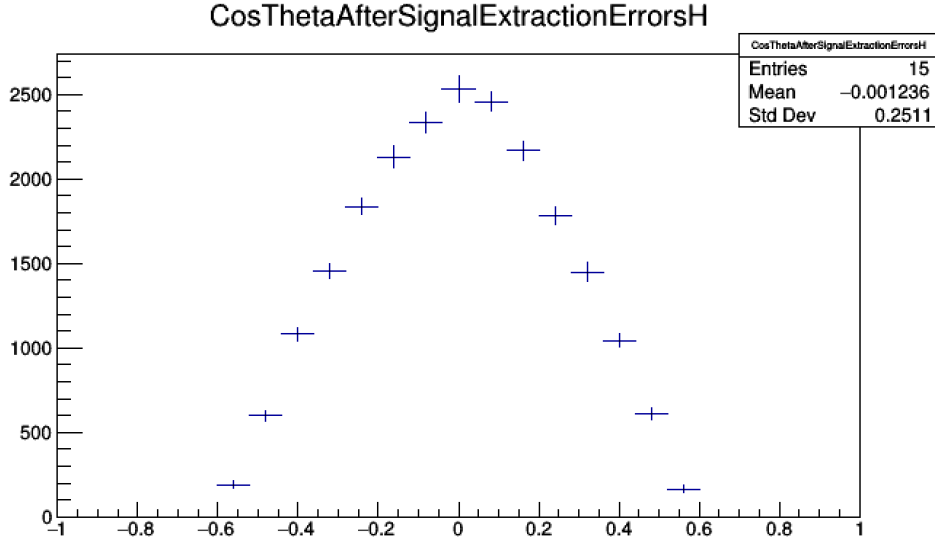


Fig. 4: Raw $\cos \theta$ distribution.

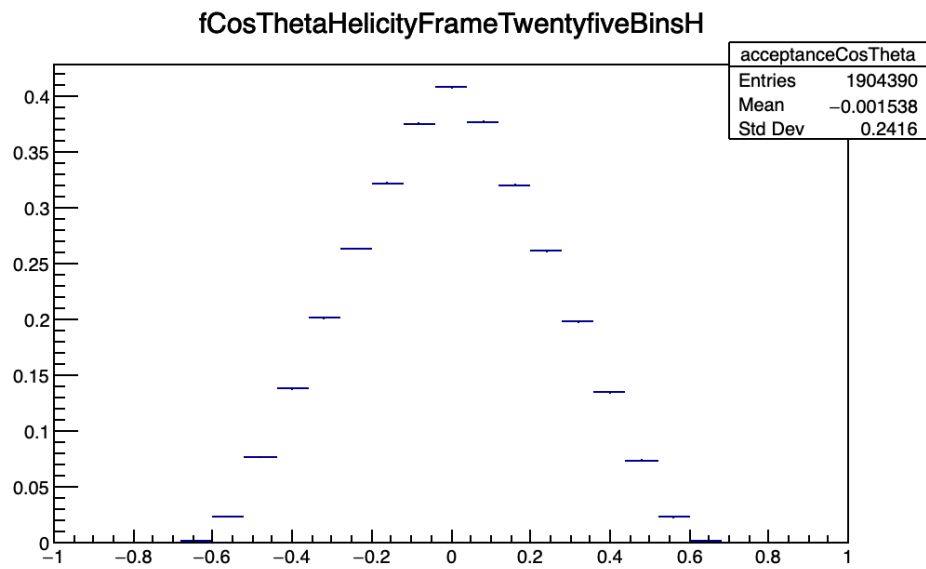
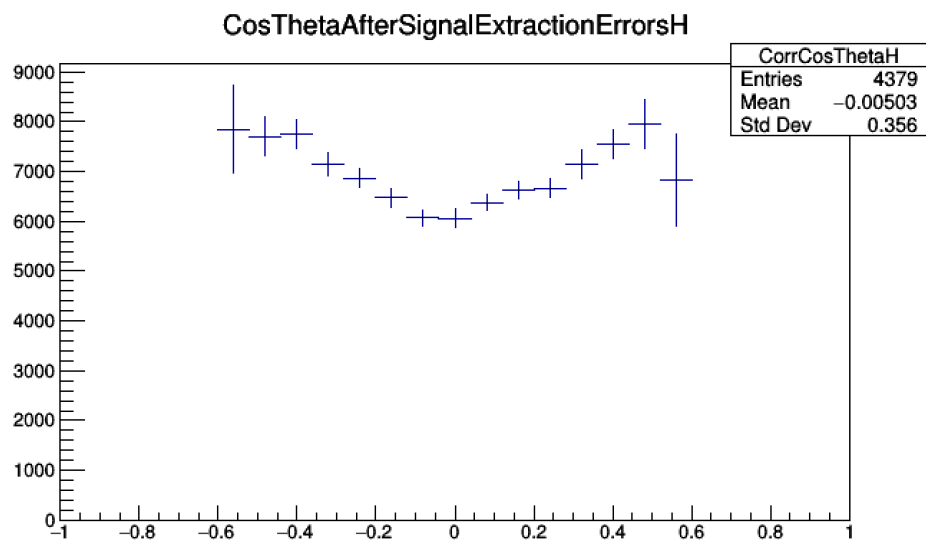
**Fig. 5:** $A \times \varepsilon$ for the $\cos \theta$ distribution.**Fig. 6:** Corrected $\cos \theta$ distribution.

Table 1: $\frac{dN}{d\cos\theta}$ raw distribution in HE frame.

Bin number	Range	dN/dcos θ	Error (stat.)
1	-1.00 – -0.92	0	0
2	-0.92 – -0.84	0	0
3	-0.84 – -0.76	0	0
4	-0.76 – -0.68	0	0
5	-0.68 – -0.60	0	0
6	-0.60 – -0.52	191	21
7	-0.52 – -0.44	601	30
8	-0.44 – -0.36	1082	39
9	-0.36 – -0.28	1457	45
10	-0.28 – -0.20	1838	50
11	-0.20 – -0.12	2131	64
12	-0.12 – -0.04	2333	57
13	-0.04 – 0.04	2532	76
14	0.04 – 0.12	2459	59
15	0.12 – 0.20	2169	55
16	0.20 – 0.28	1781	50
17	0.28 – 0.36	1449	57
18	0.36 – 0.44	1044	39
19	0.44 – 0.52	609	37
20	0.52 – 0.60	163	22
21	0.60 – 0.68	0	0
22	0.68 – 0.76	0	0
23	0.76 – 0.84	0	0
24	0.84 – 0.92	0	0
25	0.92 – 1.00	0	0

270 **5.2 Phi**

271 The yields are extracted for each ϕ bin using the formalism introduced earlier in this document, and are
 272 shown in Figs. 7(a), 7(b), 7(c), 7(d), 7(e), 7(f), 7(g), 7(h), 7(i), 8(a), 8(b), 8(c), 8(d), 8(e), 8(f), 8(g), 8(h),
 273 9(a), 9(b), 9(c), 9(d), 9(e), 9(f), 9(g), 9(h).

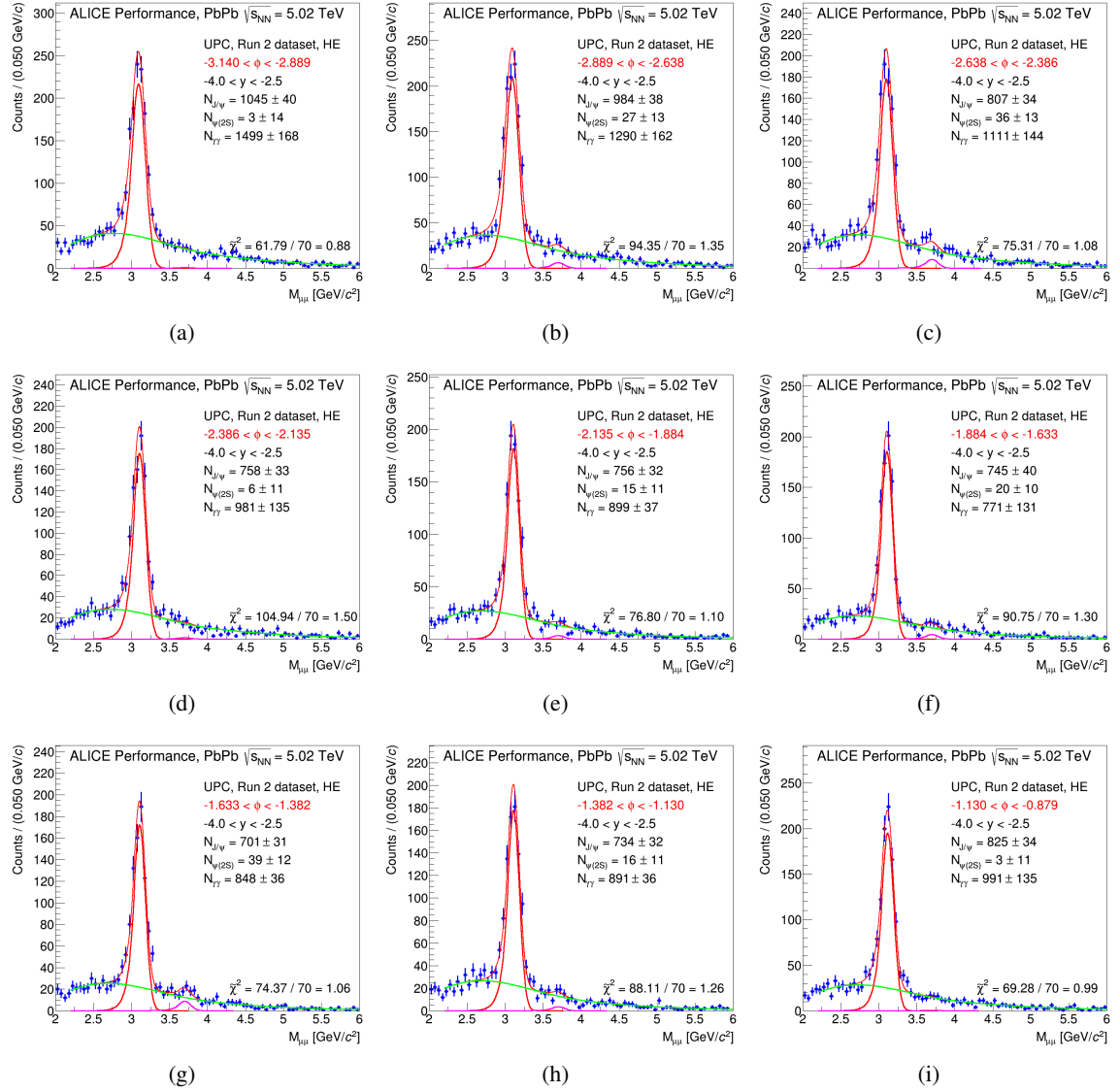


Fig. 7: Signal extraction in ϕ . From the upper left to the lower right panel, increasing bin in ϕ .

274 Fig. 10 shows the raw distribution, Fig. 11 shows the $A \times \varepsilon$ for the ϕ distribution, and the corrected shape
 275 is shown in Fig. 12.

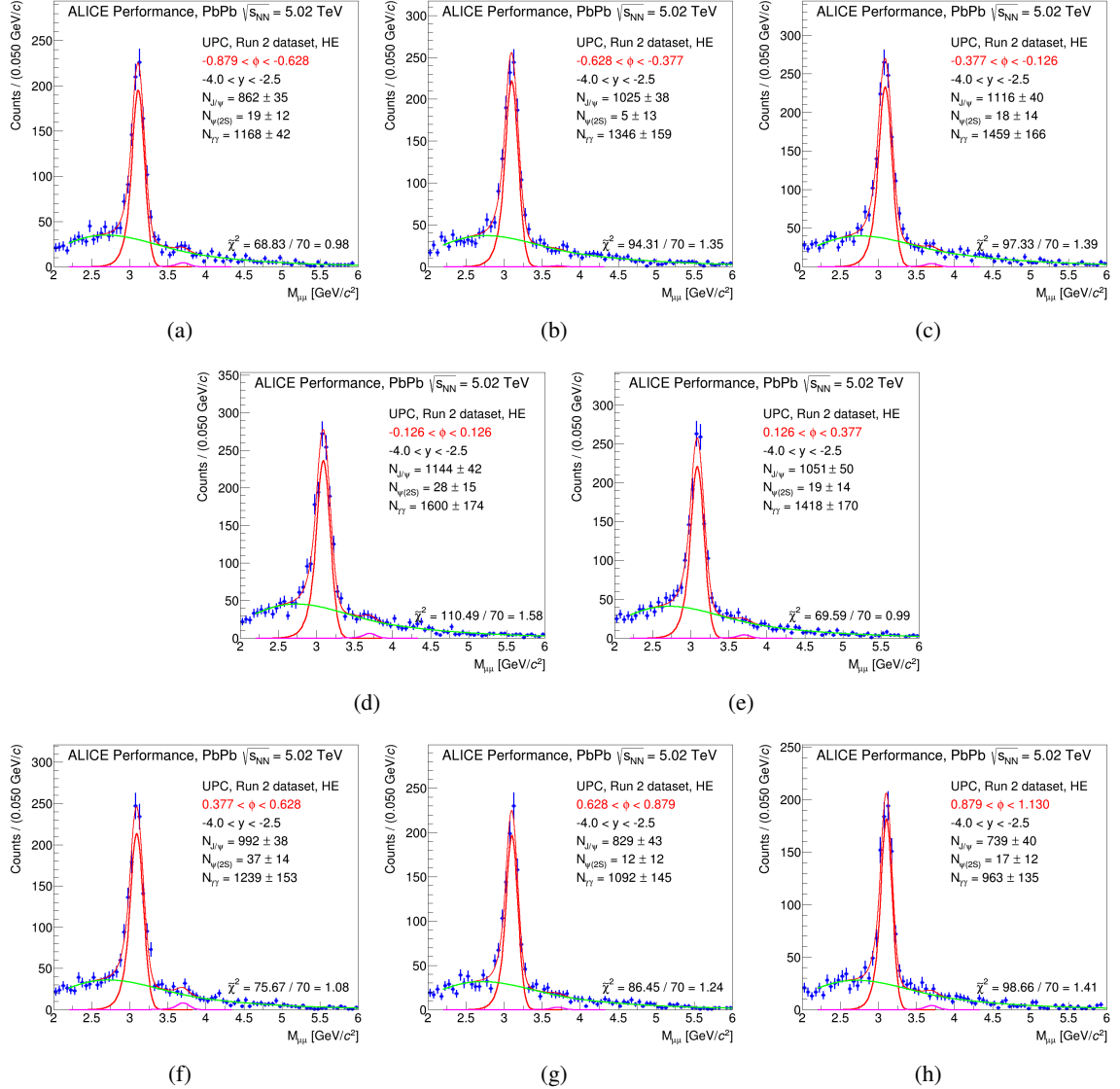


Fig. 8: Signal extraction in ϕ . From the upper left to the lower right panel, increasing bin in ϕ .

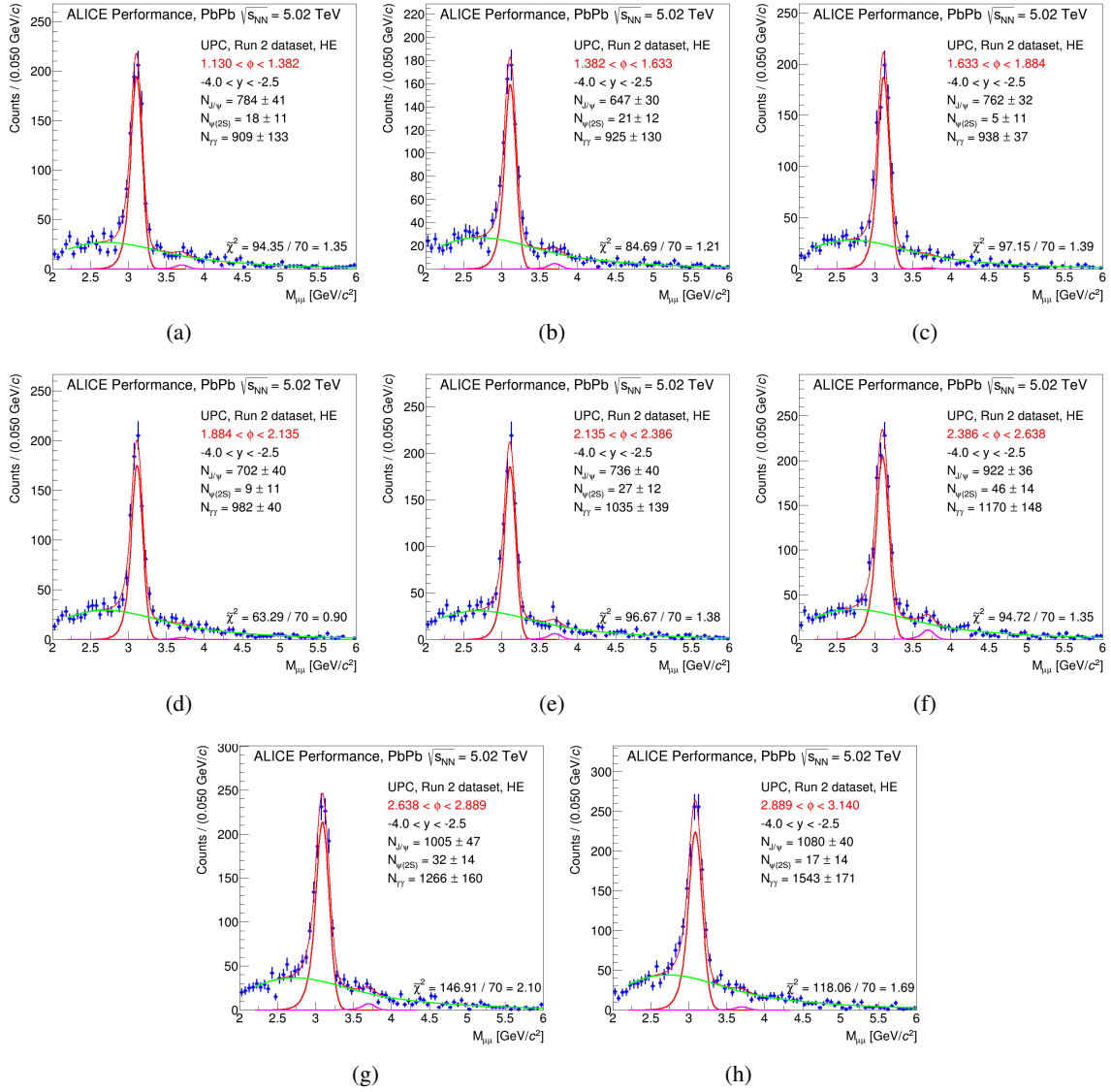


Fig. 9: Signal extraction in ϕ . From the upper left to the lower right panel, increasing bin in ϕ .

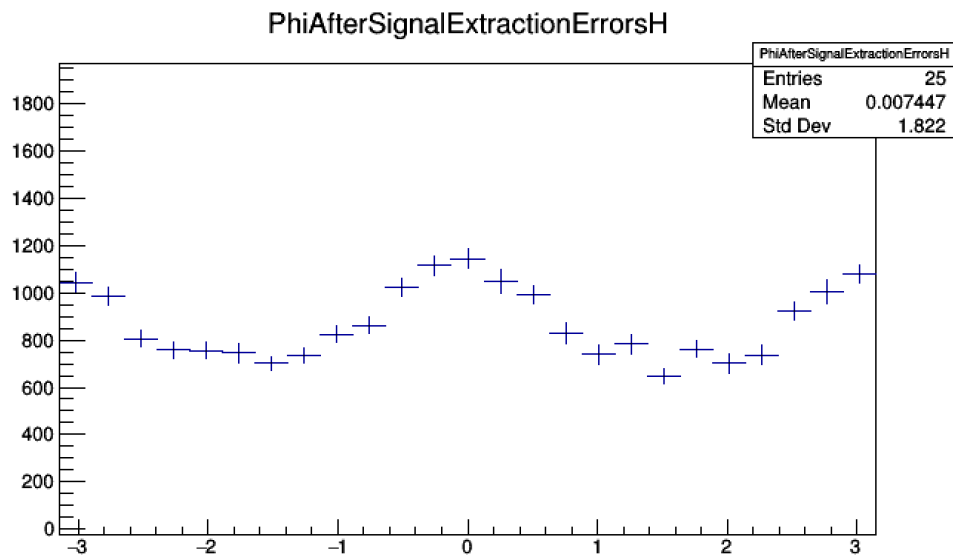


Fig. 10: Raw ϕ distribution.

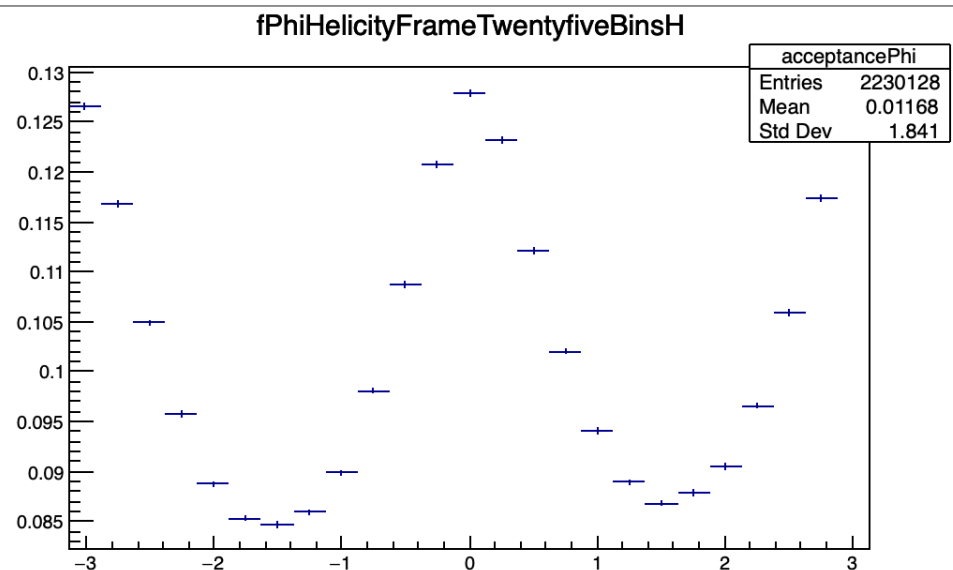
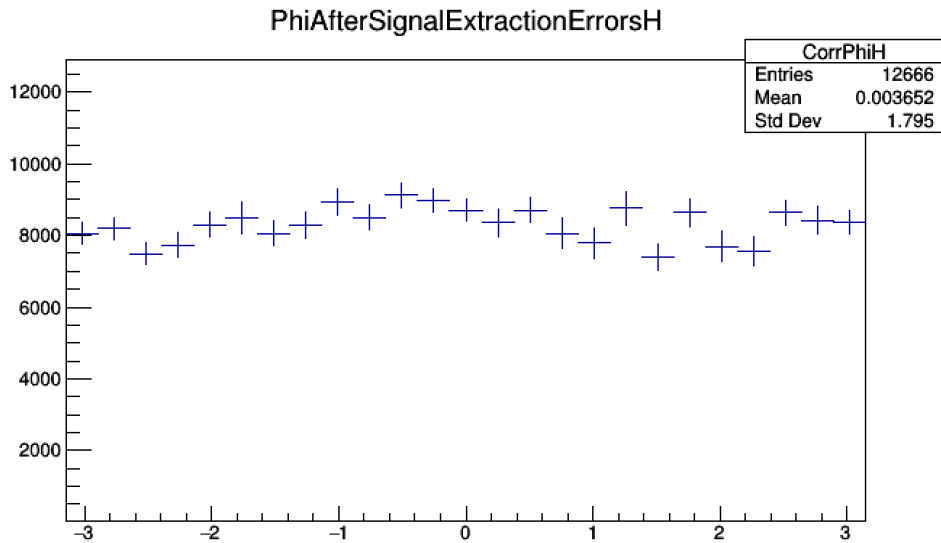


Fig. 11: $A \times \varepsilon$ for the ϕ distribution.

**Fig. 12:** $A \times \epsilon$ corrected ϕ distribution.**Table 2:** $\frac{dN}{d\phi}$ raw distribution in HE frame.

Bin number	Range	$\frac{dN}{d\phi}$	Error (stat.)
1	-3.140 - -2.889	1045	40
2	-2.889 - -2.638	984	38
3	-2.638 - -2.386	807	34
4	-2.386 - -2.135	758	33
5	-2.135 - -1.884	756	32
6	-1.884 - -1.633	745	40
7	-1.633 - -1.382	701	31
8	-1.382 - -1.130	734	32
9	-1.130 - -0.879	825	33
10	-0.879 - -0.628	882	35
11	-0.628 - -0.377	1025	38
12	-0.377 - -0.126	1116	40
13	-0.126 - 0.126	1144	42
14	0.126 - 0.377	1051	50
15	0.377 - 0.628	992	38
16	0.628 - 0.879	829	43
17	0.879 - 1.130	739	40
18	1.130 - 1.382	784	41
19	1.382 - 1.633	647	30
20	1.633 - 1.884	762	32
21	1.884 - 2.135	702	40
22	2.135 - 2.386	736	40
23	2.386 - 2.638	922	36
24	2.638 - 2.889	1005	47
25	2.889 - 3.140	1080	40

276 **5.3 TildePhi**

277 Twenty five equal sized bins are employed for this distribution.

278 The yields are extracted using the formalism explained earlier in this document, and are shown in
 279 Figs. 13(a), 13(b), 13(c), 13(d), 13(e), 13(f), 13(g), 13(h), 13(i), 14(a), 14(b), 14(c), 14(d), 14(e), 14(f), 14(g),
 280 14(h), 14(i), 15(a), 15(b), 15(c), 15(d), 15(e), 15(f), 15(g).

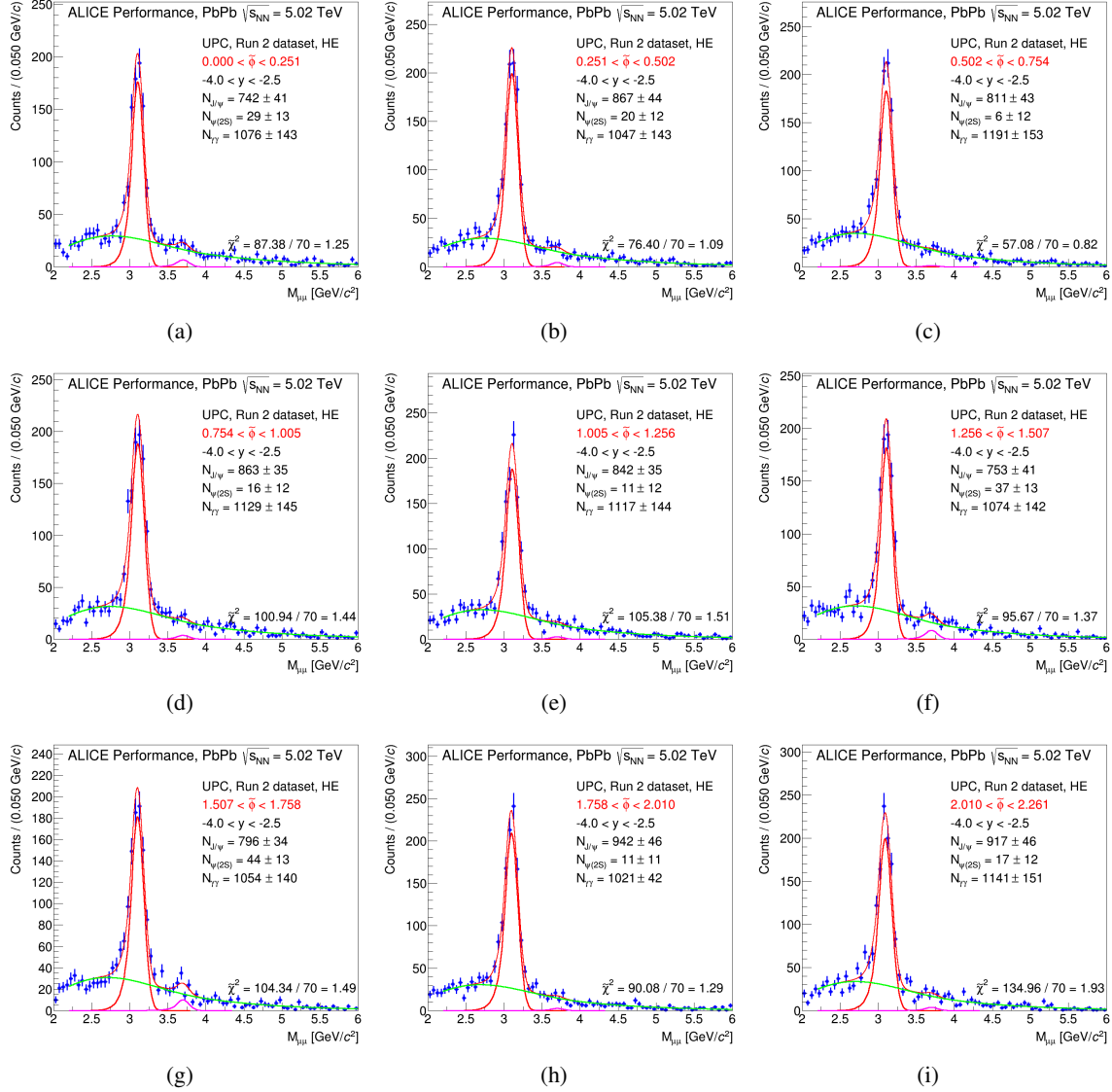


Fig. 13: Signal extraction in $\tilde{\phi}$. From the upper left to the lower right panel, increasing bin in $\tilde{\phi}$.

281 Fig. 16 shows the raw distribution, Fig. 17 shows the $A \times \epsilon$ for the $\tilde{\phi}$ distribution, and the corrected shape
 282 shown in Fig. 18.

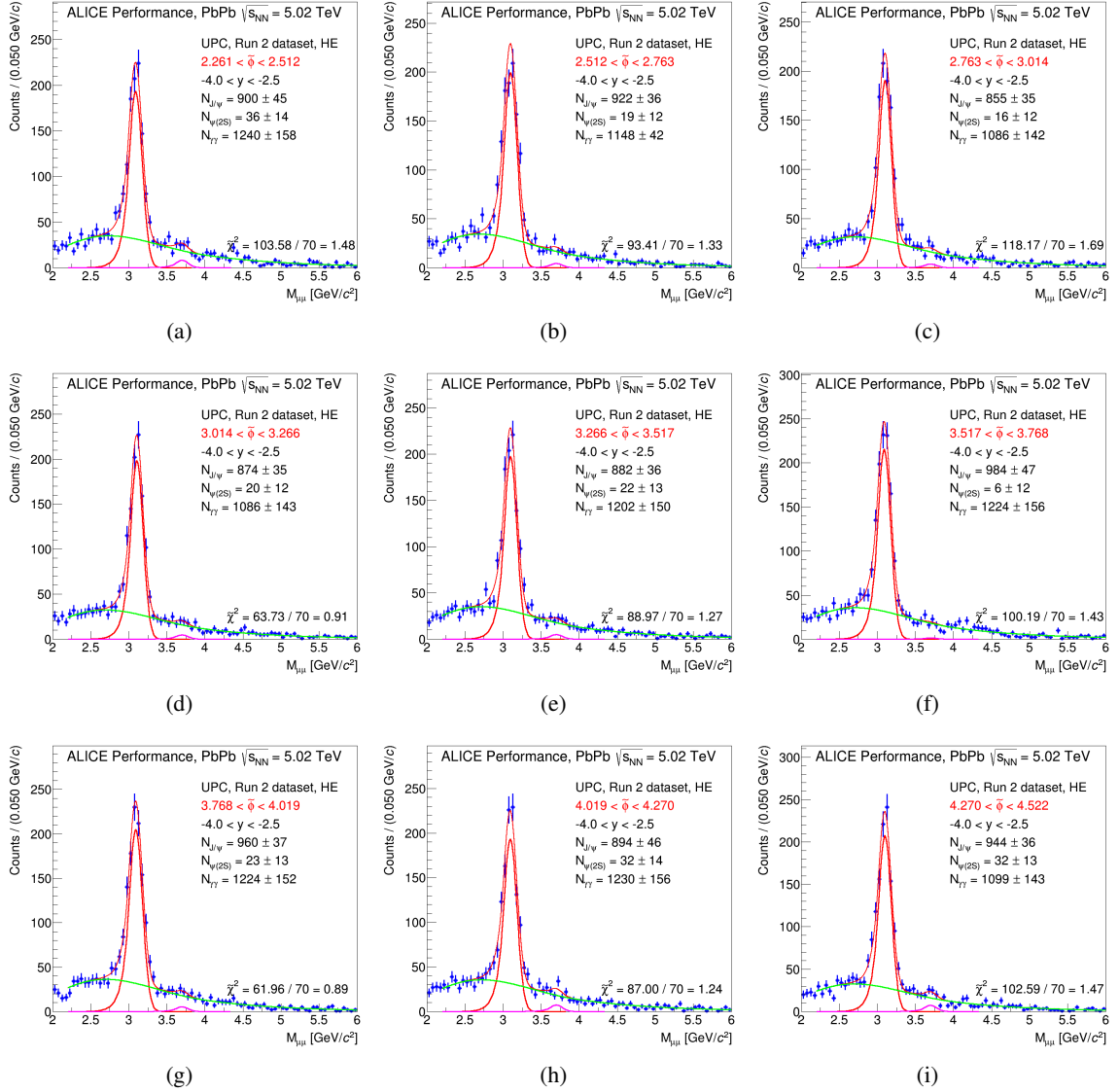


Fig. 14: Signal extraction in $\tilde{\phi}$. From the upper left to the lower right panel, increasing bin in $\tilde{\phi}$.

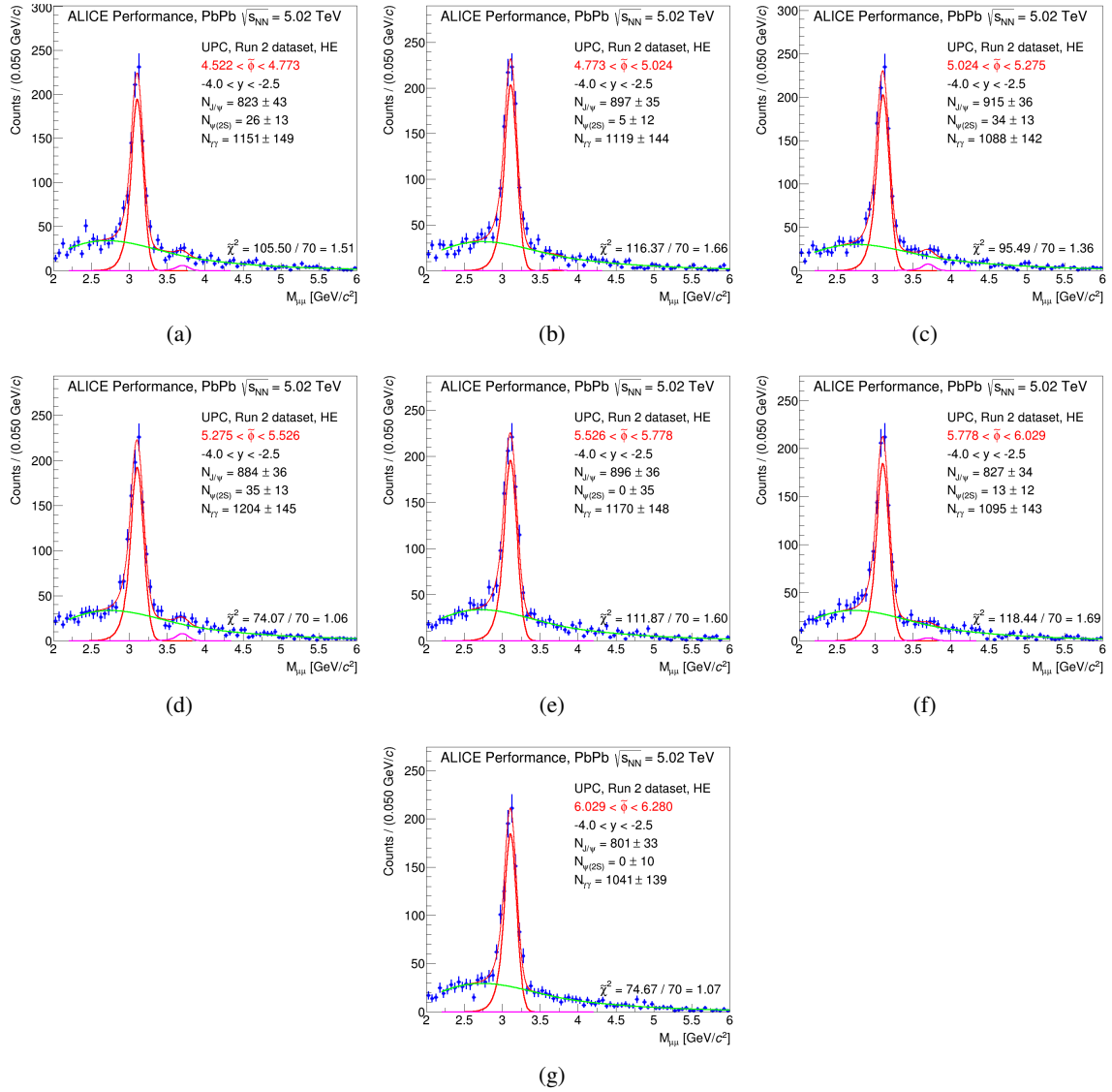
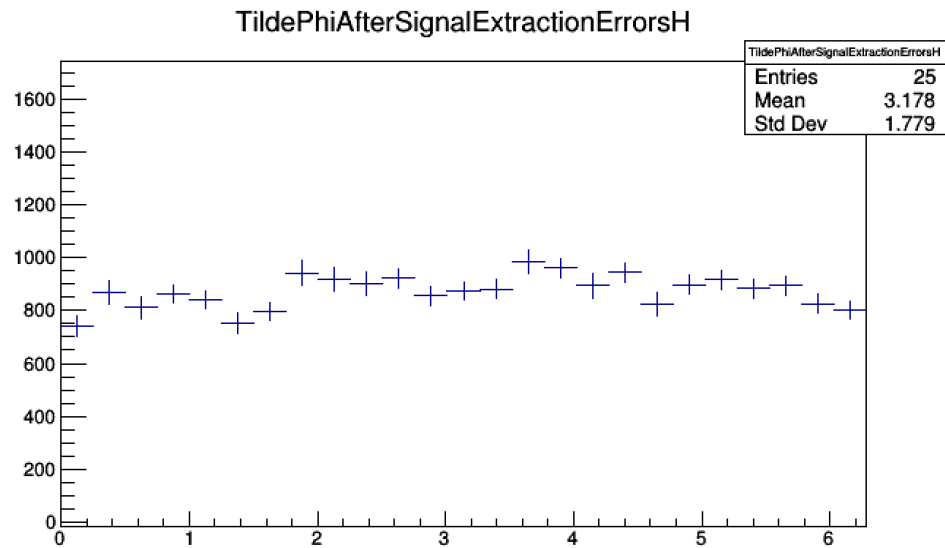
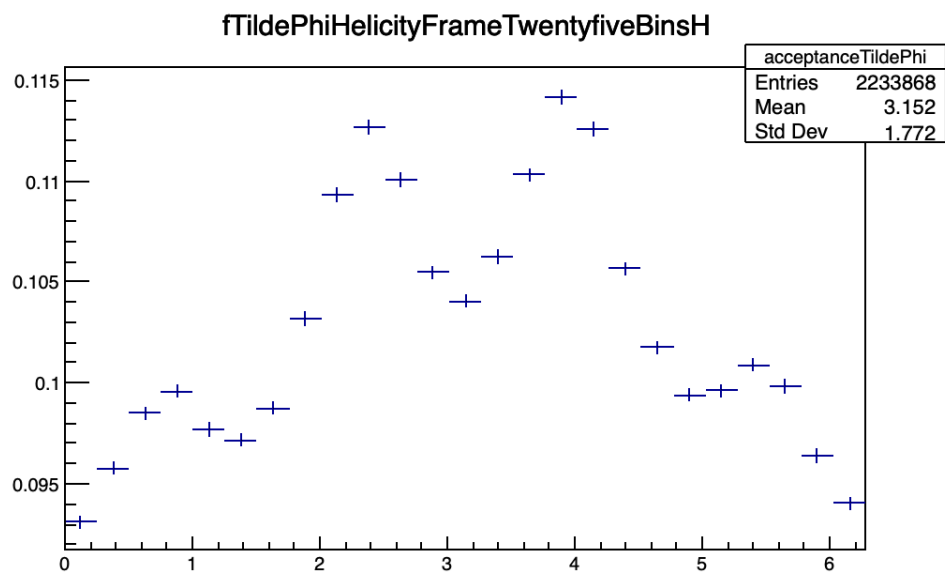


Fig. 15: Signal extraction in $\tilde{\phi}$. From the upper left to the lower right panel, increasing bin in $\tilde{\phi}$.

**Fig. 16:** Raw $\tilde{\phi}$ distribution.**Fig. 17:** $A \times \varepsilon$ for the $\tilde{\phi}$ distribution.

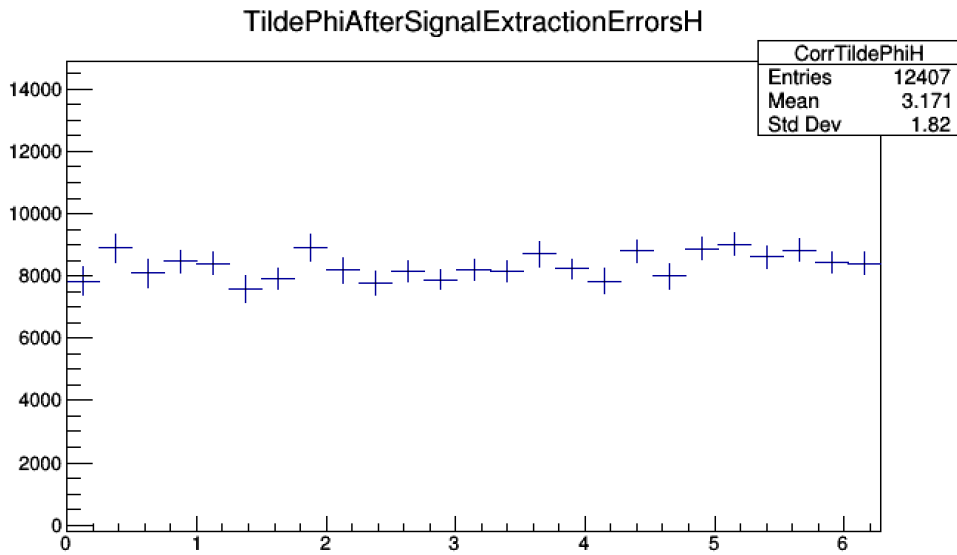


Fig. 18: Corrected $\tilde{\phi}$ distribution.

Table 3: $\frac{dN}{d\tilde{\phi}}$ raw distribution in HE frame.

Bin number	Range	$\frac{dN}{d\tilde{\phi}}$	Error (stat.)
1	0.000 – 0.251	742	41
2	0.251 – 0.502	867	44
3	0.502 – 0.754	811	43
4	0.754 – 1.005	863	35
5	1.005 – 1.256	842	35
6	1.256 – 1.507	753	41
7	1.507 – 1.758	796	34
8	1.758 – 2.010	942	46
9	2.010 – 2.261	917	46
10	2.261 – 2.512	900	45
11	2.512 – 2.763	922	36
12	2.763 – 3.014	855	35
13	3.014 – 3.266	874	35
14	3.266 – 3.517	882	36
15	3.517 – 3.768	984	47
16	3.768 – 4.019	960	37
17	4.019 – 4.270	894	46
18	4.270 – 4.522	944	36
19	4.522 – 4.773	823	43
20	4.773 – 5.024	897	35
21	5.024 – 5.275	915	36
22	5.275 – 5.526	884	36
23	5.526 – 5.778	896	36
24	5.778 – 6.029	827	34
25	6.029 – 6.280	801	33

283 **5.4 Combined fits**

284 The principal parameter in Eq. 2, is λ_θ . To constrain its value as much as possible, it is fitted together
 285 with the other two distributions too in this 1D analysis. This is because the other two distributions also
 286 depend on λ_θ . A Minuit macro is used to do a simultaneous fit on all three distributions. The results are
 287 shown below in Figs. 19(a), 19(b), 19(c).

The fit is performed over the full range in $\cos \theta$, ϕ , $\tilde{\phi}$. The results are as follows:

$$\begin{aligned}\lambda_\theta &= 1.208 \pm 0.155 , \\ \lambda_\phi &= 0.049 \pm 0.026 , \\ \lambda_{\theta\phi} &= -0.032 \pm 0.037 .\end{aligned}$$

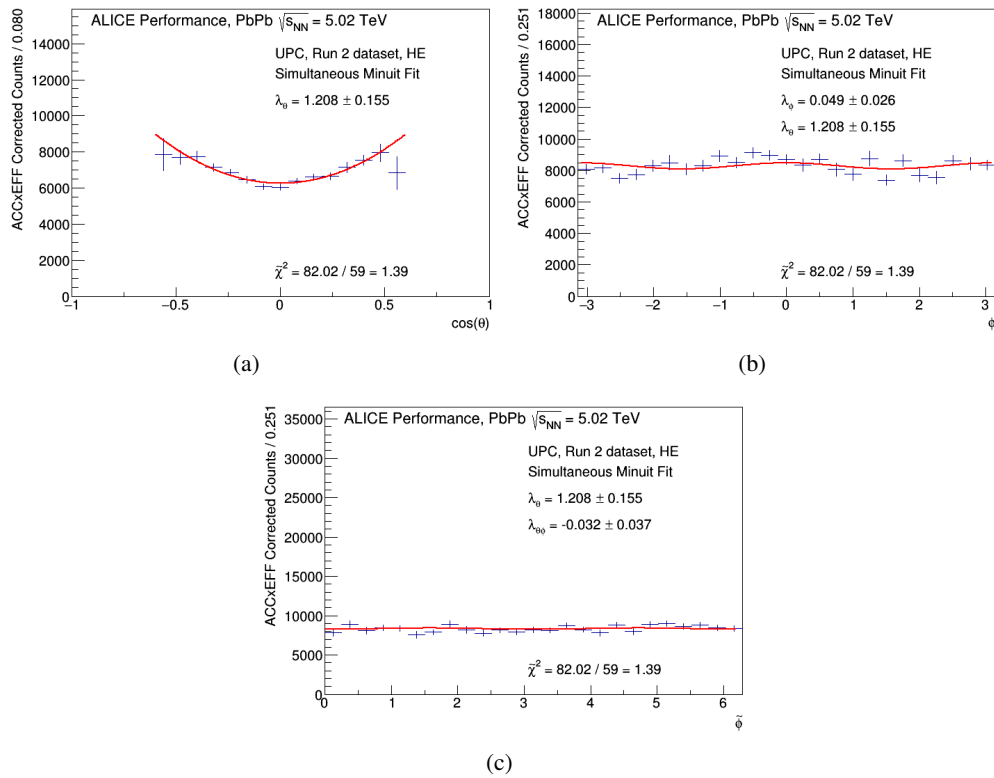


Fig. 19: Simultaneous fit to the distributions.

288 **6 Invariant Mass Fits for 1D signal extraction in the Collins-Soper frame**

289 **6.1 CosTheta**

290 In a similar manner to the previous section, twenty five equal sized bins have been chosen overall for
291 the $\cos \theta$, ϕ and $\tilde{\phi}$ distributions, in order to allow a direct comparison with the results in the Helicity
292 Frame. Only fifteen bins are used in the $\cos \theta$ distribution owing to acceptance problems. The results
293 of the fits are shown in Figs. 20(a), 20(b), 20(c), 20(d), 20(e), 20(f), 20(g), 20(h), 20(i), 21(a), 21(b),
294 21(c), 21(d), 21(e), 21(f).

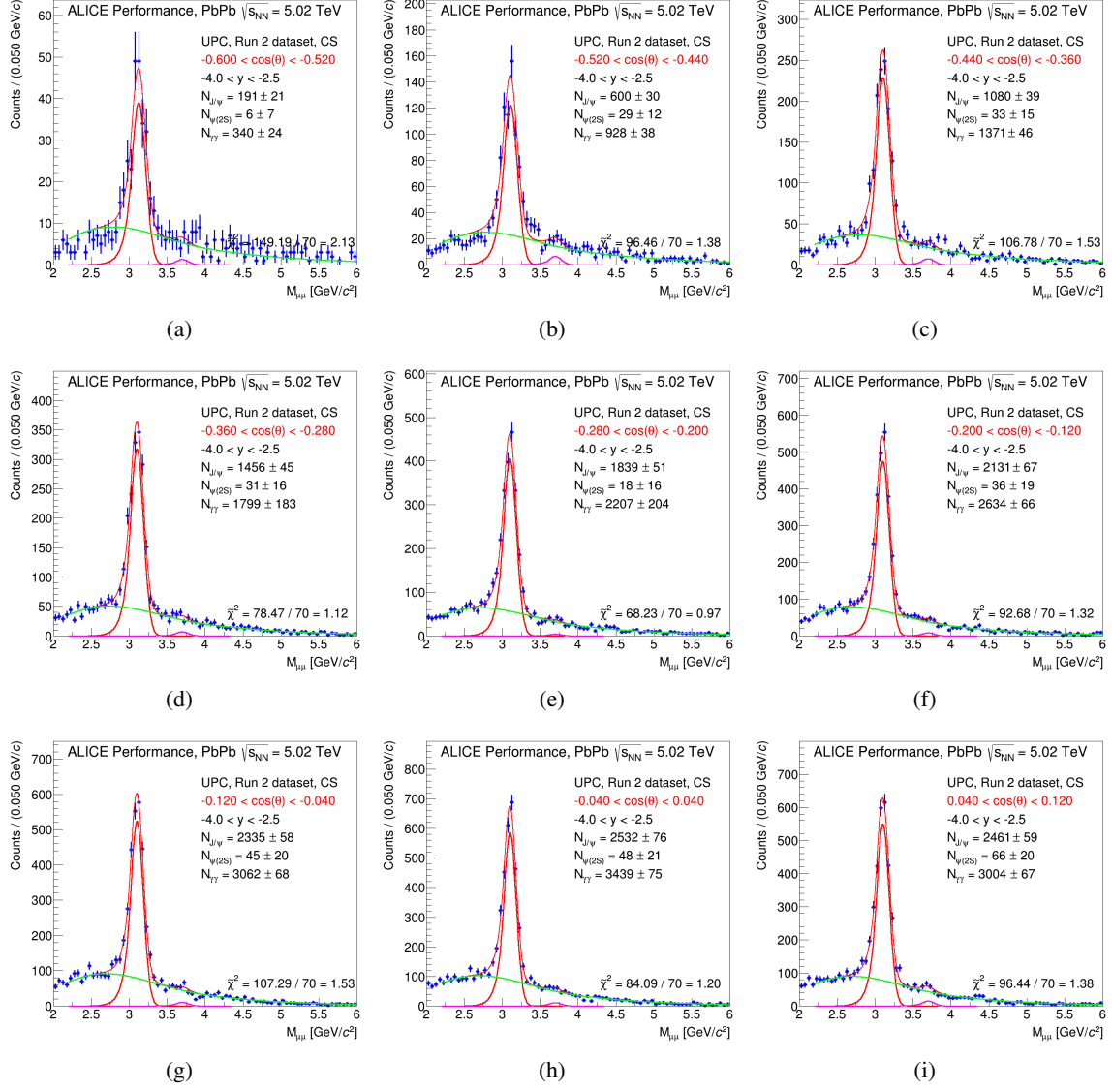


Fig. 20: Signal extraction in $\cos \theta$. From the upper left to the lower right panel, increasing bin in $\cos \theta$.

295 The raw distribution is shown in Fig. 22, the $A \times \epsilon$ for the $\cos \theta$ distribution is shown in Fig. 23, and the
296 corrected shape is shown in Fig. 24.

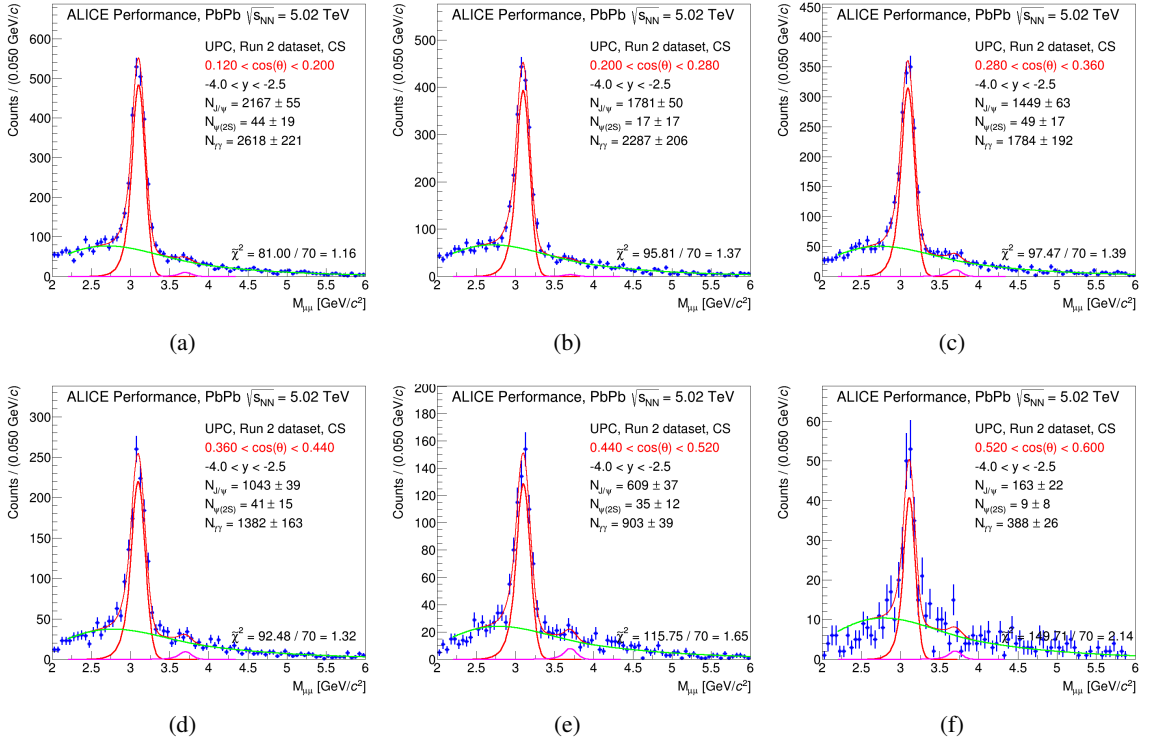


Fig. 21: Signal extraction in $\cos \theta$. From the upper left to the lower right panel, increasing bin in $\cos \theta$.

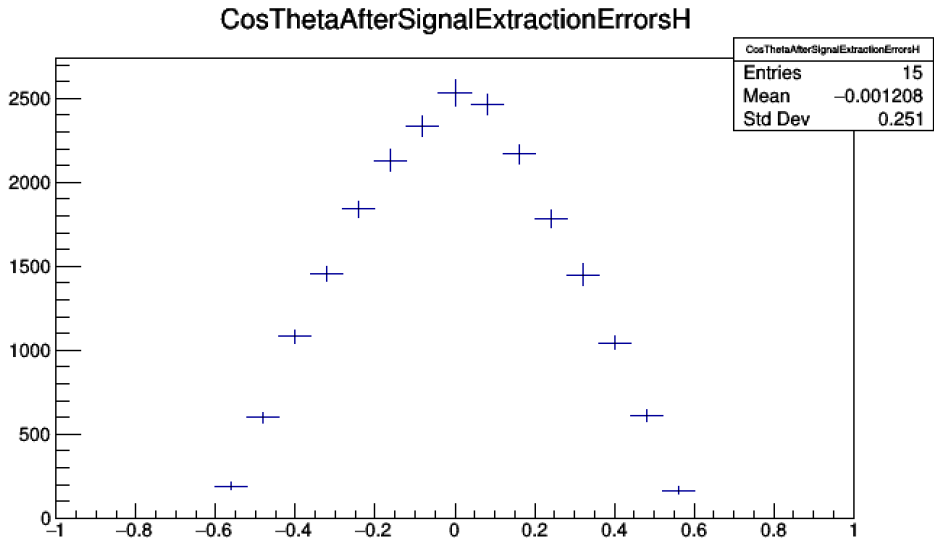


Fig. 22: Raw $\cos \theta$ distribution.

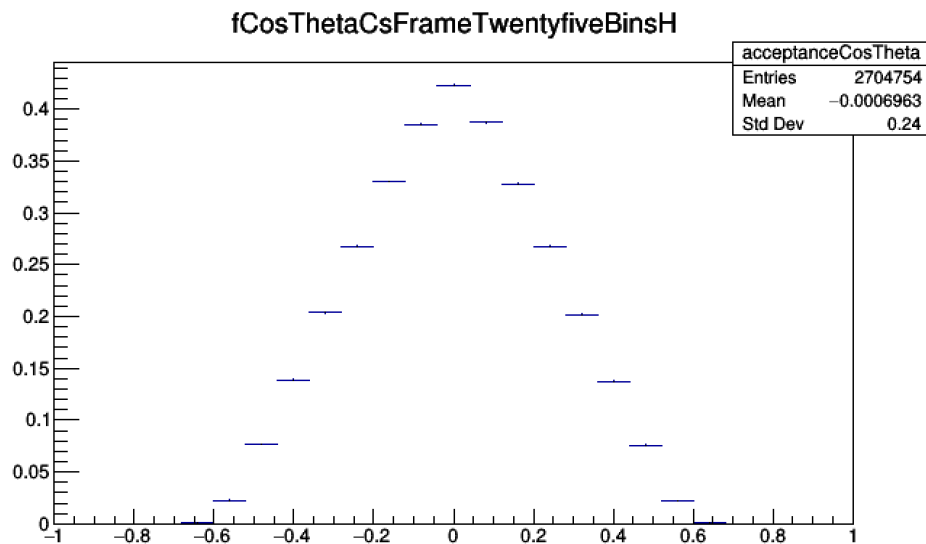


Fig. 23: $A \times \epsilon$ for the $\cos \theta$ distribution.

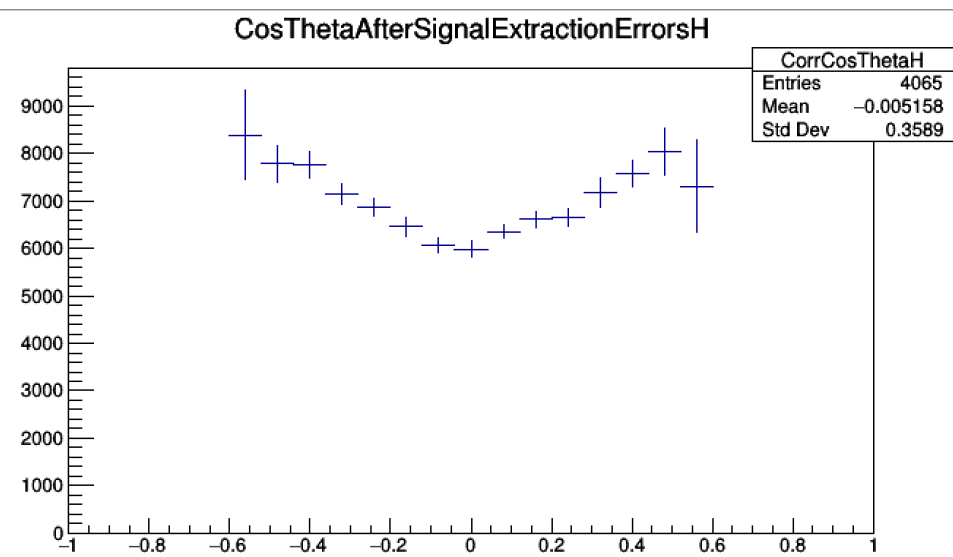


Fig. 24: Corrected $\cos \theta$ distribution.

Table 4: $\frac{dN}{d\cos\theta}$ raw distribution in the CS frame.

Bin number	Range	$\frac{dN}{d\cos\theta}$	Error (stat.)
1	-1.00 – -0.92	0	0
2	-0.92 – -0.84	0	0
3	-0.84 – -0.76	0	0
4	-0.76 – -0.68	0	0
5	-0.68 – -0.60	0	0
6	-0.60 – -0.52	191	21
7	-0.52 – -0.44	600	30
8	-0.44 – -0.36	1080	39
9	-0.36 – -0.28	1456	45
10	-0.28 – -0.20	1839	51
11	-0.20 – -0.12	2131	67
12	-0.12 – -0.04	2335	58
13	-0.04 – 0.04	2532	76
14	0.04 – 0.12	2461	59
15	0.12 – 0.20	2167	55
16	0.20 – 0.28	1781	50
17	0.28 – 0.36	1449	63
18	0.36 – 0.44	1043	39
19	0.44 – 0.52	609	37
20	0.52 – 0.60	163	22
21	0.60 – 0.68	0	0
22	0.68 – 0.76	0	0
23	0.76 – 0.84	0	0
24	0.84 – 0.92	0	0
25	0.92 – 1.00	0	0

297 6.2 Phi

298 The yields are extracted for each ϕ bin using the formalism introduced earlier in this document, and
 299 are shown in Figs. 25(a), 25(b), 25(c), 25(d), 25(e), 25(f), 25(g), 25(h), 25(i), 26(a), 26(b), 26(c),
 300 26(d), 26(e), 26(f), 26(g), 26(h), 27(a), 27(b), 27(c), 27(d), 27(e), 27(f), 27(g), 27(h).

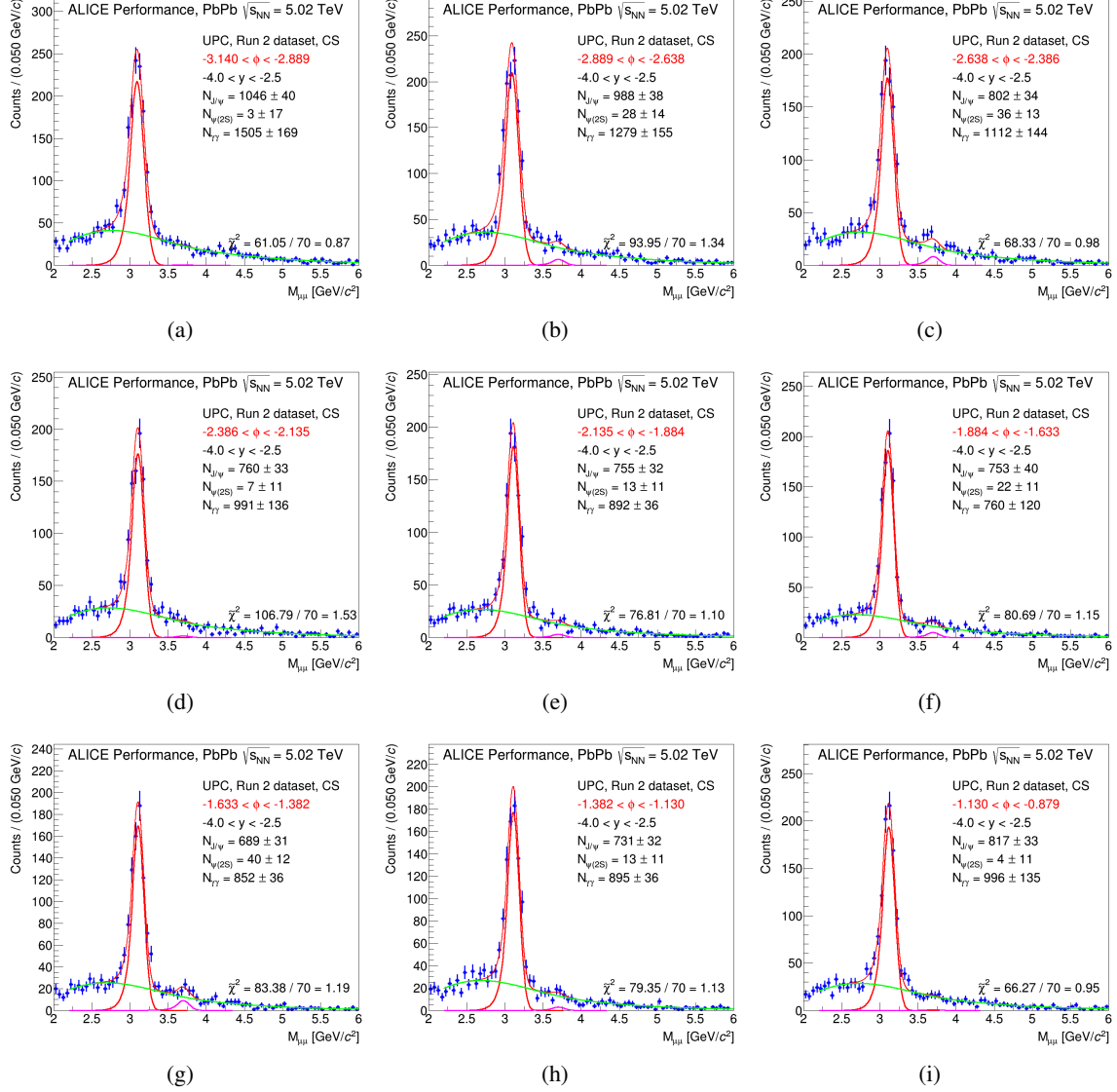


Fig. 25: Signal extraction in ϕ . From the upper left to the lower right panel, increasing bin in ϕ .

301 Fig. 28 shows the raw distribution, Fig. 29 the $A \times \varepsilon$ for the ϕ distribution , and the corrected shape is
 302 shown in Fig. 30.

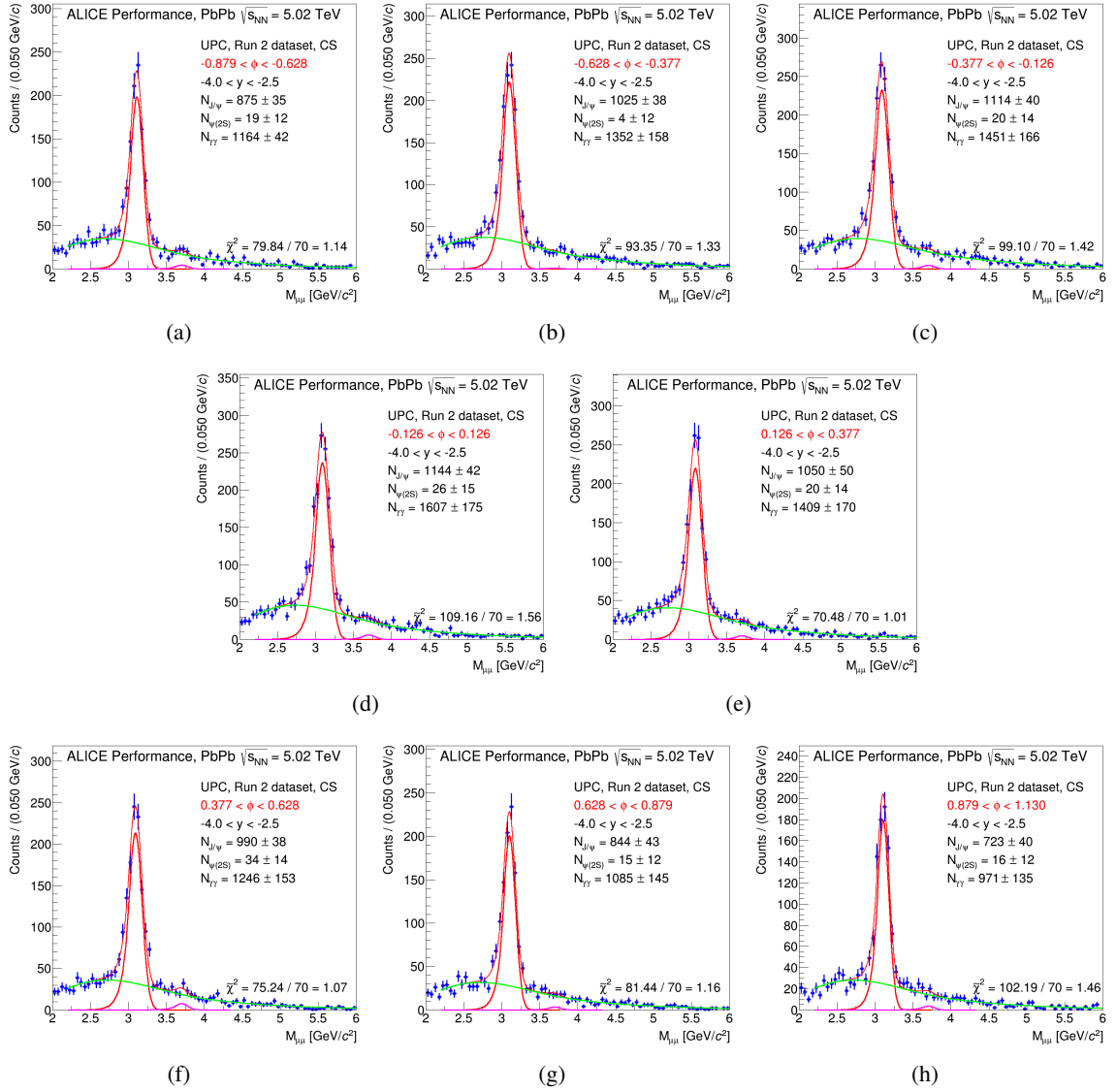


Fig. 26: Signal extraction in ϕ . From the upper left to the lower right panel, increasing bin in ϕ .

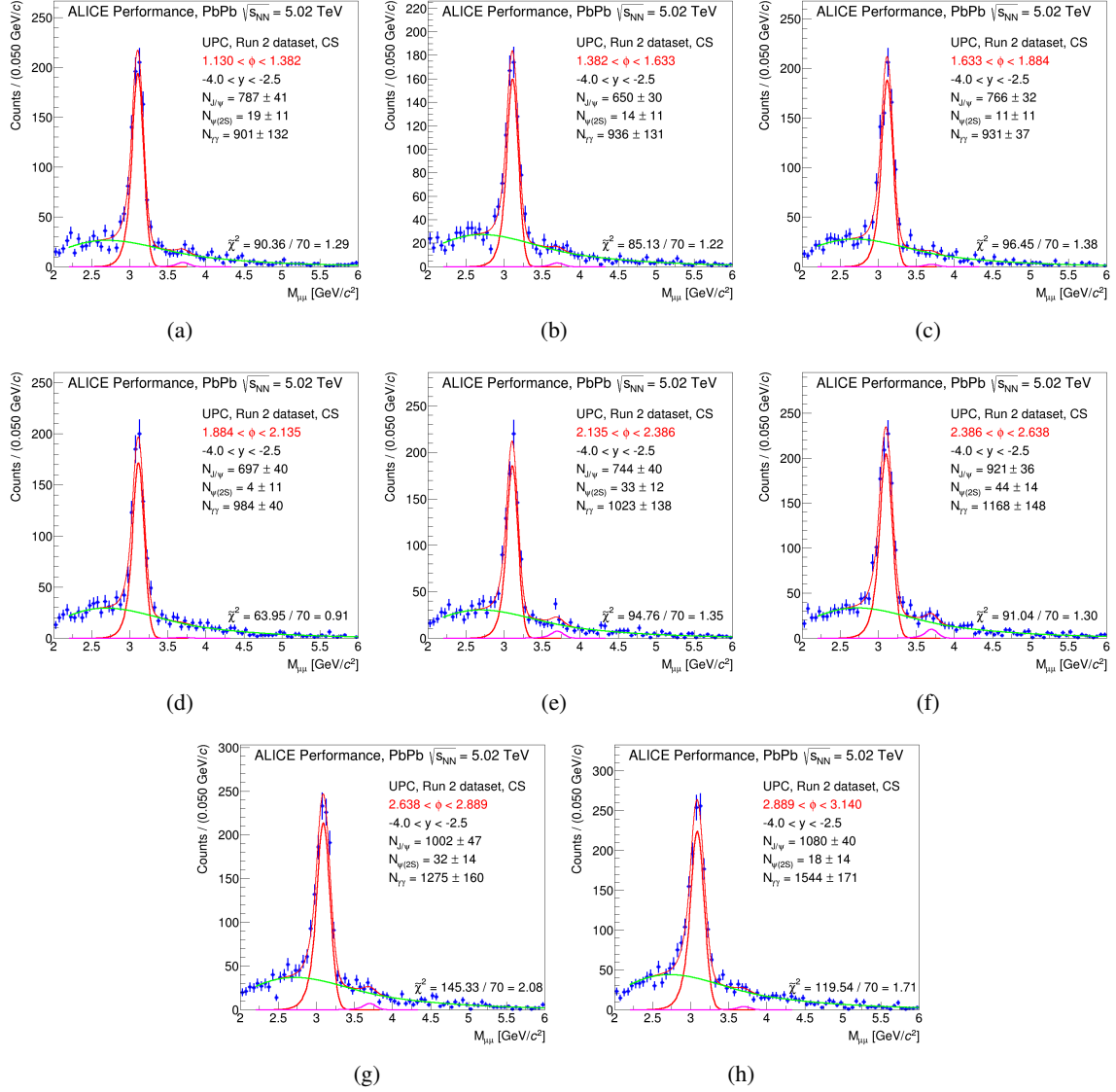
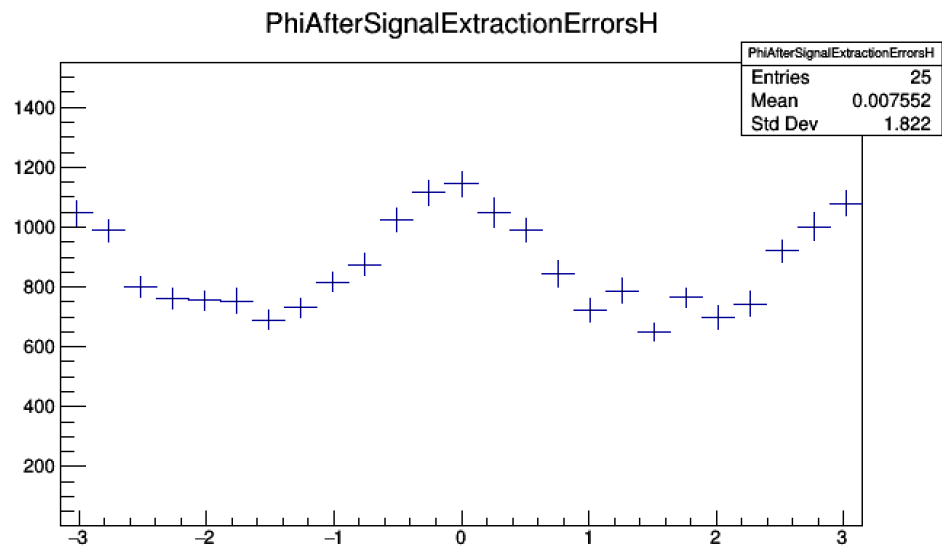
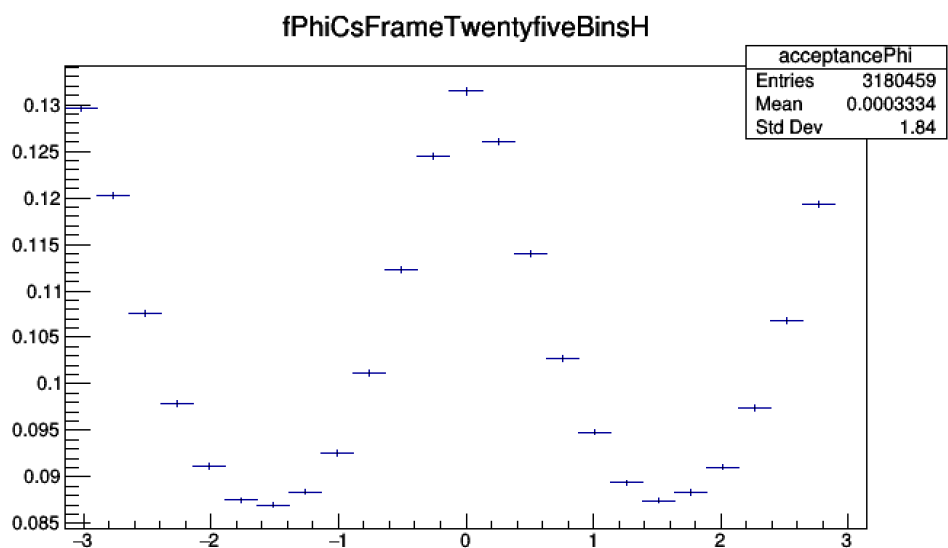


Fig. 27: Signal extraction in ϕ . From the upper left to the lower right panel, increasing bin in ϕ .

**Fig. 28:** Raw ϕ distribution.**Fig. 29:** $A \times \epsilon$ for the ϕ distribution.

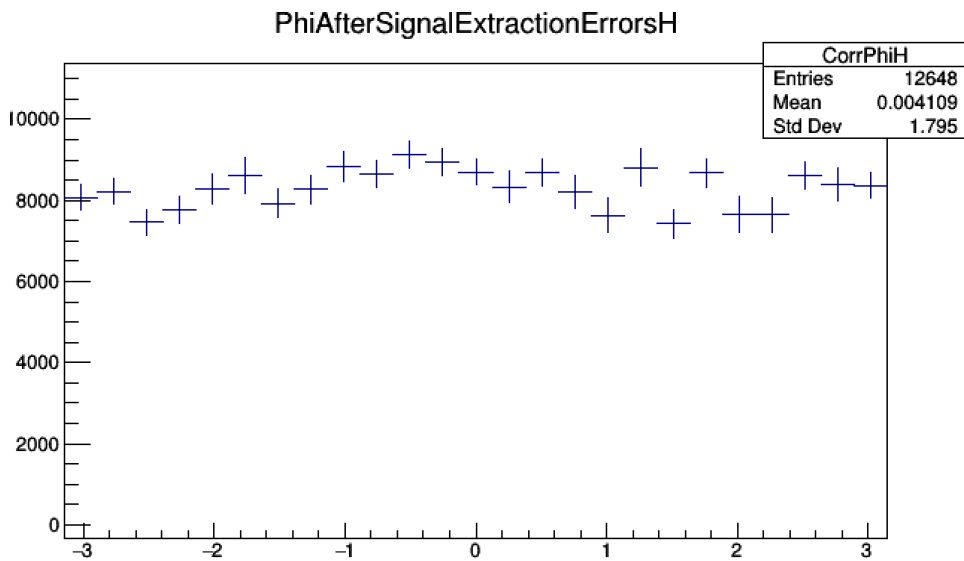


Fig. 30: $A \times \varepsilon$ corrected ϕ distribution.

Table 5: $\frac{dN}{d\phi}$ raw distribution in the CS frame.

Bin number	Range	$\frac{dN}{d\phi}$	Error (stat.)
1	-3.140 – -2.889	1046	40
2	-2.889 – -2.638	988	38
3	-2.638 – -2.386	802	34
4	-2.386 – -2.135	760	33
5	-2.135 – -1.884	755	32
6	-1.884 – -1.633	753	40
7	-1.663 – -1.382	689	31
8	-1.382 – -1.130	731	32
9	-1.130 – -0.879	817	33
10	-0.879 – -0.628	875	35
11	-0.628 – -0.377	1025	38
12	-0.377 – -0.126	1114	40
13	-0.126 – 0.126	1144	42
14	0.126 – 0.377	1050	50
15	0.377 – 0.628	990	38
16	0.628 – 0.879	844	43
17	0.879 – 1.130	723	40
18	1.130 – 1.382	787	41
19	1.382 – 1.633	650	30
20	1.633 – 1.884	766	32
21	1.884 – 2.135	697	40
22	2.135 – 2.386	744	40
23	2.386 – 2.638	921	36
24	2.638 – 2.889	1002	47
25	2.889 – 3.140	1080	40

303 **6.3 TildePhi**

304 Twenty five equal sized bins are employed for this distribution.

305 The yields are extracted using the formalism explained earlier in this document, and are shown in
 306 Figs. 31(a), 31(b), 31(c), 31(d), 31(e), 31(f), 31(g), 31(h), 31(i), 32(a), 32(b), 32(c), 32(d), 32(e), 32(f),
 307 32(g), 32(h), 32(i), 33(a), 33(b), 33(c), 33(d), 33(e), 33(f), 33(g).

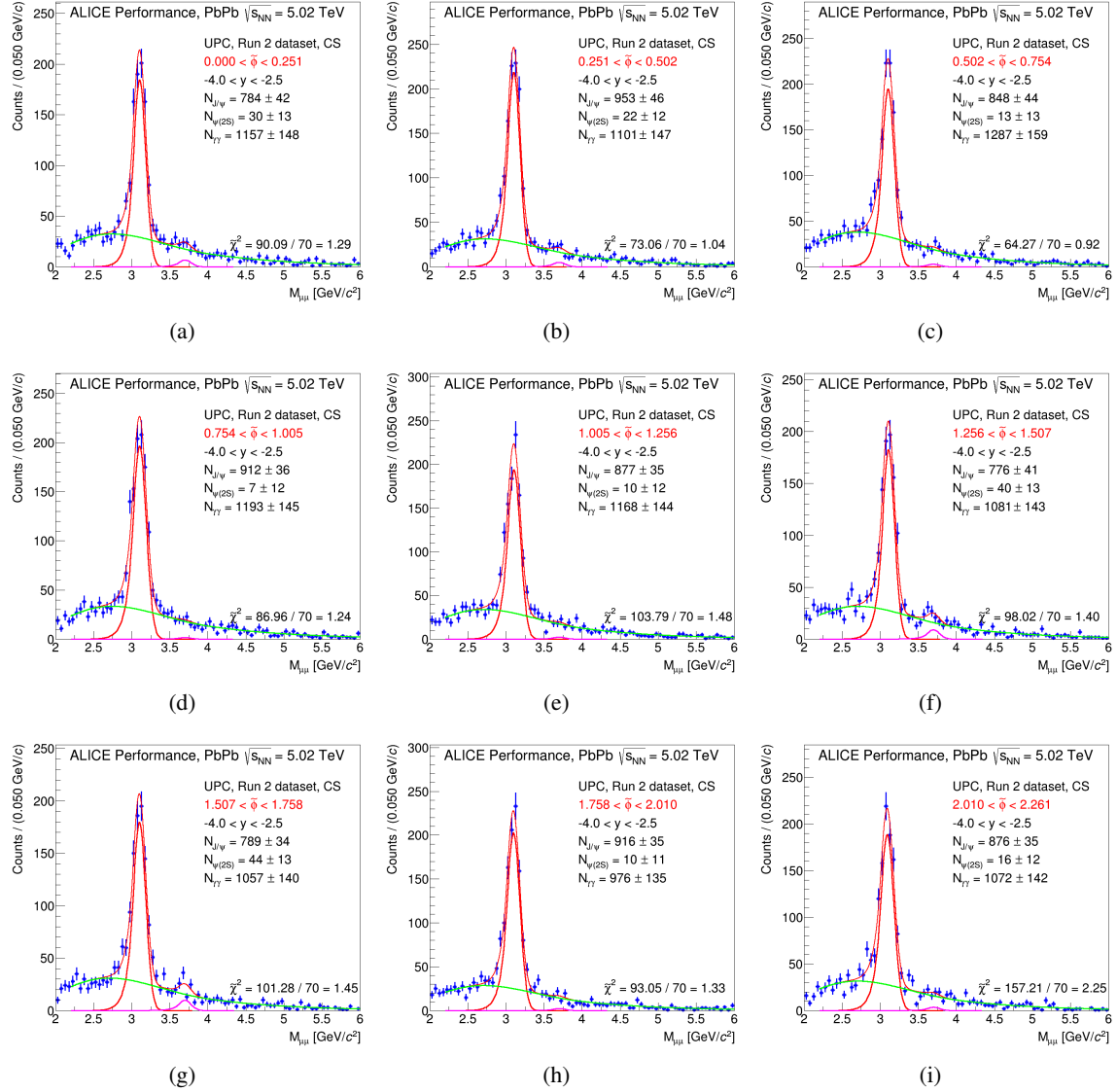


Fig. 31: Signal extraction in $\tilde{\phi}$. From the upper left to the lower right panel, increasing bin in $\tilde{\phi}$.

308 The raw distribution is shown in Fig. 34, the $A \times \epsilon$ for the $\tilde{\phi}$ distribution is shown in Fig. 35, and the
 309 corrected shape is shown in Fig. 36.

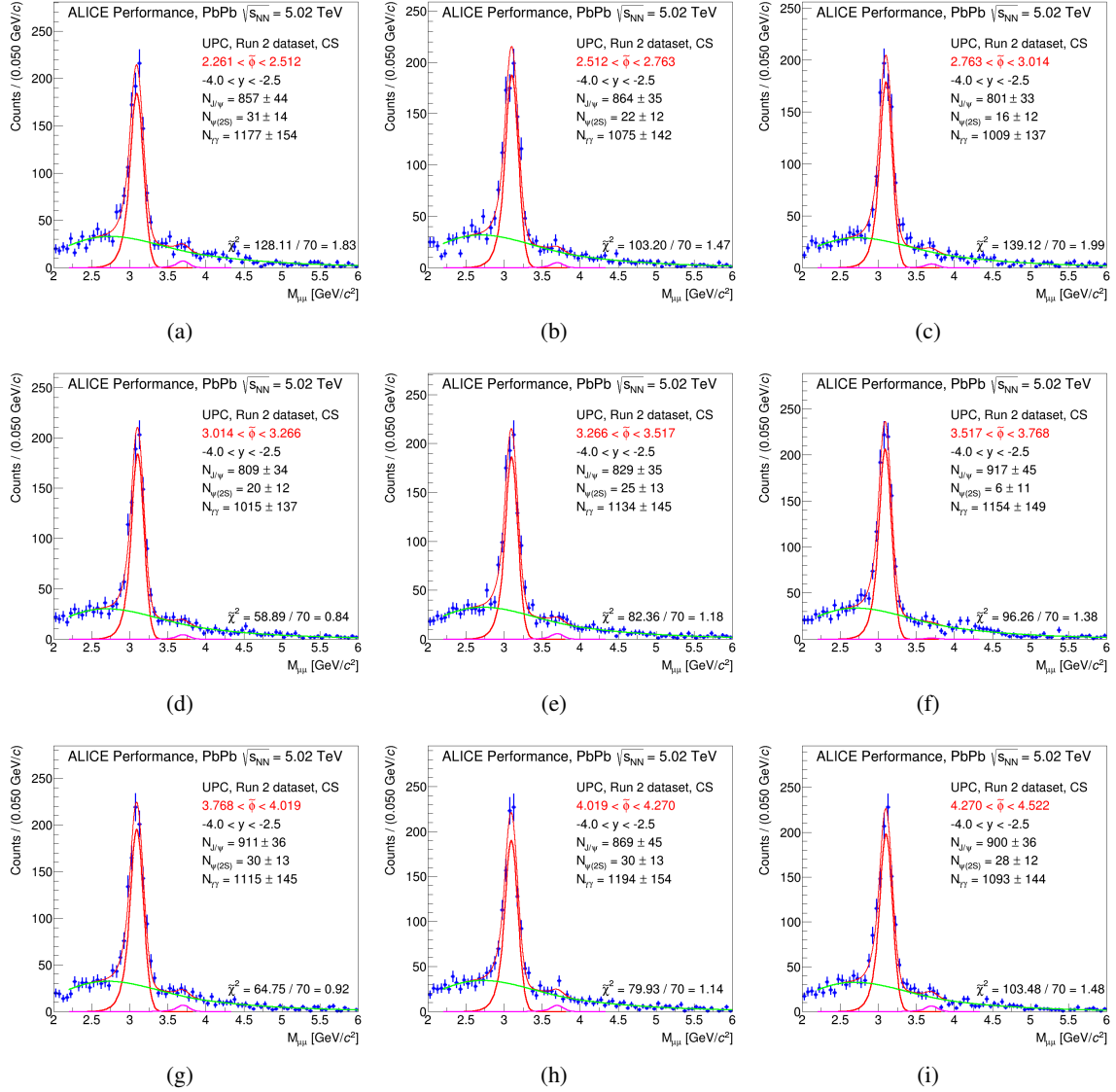


Fig. 32: Signal extraction in $\tilde{\phi}$. From the upper left to the lower right panel, increasing bin in $\tilde{\phi}$.

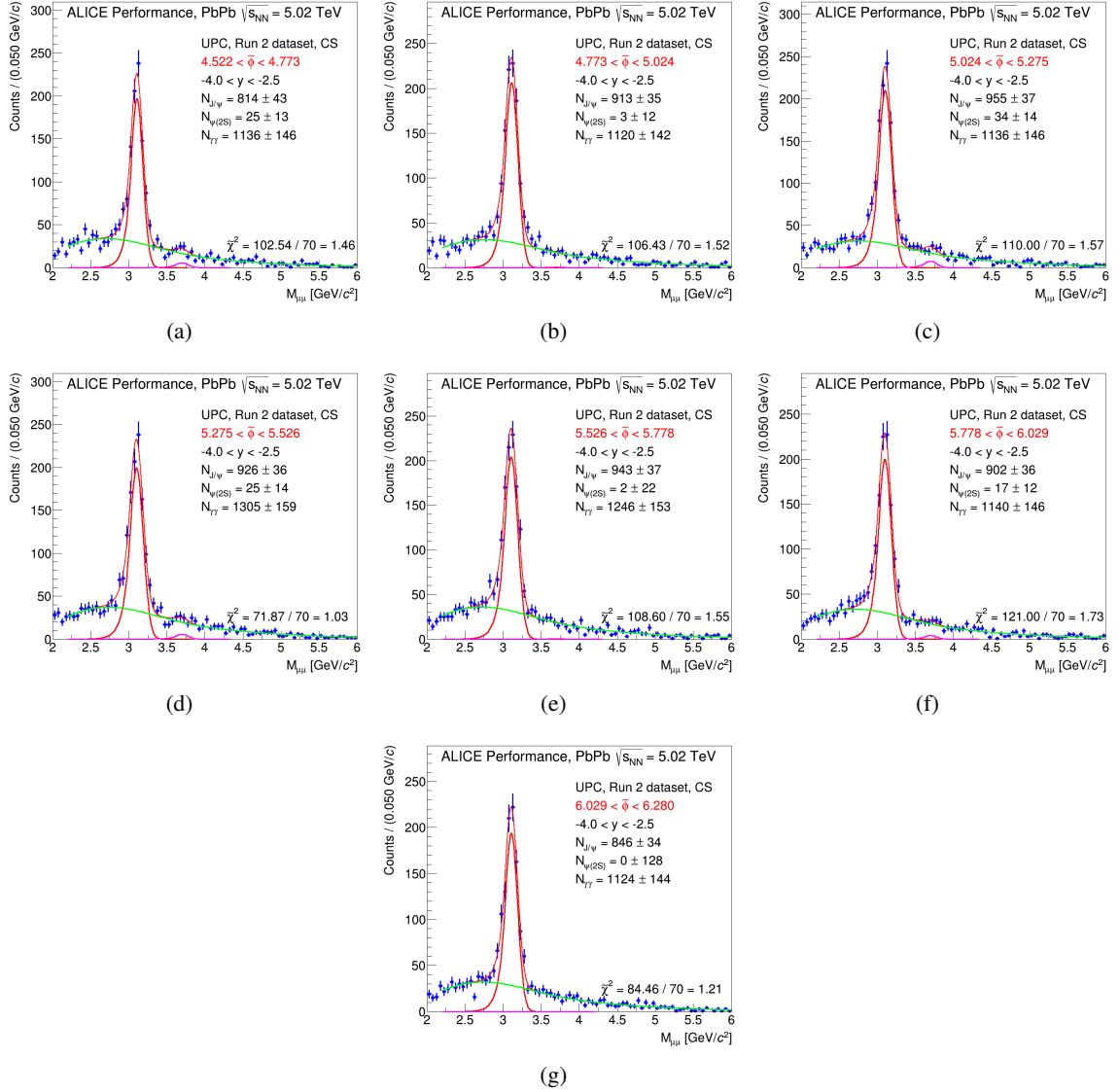


Fig. 33: Signal extraction in $\tilde{\phi}$. From the upper left to the lower right panel, increasing bin in $\tilde{\phi}$.

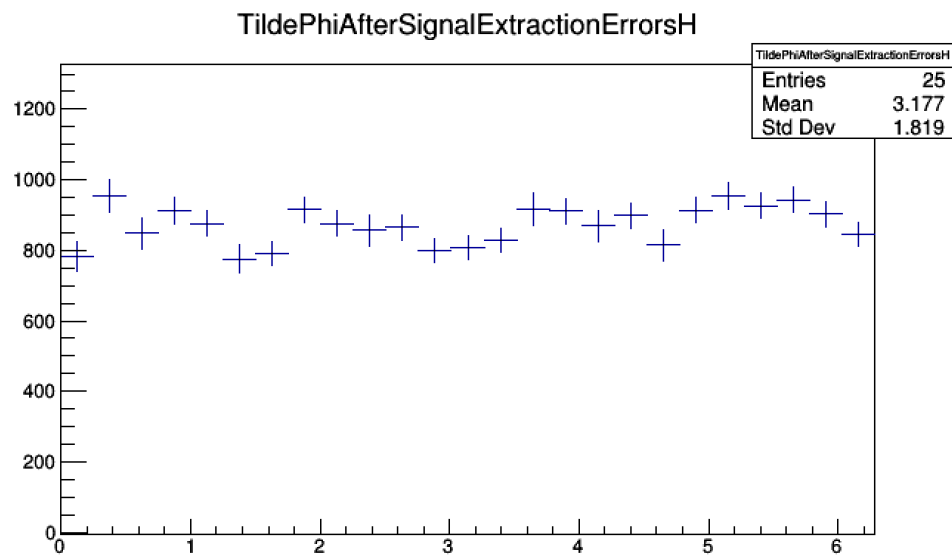


Fig. 34: Raw $\tilde{\phi}$ distribution.

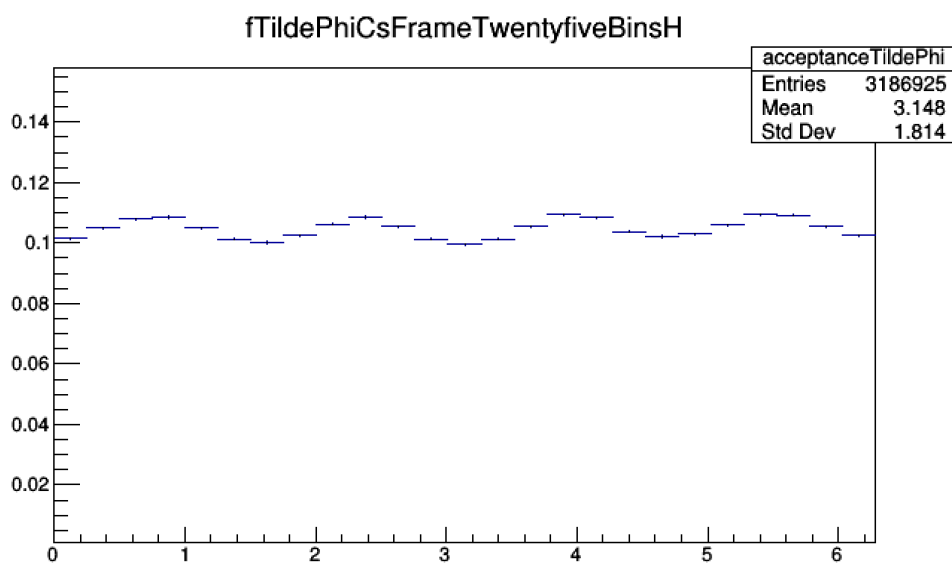


Fig. 35: $A \times \varepsilon$ for the $\tilde{\phi}$ distribution.

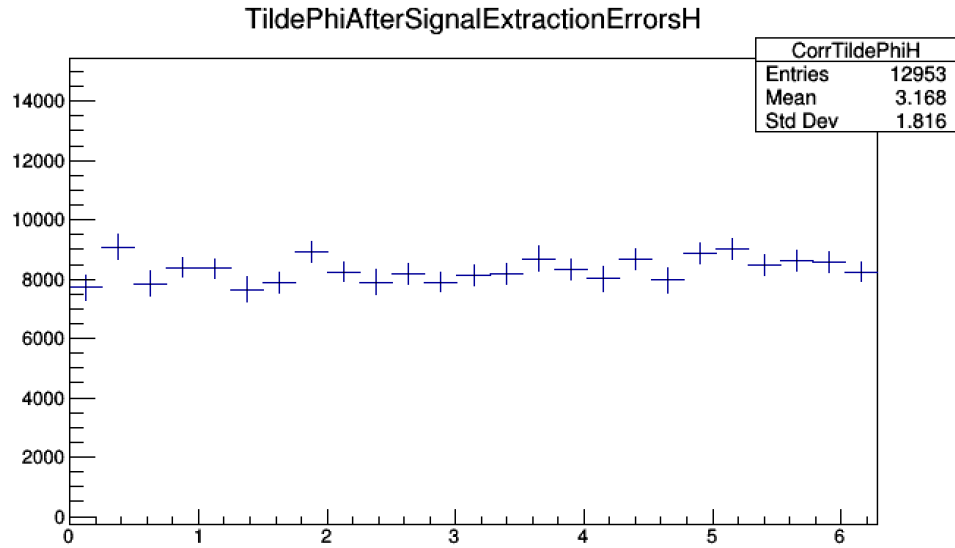


Fig. 36: Corrected $\tilde{\phi}$ distribution.

Table 6: $\frac{dN}{d\phi}$ raw distribution in the CS frame.

Bin number	Range	$\frac{dN}{d\phi}$	Error (stat.)
1	0.000 – 0.252	784	42
2	0.252 – 0.502	953	46
3	0.502 – 0.754	848	44
4	0.754 – 1.005	912	36
5	1.005 – 1.256	877	35
6	1.256 – 1.507	776	41
7	1.507 – 1.758	789	34
8	1.758 – 2.010	916	35
9	2.010 – 2.261	876	35
10	2.261 – 2.512	857	44
11	2.512 – 2.763	864	35
12	2.763 – 3.014	801	33
13	3.014 – 3.266	809	34
14	3.266 – 3.517	829	35
15	3.517 – 3.768	917	45
16	3.768 – 4.019	911	36
17	4.019 – 4.270	869	45
18	4.207 – 4.522	900	36
19	4.522 – 4.773	814	43
20	4.773 – 5.024	913	35
21	5.024 – 5.275	955	37
22	5.275 – 5.526	926	36
23	5.526 – 5.778	943	37
24	5.778 – 6.029	902	36
25	6.029 – 6.280	846	34

310 **6.4 Combined fits**

311 The principal parameter in Eq. 2 is λ_θ . To constrain its value as much as possible, it is fitted together
 312 with the other two distributions too in this 1D analysis. This is because the other two distributions also
 313 depend on λ_θ . A Minuit macro is used to do a simultaneous fit on all distributions. The results are shown
 314 below in Fig. 37(a), 37(b), 37(c).

The fit is performed over the full range in $\cos \theta$, ϕ , $\tilde{\phi}$. The results are the following:

$$\begin{aligned}\lambda_\theta &= 1.326 \pm 0.159, \\ \lambda_\phi &= 0.052 \pm 0.026, \\ \lambda_{\theta\phi} &= -0.038 \pm 0.037.\end{aligned}$$

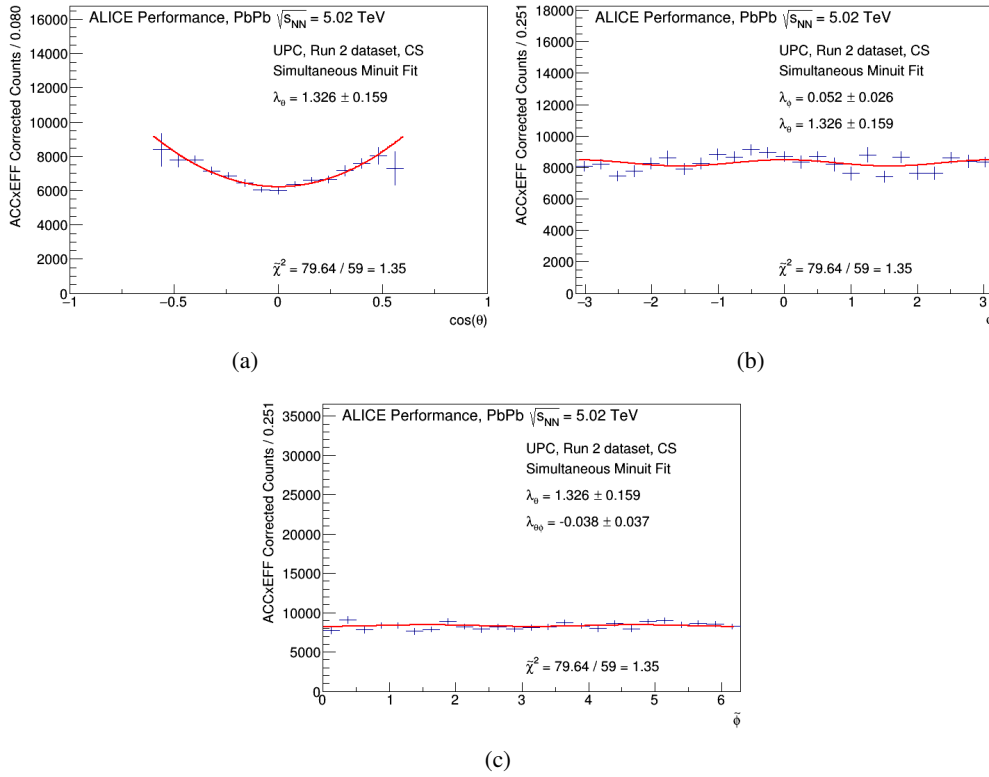


Fig. 37: Simultaneous fit to the distributions.

315 **7 Systematics for the 1D analysis**

316 Several systematic sources have been considered and are listed below:

317 – **J/Ψ mass range:** By default, the dimuon mass spectrum is fitted in the mass range 2.2 to 6.0 GeV.
 318 Different mass ranges are investigated in this systematic study, as listed below.

- 319 – $M_{\mu\mu} = (2.85 \rightarrow 3.35) \text{ GeV}/c^2$
 320 – $M_{\mu\mu} = (2.80 \rightarrow 3.35) \text{ GeV}/c^2$
 321 – $M_{\mu\mu} = (2.90 \rightarrow 3.35) \text{ GeV}/c^2$
 322 – $M_{\mu\mu} = (2.85 \rightarrow 3.40) \text{ GeV}/c^2$
 323 – $M_{\mu\mu} = (2.85 \rightarrow 3.30) \text{ GeV}/c^2$

324 – **$\cos\theta$ range variation:** The $\cos\theta$ distribution has been fitted over a restricted range, owing to limita-
 325 tions in the useful acceptance. This was done as follows. In the default analysis, the outermost
 326 $\cos\theta$ bins are excluded from the fit. This is varied by first removing the outermost *two* bins on
 327 each side, then the outermost three bins.

328 The mass range and $\cos\theta$ range distributions are taken together to produce a single contribution to
 329 the overall systematic error.

330 – **trigger efficiency:** The single muon p_T software varied between 0.85 GeV/ c and 1.15 GeV/ c .

331 – **different acceptance table:** The default acceptance table presupposes transverse polarization.
 332 In order to investigate the effect of the acceptance table on the systematic error, a new acceptance
 333 table based on linear polarization has been generated. Here instead of generating a new distribution
 334 *ab initio*, an acceptance table based on transverse polarization, but with fine binning, has been
 335 reweighted by the required factor to convert it to a flat $\cos\theta$ distribution. The default configuration
 336 is flat in ϕ already. The analysis is then repeated using this new table, and the differences in the
 337 polarization parameters for the same event sample are used to estimate the systematic error.

338 **7.1 Helicity Frame**

339 The results from the variation in the mass cut and $\cos\theta$ ranges are shown in Figs. 38(a), 38(b), and 38(c).
 340 The results from the variation in the single muon p_T cut are shown in Figs. 39(a), 39(b), and 39(c).
 341 The entries in Figs. 39(a) and 39(c) are plotted in terms of “mode numbers”, corresponding to different
 342 combinations of mass and $\cos\theta$ ranges. The mode numbers are explained in Table 7. The contributions
 343 to the overall systematic error are summarized in Table 8.

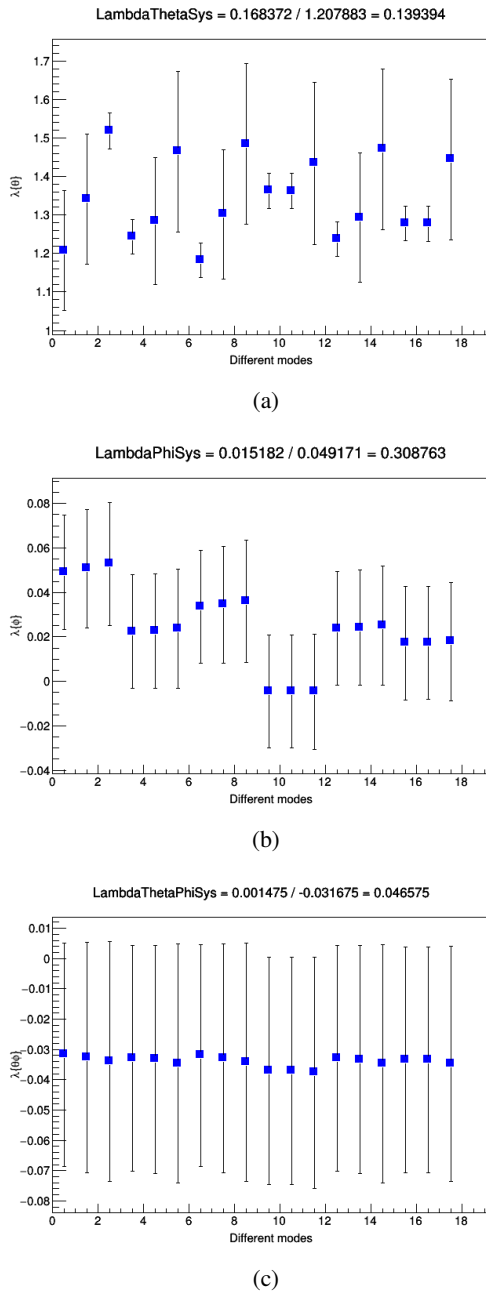


Fig. 38: Signal extraction and fit range variation in $\cos \theta$, ϕ and $\tilde{\phi}$, from the upper to the lower panel, respectively.

Table 7: List of different modes in Fig. 38 and 40 and their mass range and $\cos \theta$ selections. The χ^2/DOF for the fit with the corresponding variation are also given.

Mode No.	χ^2/DOF	Meaning
1	1.39	$M_{\mu\mu} = (2.2 \rightarrow 6.0) \text{ GeV}/c$, standard fit range
2	1.30	$M_{\mu\mu} = (2.2 \rightarrow 6.0) \text{ GeV}/c$, fit range without two bins
3	1.26	$M_{\mu\mu} = (2.2 \rightarrow 6.0) \text{ GeV}/c$, fit range without four bins
4	1.37	$M_{\mu\mu} = (2.85 \rightarrow 3.35) \text{ GeV}/c$, standard fit range
5	1.29	$M_{\mu\mu} = (2.85 \rightarrow 3.35) \text{ GeV}/c$, fit range without two bins
6	1.25	$M_{\mu\mu} = (2.85 \rightarrow 3.35) \text{ GeV}/c$, fit range without four bins
7	1.37	$M_{\mu\mu} = (2.80 \rightarrow 3.35) \text{ GeV}/c$, standard fit range
8	1.29	$M_{\mu\mu} = (2.80 \rightarrow 3.35) \text{ GeV}/c$, fit range without two bins
9	1.25	$M_{\mu\mu} = (2.80 \rightarrow 3.35) \text{ GeV}/c$, fit range without four bins
10	1.67	$M_{\mu\mu} = (2.90 \rightarrow 3.35) \text{ GeV}/c$, standard fit range
11	1.57	$M_{\mu\mu} = (2.90 \rightarrow 3.35) \text{ GeV}/c$, fit range without two bins
12	1.53	$M_{\mu\mu} = (2.90 \rightarrow 3.35) \text{ GeV}/c$, fit range without four bins
13	1.37	$M_{\mu\mu} = (2.85 \rightarrow 3.40) \text{ GeV}/c$, standard fit range
14	1.29	$M_{\mu\mu} = (2.85 \rightarrow 3.40) \text{ GeV}/c$, fit range without two bins
15	1.25	$M_{\mu\mu} = (2.85 \rightarrow 3.40) \text{ GeV}/c$, fit range without four bins
16	1.39	$M_{\mu\mu} = (2.85 \rightarrow 3.30) \text{ GeV}/c$, standard fit range
17	1.30	$M_{\mu\mu} = (2.85 \rightarrow 3.30) \text{ GeV}/c$, fit range without two bins
18	1.29	$M_{\mu\mu} = (2.85 \rightarrow 3.30) \text{ GeV}/c$, fit range without four bins

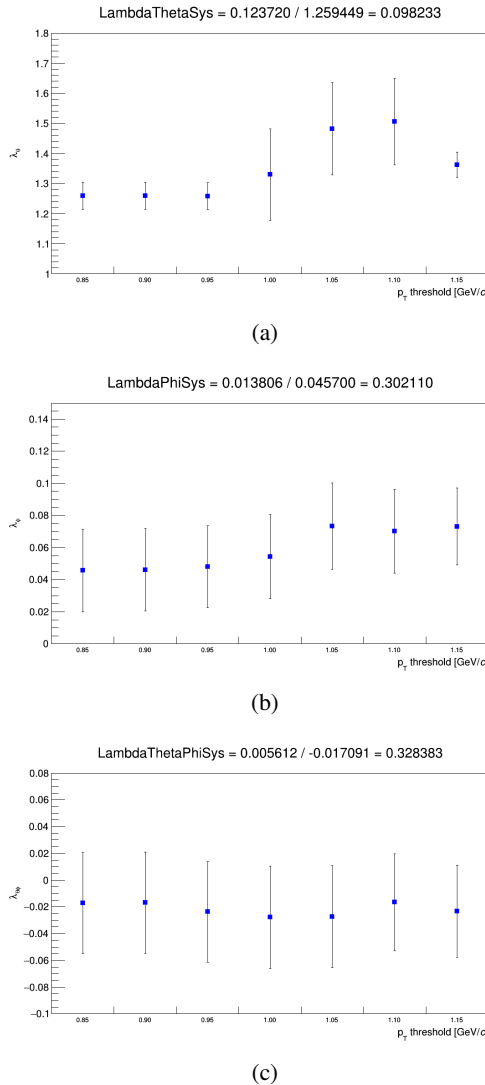


Fig. 39: Trigger variation in $\cos \theta$, ϕ and $\tilde{\phi}$, from the upper to the lower panel, respectively.

Table 8: Systematic uncertainties in the Helicity frame

	λ_θ	λ_ϕ	$\lambda_{\theta\phi}$
Mass and fit range	13.94%	30.87%	4.66%
Trigger efficiency	9.45%	29.38%	3.03%
Acceptance table	2.8%	2.0%	3.1%
TOTAL (%)	17.07%	42.66%	6.36%
TOTAL	0.206	0.021	0.002

344 7.2 Collins Soper Frame

345 The same procedure is applied to the analysis using Collins-Soper axes. Figs. 40(a), 40(b), and 40(c)
 346 show the variation in mass range and $\cos \theta$ range, and Figs. 41(a), 41(b), and 41(c) show the variation
 347 arising from the $p_T^{\text{Trig}}(\mu)$. The results are summarized in Table 9.

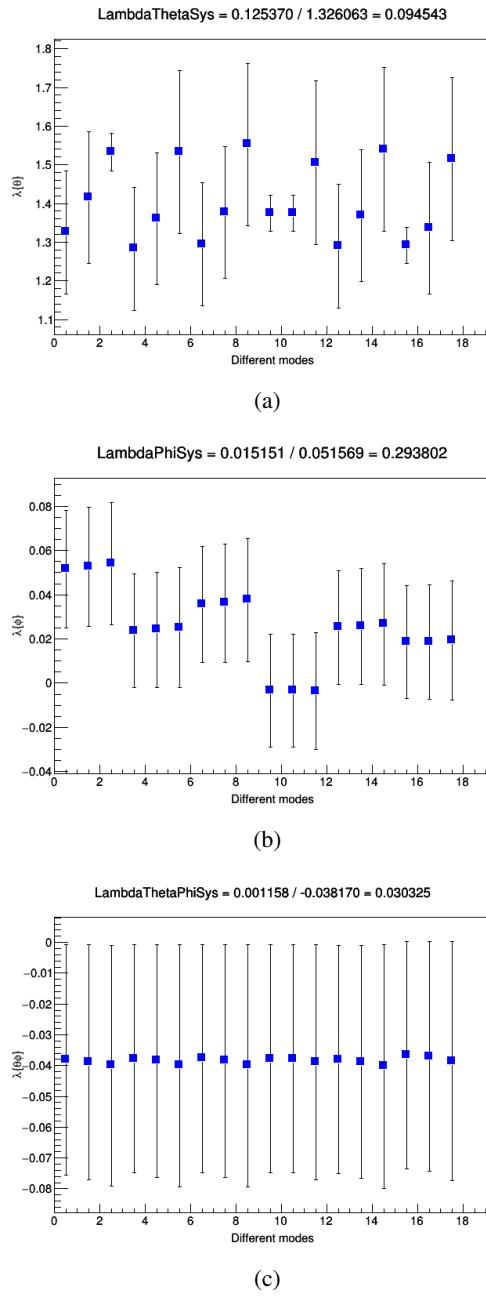


Fig. 40: Signal extraction and fit range variation in $\cos \theta$, ϕ and $\tilde{\phi}$, from the upper to the lower panel, respectively.

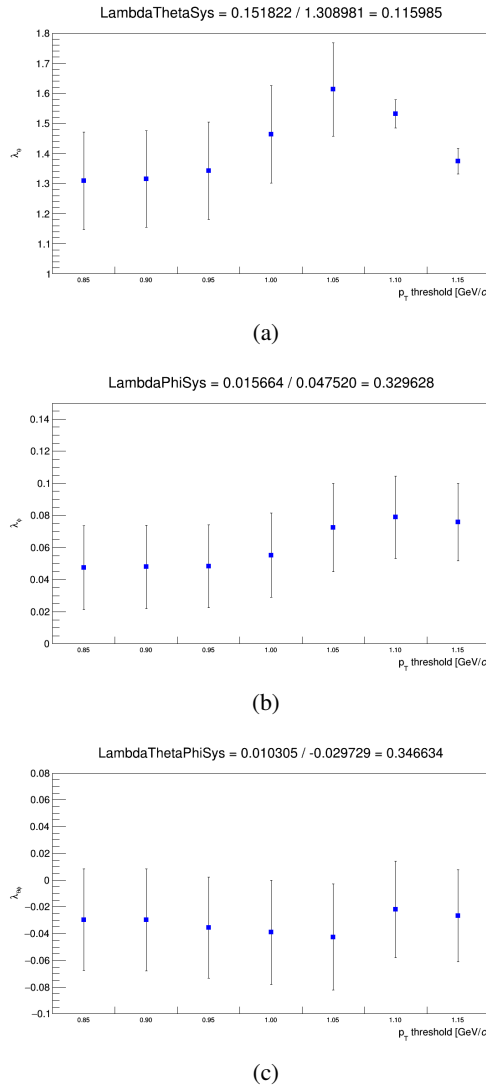


Fig. 41: Trigger variation in $\cos \theta$, ϕ and $\tilde{\phi}$, from the upper to the lower panel, respectively.

Table 9: Systematic uncertainties in the Collins-Soper frame

	λ_θ	λ_ϕ	$\lambda_{\theta\phi}$
Mass and fit range	9.82%	30.21%	32.84%
Trigger efficiency	11.59%	32.96%	34.66%
Acceptance table	2.8%	2.0%	3.1%
TOTAL (%)	15.45%	44.76%	47.85%
TOTAL	0.205	0.023	0.018

³⁴⁸ **8 Conclusions**

³⁴⁹ The 1D analysis presented above and the 2D analysis in the Appendix, in both Helicity and Collins-Soper
³⁵⁰ Frames, show similar results, and agree within statistical uncertainties.

³⁵¹ Thus, the J/ Ψ polarization is consistent with the hypothesis of transverse polarization ($[\lambda_\theta, \lambda_\phi, \lambda_{\theta\phi}] =$
³⁵² $[1, 0, 0]$) within the statistical uncertainties.

³⁵³ Including both statistical and systematic uncertainties, we obtain for the Helicity frame in 1D:

$$\begin{aligned}\lambda_\theta &= 1.208 \pm 0.155 \text{ (stat.)} \pm 0.215 \text{ (sys.)}, \\ \lambda_\phi &= 0.049 \pm 0.026 \text{ (stat.)} \pm 0.022 \text{ (sys.)}, \\ \lambda_{\theta\phi} &= -0.032 \pm 0.037 \text{ (stat.)} \pm 0.005 \text{ (sys.)}.\end{aligned}$$

³⁵⁴ while for the Collins-Soper frame in 1D we obtain:

$$\begin{aligned}\lambda_\theta &= 1.326 \pm 0.159 \text{ (stat.)} \pm 0.204 \text{ (sys.)}, \\ \lambda_\phi &= 0.052 \pm 0.026 \text{ (stat.)} \pm 0.023 \text{ (sys.)}, \\ \lambda_{\theta\phi} &= -0.038 \pm 0.037 \text{ (stat.)} \pm 0.018 \text{ (sys.)}.\end{aligned}$$

355 **Appendix**

356 **A Invariant Mass Fits for 2D signal extraction in the Helicity frame**

357 As a cross-check of the results obtained from the “1D” analysis of the angular distributions, projected
 358 onto the $\cos \theta$, ϕ and $\tilde{\phi}$ distributions, we have also fitted the joint $(\cos \theta, \phi)$ distribution in a two-
 359 dimensional approach. This is done doing a log. likelihood fit to the 2D distributions. Variable bins
 360 are used in order to obtain adequate statistics in each $(\cos \theta, \phi)$ bin. The bin boundaries are given below.

$$\begin{aligned} \cos \theta = & -0.65, -0.35, -0.15, -0.05, 0.05, 0.15, 0.35, 0.65; \\ \phi / (0.05 \times 3.14) = & -20, -19, -18, -17, -13, -9, -6, -4, -2, -1, 0, \\ & +1, +2, +4, +6, +9, +13, +17, +18, +19, +20. \end{aligned} \quad (\text{A.1})$$

361 The raw distribution is shown in Fig. A.1, the $A \times \varepsilon$ correction in Fig. A.5, and the $A \times \varepsilon$ corrected
 362 distribution in Fig. A.2. As can be seen, despite the variable binning there are some $(\cos \theta, \phi)$ bins
 363 in which relatively few events are recorded. These tend to be in low-acceptance zones, where large
 364 acceptance factors are required to correct the distributions. These lead to there being a few bins with
 365 large fluctuations.

366 In order to investigate the effect of these outlier bins, the fit was performed in two ways. First, all the
 367 bins were used in the fit, using a pre-prepared ROOT macro, and in addition a fit was performed using a
 368 customised macro accessing MINUIT directly, in which it was possible to mask specific bins explicitly.
 369 It was verified that, with no masking, the two methods give very similar results. Fig. A.3 shows the
 370 ROOT fit to the 2D distribution while Fig. A.4 shows the fit done with the MINUIT macro, with no bins
 371 excluded.

372 The results for the 2D Helicity frame fits are summarized in Table A.1.

Table A.1: Results from the fits for the 2D Helicity frame.

	λ_θ	λ_ϕ	$\lambda_{\theta\phi}$	χ^2/NDF
ROOT - all bins	1.076 ± 0.128	0.005 ± 0.014	0.077 ± 0.029	1.11
TMinuit - all bins	1.077 ± 0.129	0.003 ± 0.014	0.070 ± 0.029	1.11

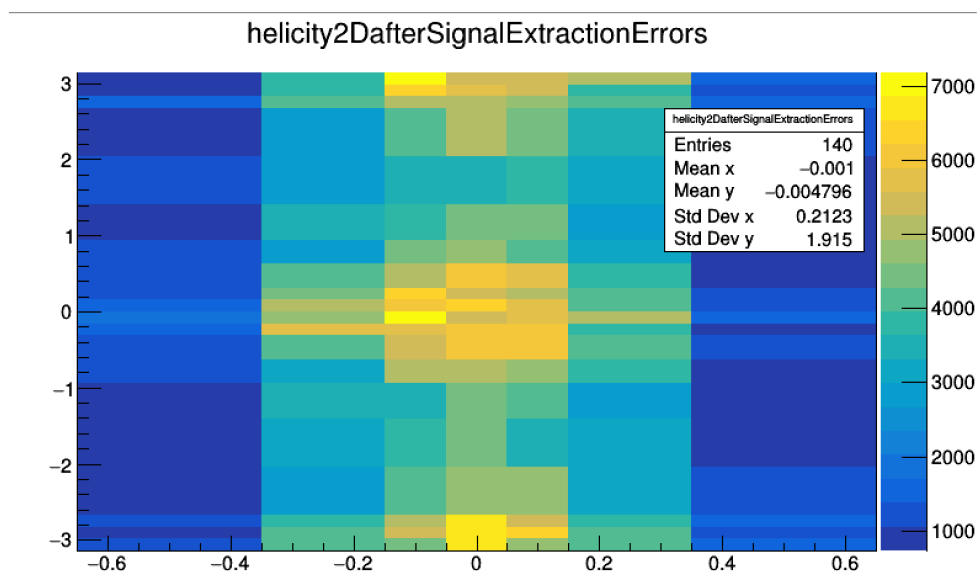


Fig. A.1: The raw distribution before correction. The x -axis shows the $\cos \theta$, while the y -axis the ϕ .

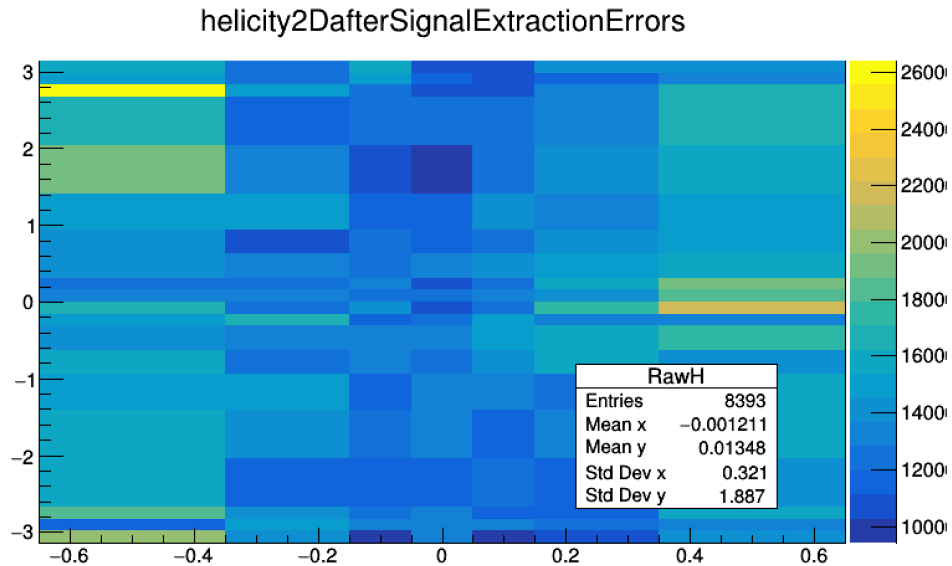


Fig. A.2: The $A \times \varepsilon$ corrected 2D distribution.

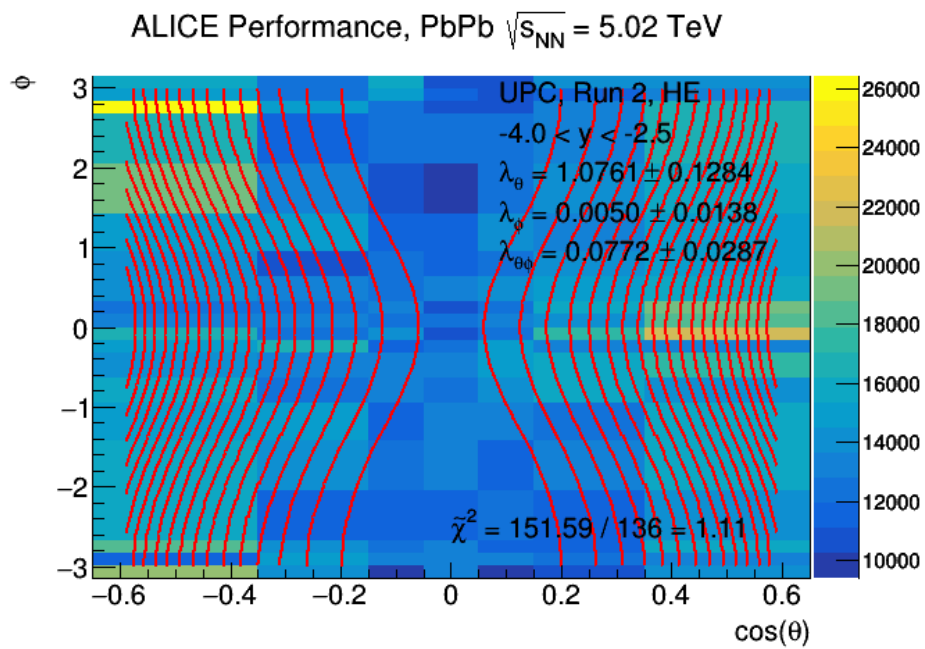


Fig. A.3: The ROOT fit to the 2D distribution.

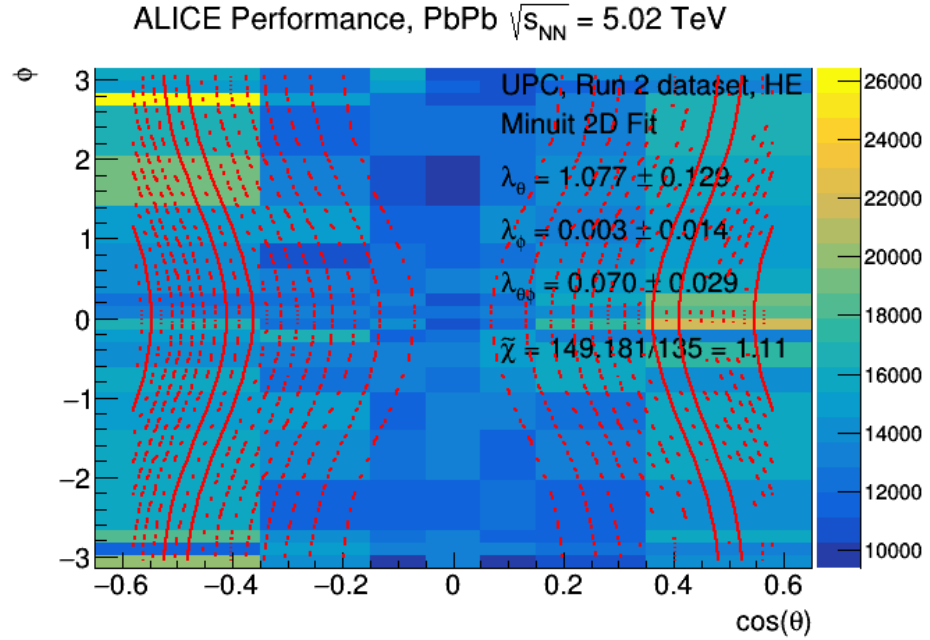


Fig. A.4: The Minuit fit to the 2D distribution.

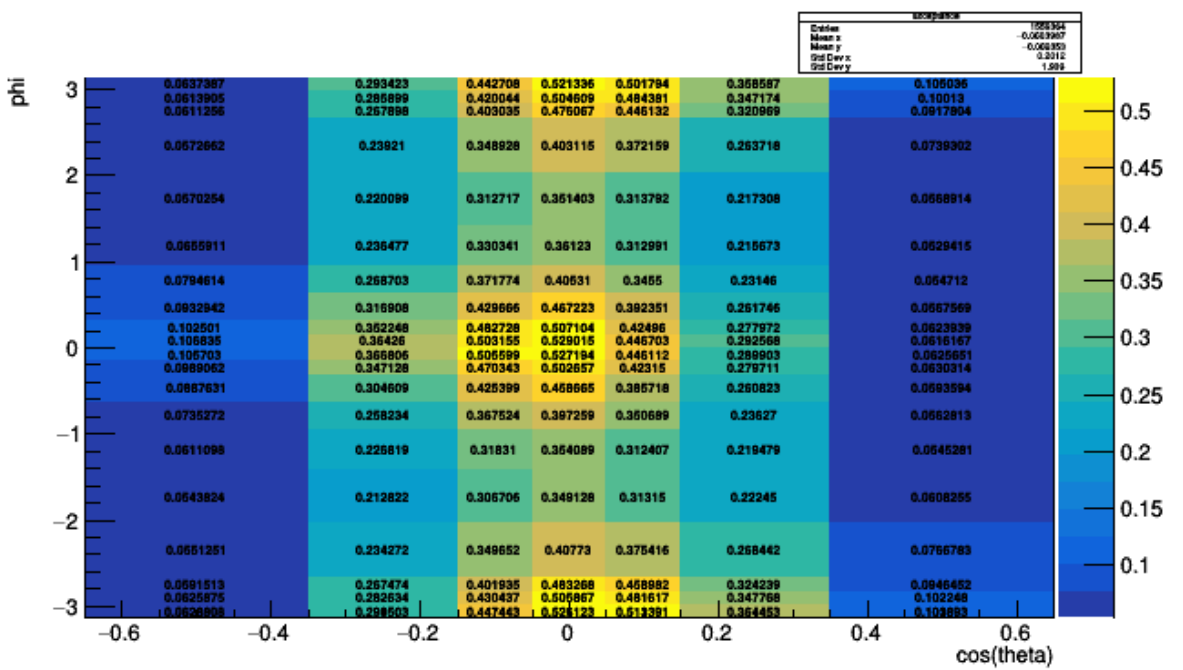


Fig. A.5: The $A \times \epsilon$ for the 2D distribution.

373 **A.1 Yield extraction for the 2D analysis**

374 The yields used in this 2D analysis, along with the $\cos\theta$ and ϕ bins they refer to, are shown in
 375 Figs. A.6, A.7, A.8, A.9, A.10, A.11, A.12, A.13, A.14, A.15, A.16, A.17, A.18, A.19.

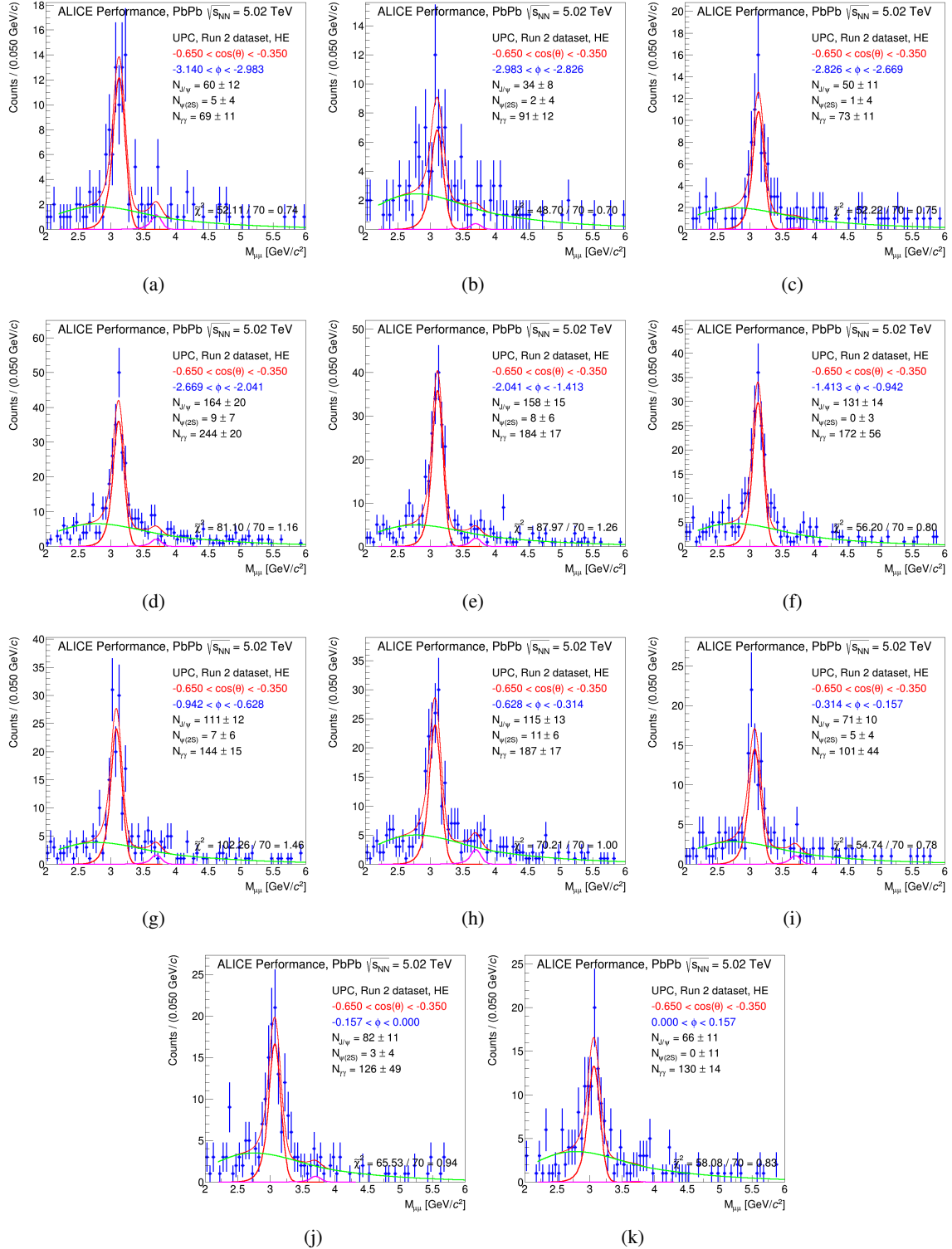


Fig. A.6: Signal extraction in the (-0.65, -0.35) bin in $\cos\theta$. From the upper left to the lower right panel, increasing bin in ϕ , from 0 to 10.

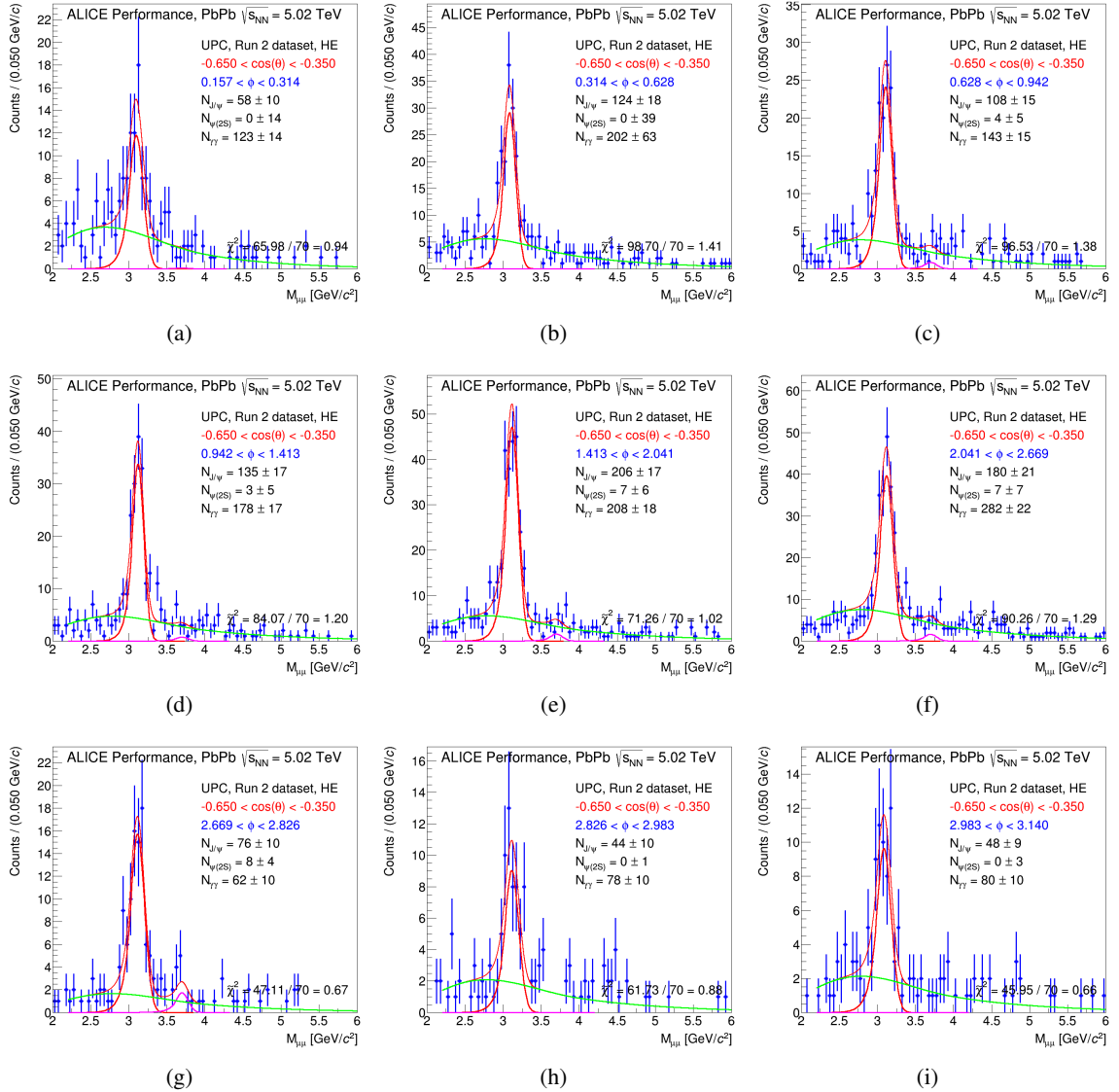


Fig. A.7: Signal extraction in the (-0.65, -0.35) bin in $\cos \theta$. From the upper left to the lower right panel, increasing bin in ϕ , from 11 to 19.

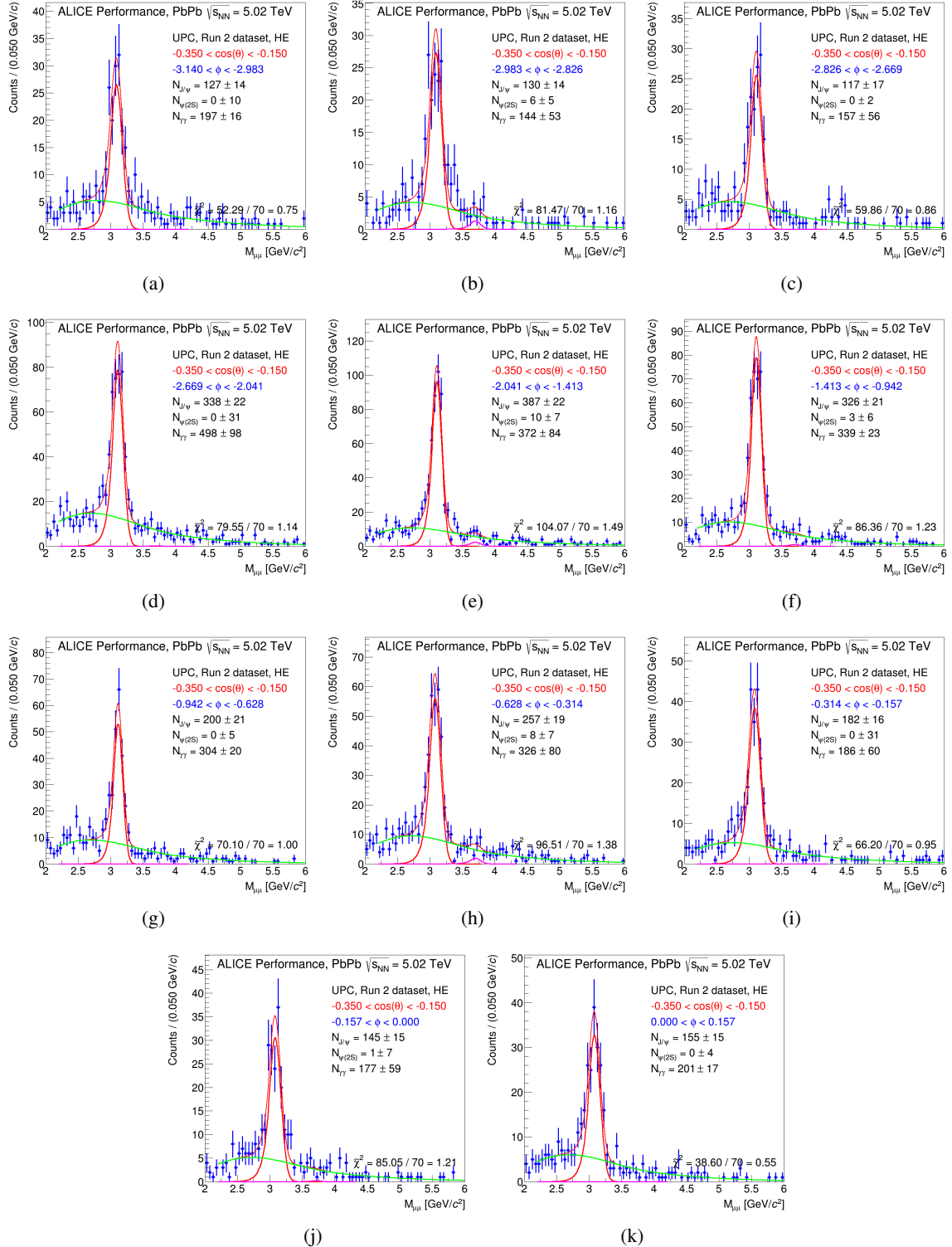


Fig. A.8: Signal extraction in the (-0.35, -0.15) bin in $\cos \theta$. From the upper left to the lower right panel, increasing bin in ϕ , from 0 to 10.

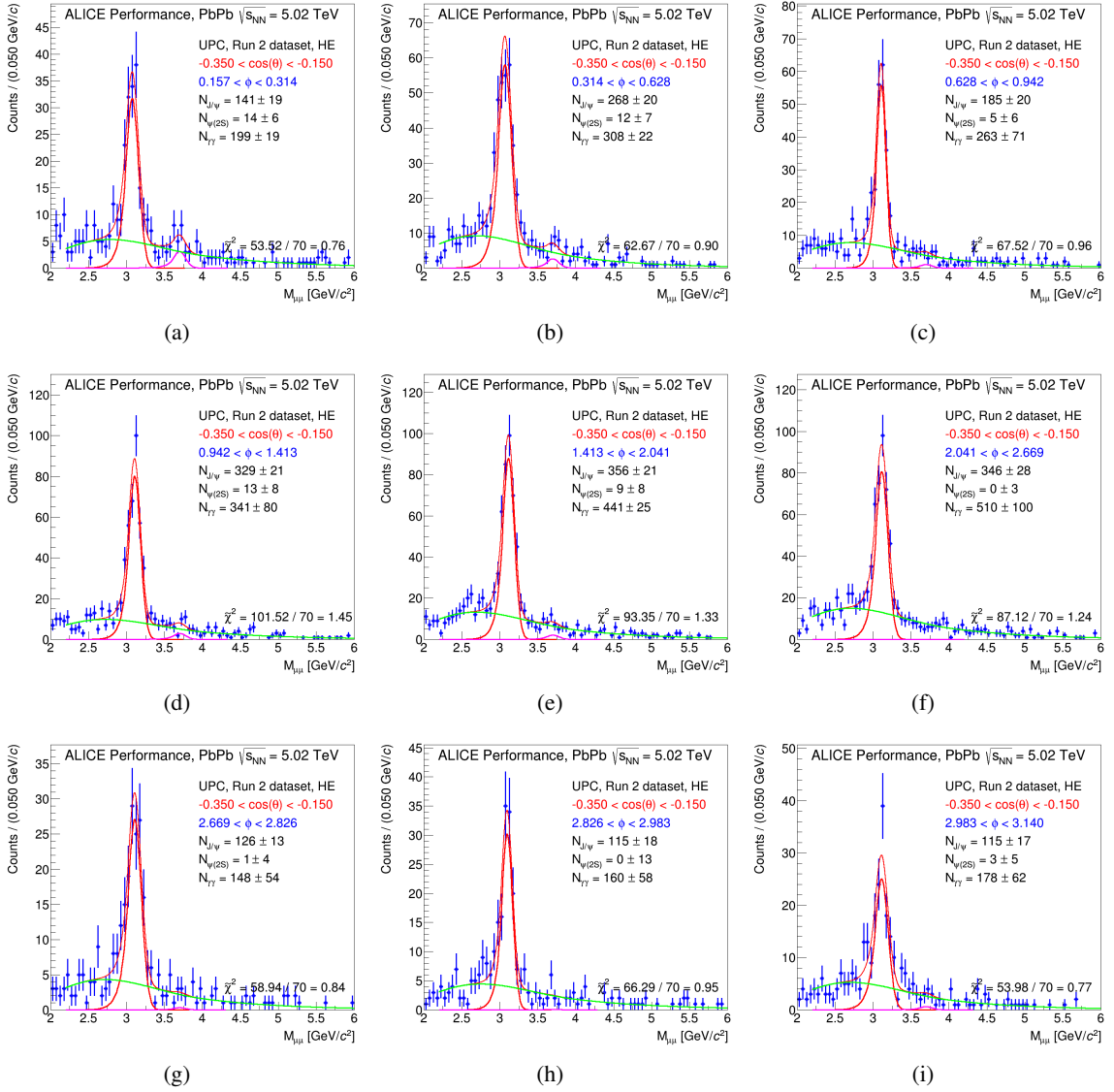


Fig. A.9: Signal extraction in the (-0.35, -0.15) bin in $\cos \theta$. From the upper left to the lower right panel, increasing bin in ϕ , from 11 to 19.

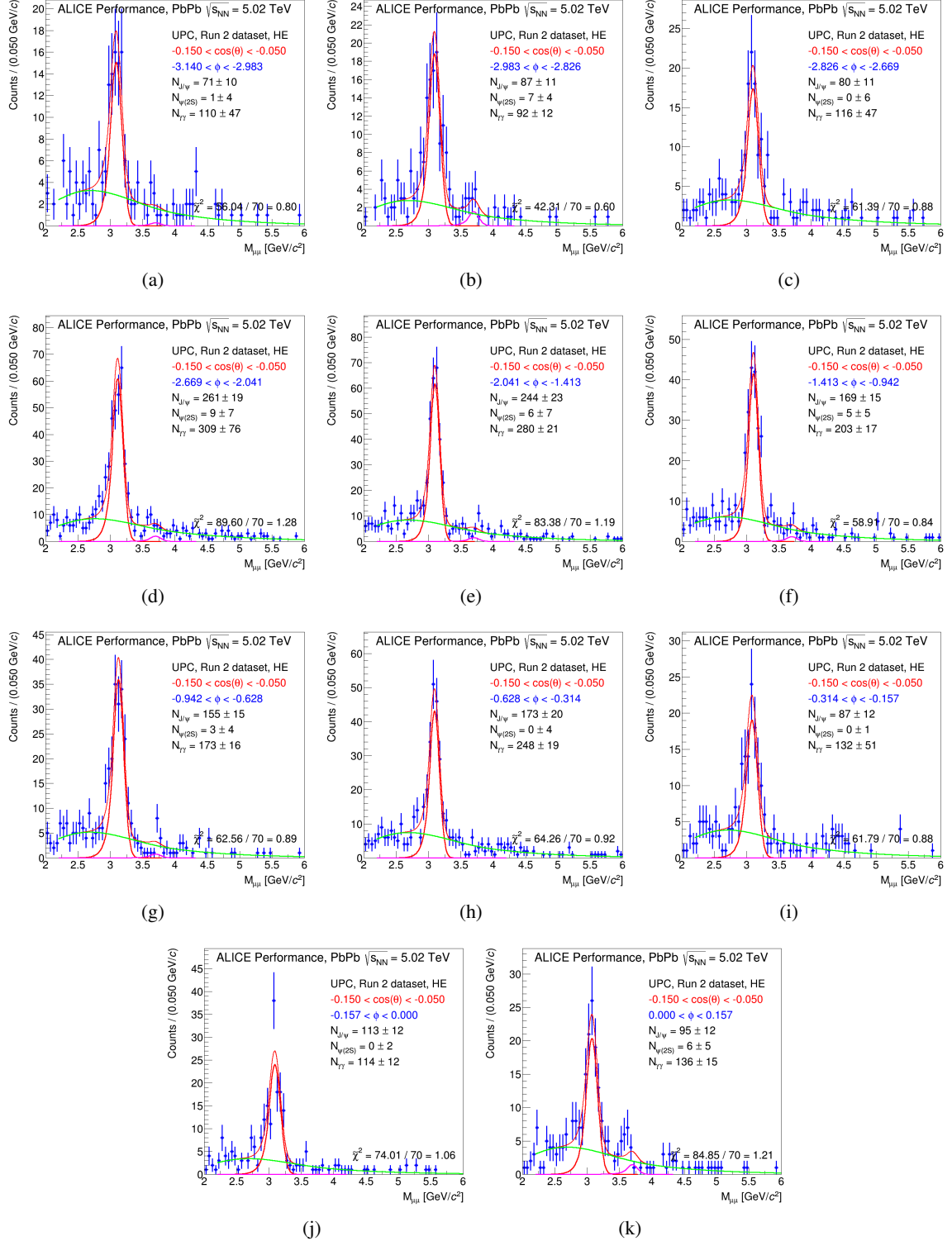


Fig. A.10: Signal extraction in the (-0.15, -0.05) bin in $\cos\theta$. From the upper left to the lower right panel, increasing bin in ϕ , from 0 to 10.

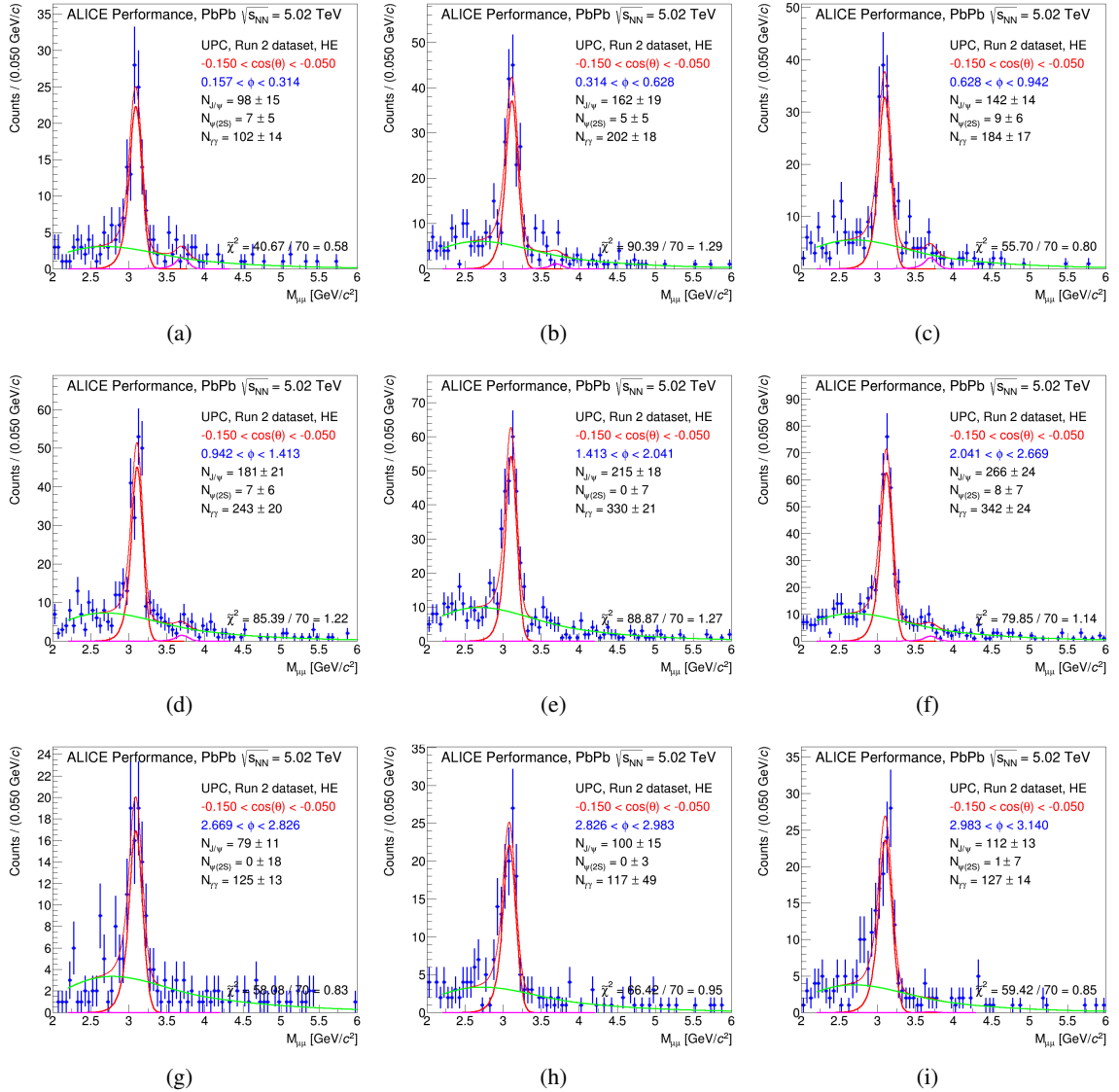


Fig. A.11: Signal extraction in the (-0.15, -0.05) bin in $\cos \theta$. From the upper left to the lower right panel, increasing bin in ϕ , from 11 to 19.

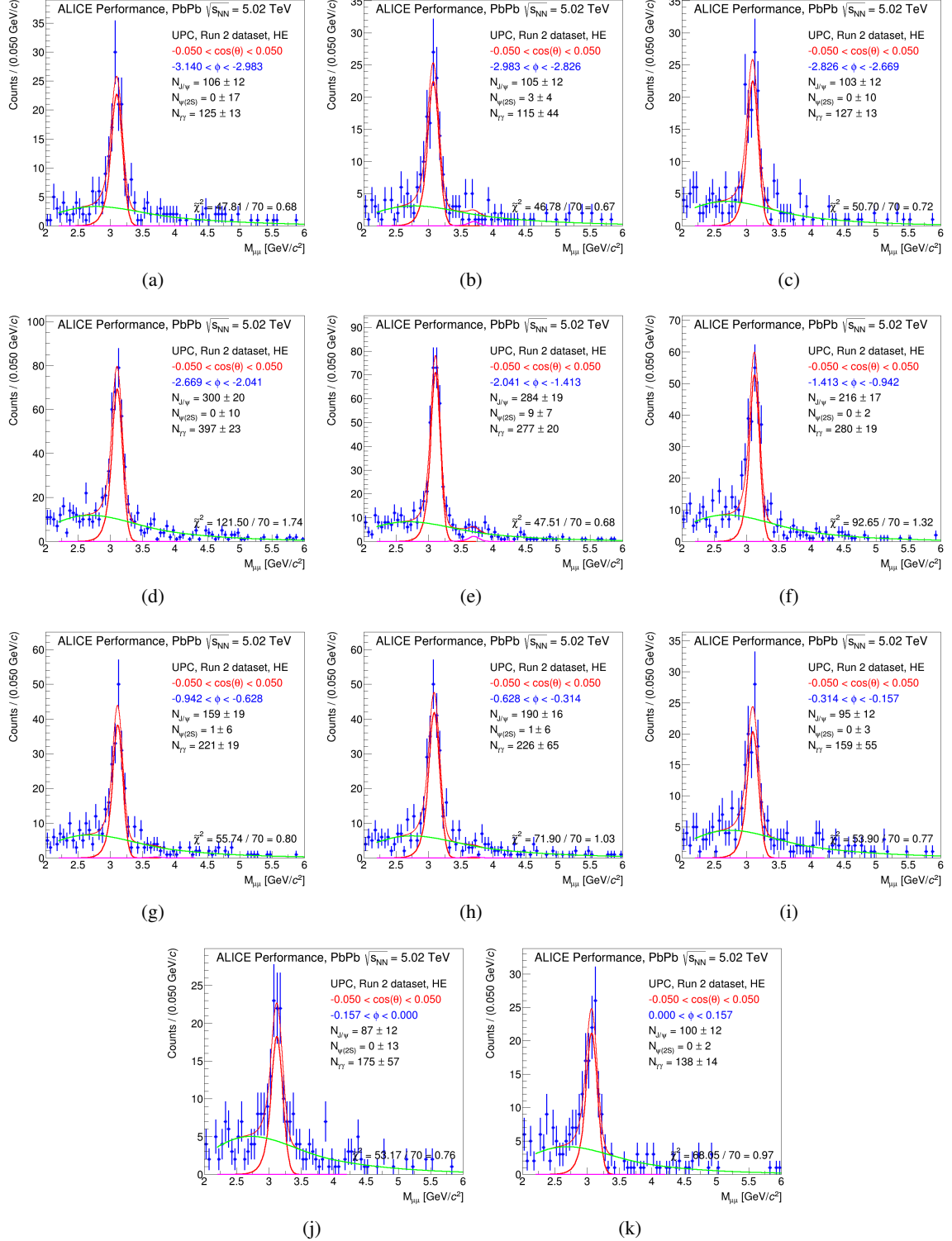


Fig. A.12: Signal extraction in the $(-0.05, +0.05)$ bin in $\cos\theta$. From the upper left to the lower right panel, increasing bin in ϕ , from 0 to 10.

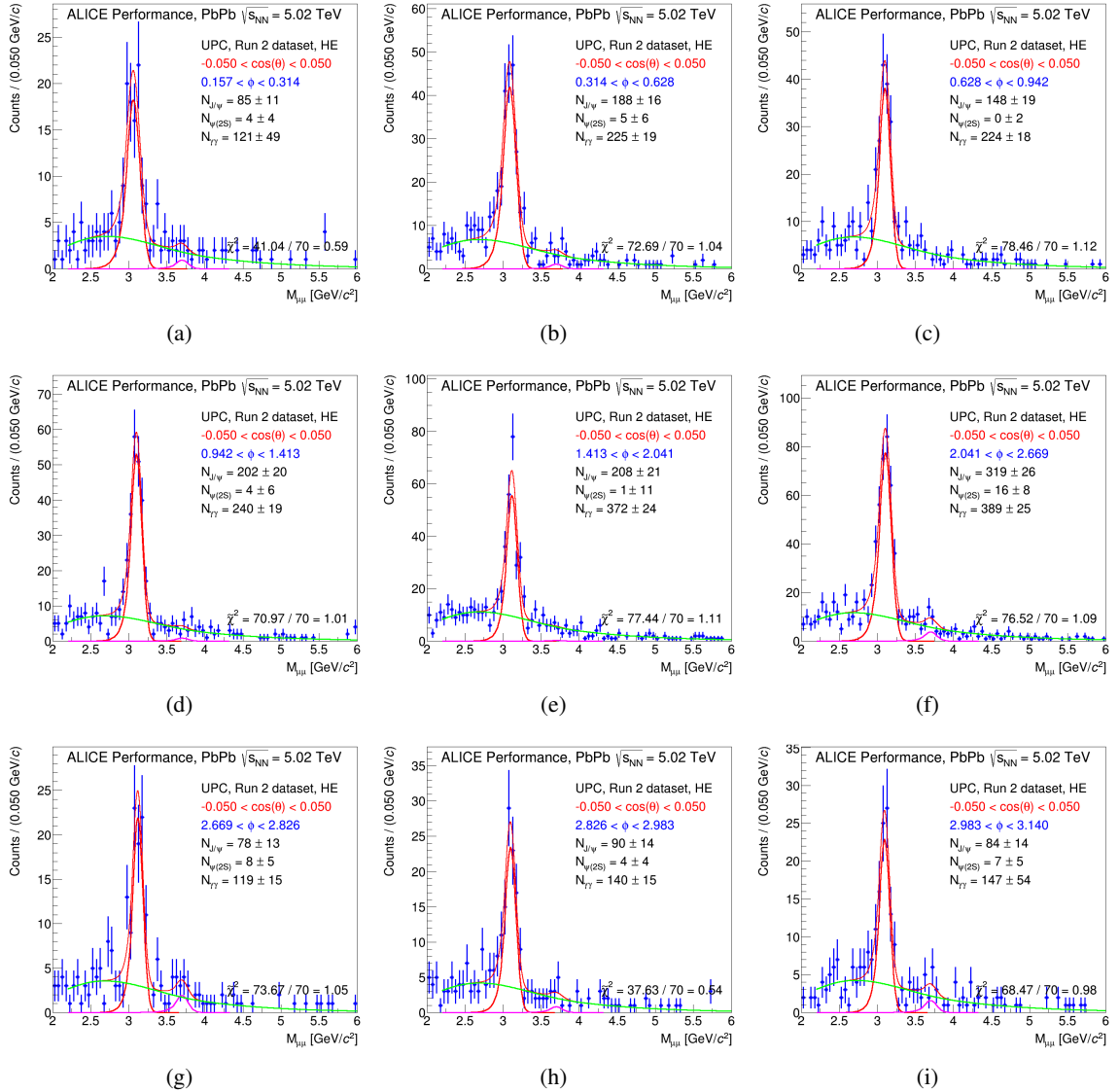


Fig. A.13: Signal extraction in the (-0.05, +0.05) bin in $\cos \theta$. From the upper left to the lower right panel, increasing bin in ϕ , from 11 to 19.

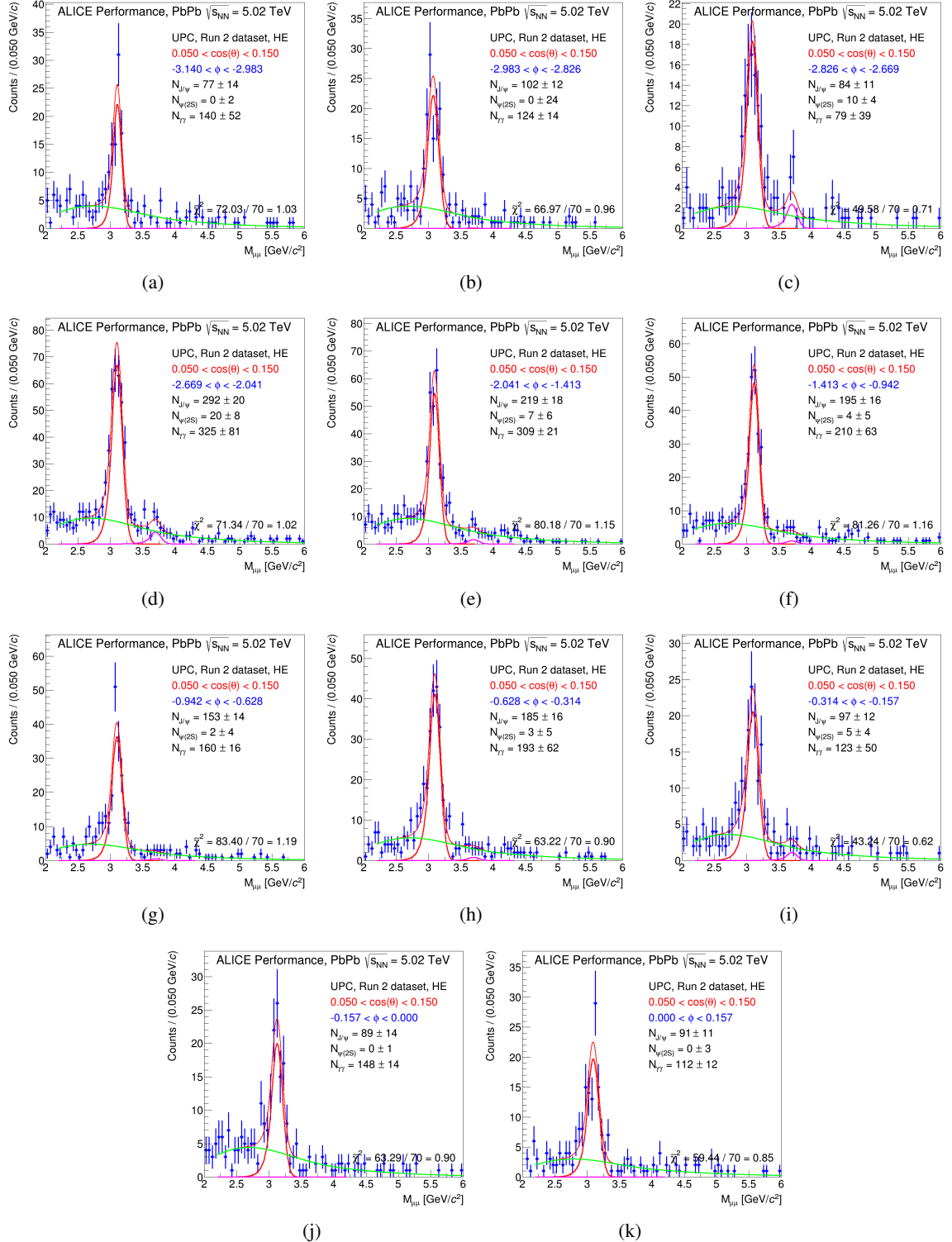


Fig. A.14: Signal extraction in the $(+0.05, +0.15)$ bin in $\cos\theta$. From the upper left to the lower right panel, increasing bin in ϕ , from 0 to 10.

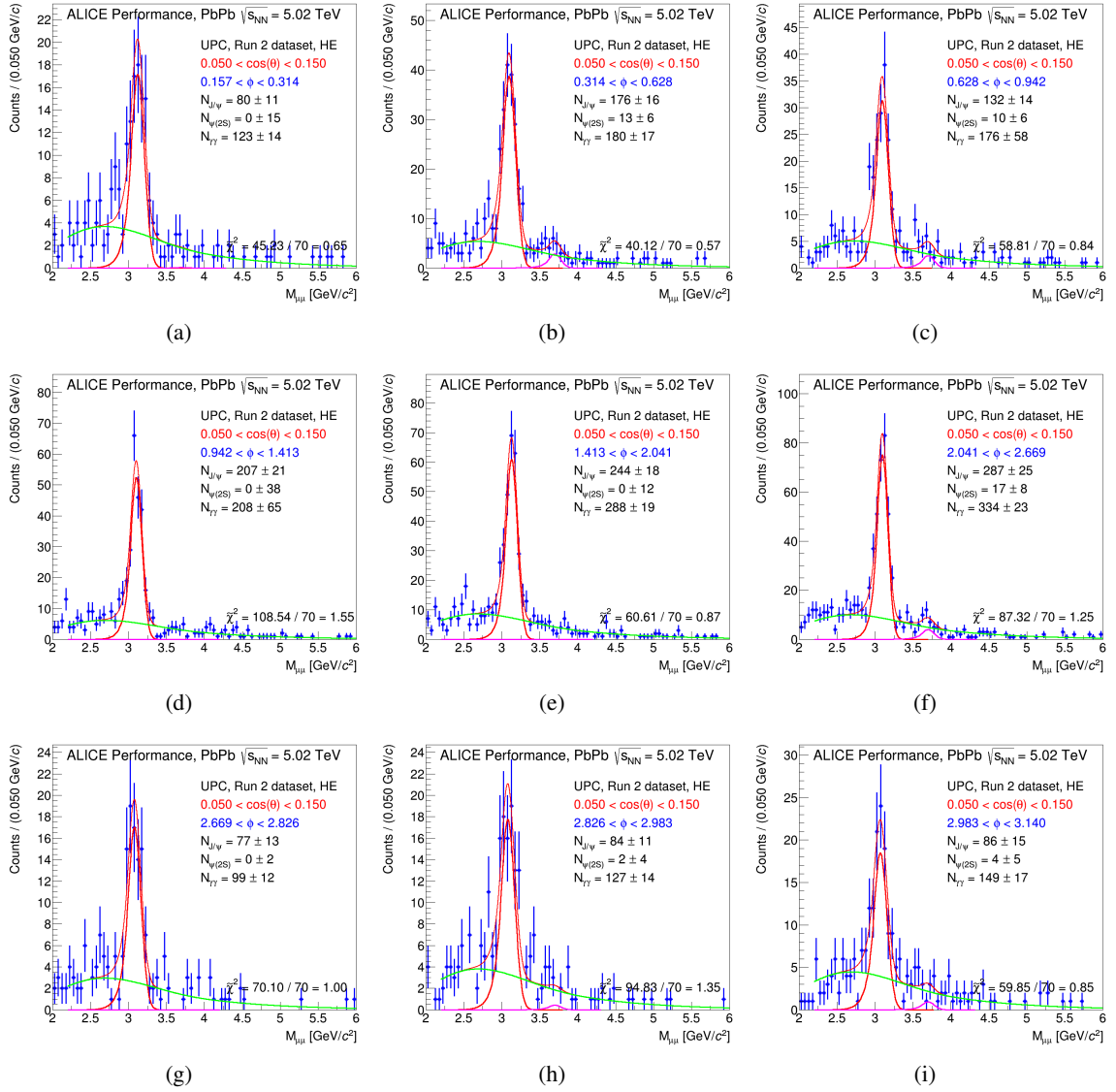


Fig. A.15: Signal extraction in the (+0.05, +0.15) bin in $\cos \theta$. From the upper left to the lower right panel, increasing bin in ϕ , from 11 to 19.

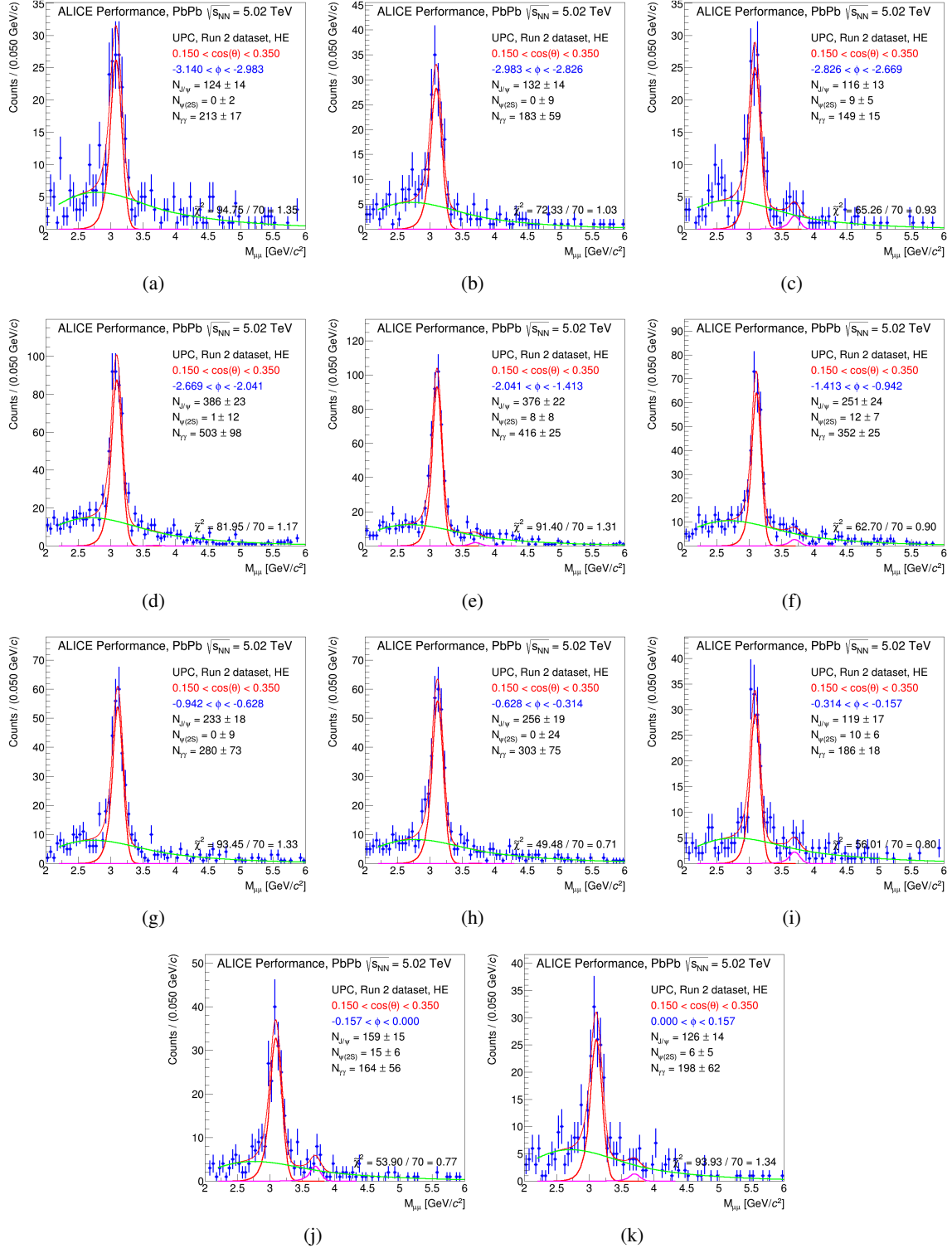


Fig. A.16: Signal extraction in the $(+0.15, +0.35)$ bin in $\cos\theta$. From the upper left to the lower right panel, increasing bin in ϕ , from 0 to 10.

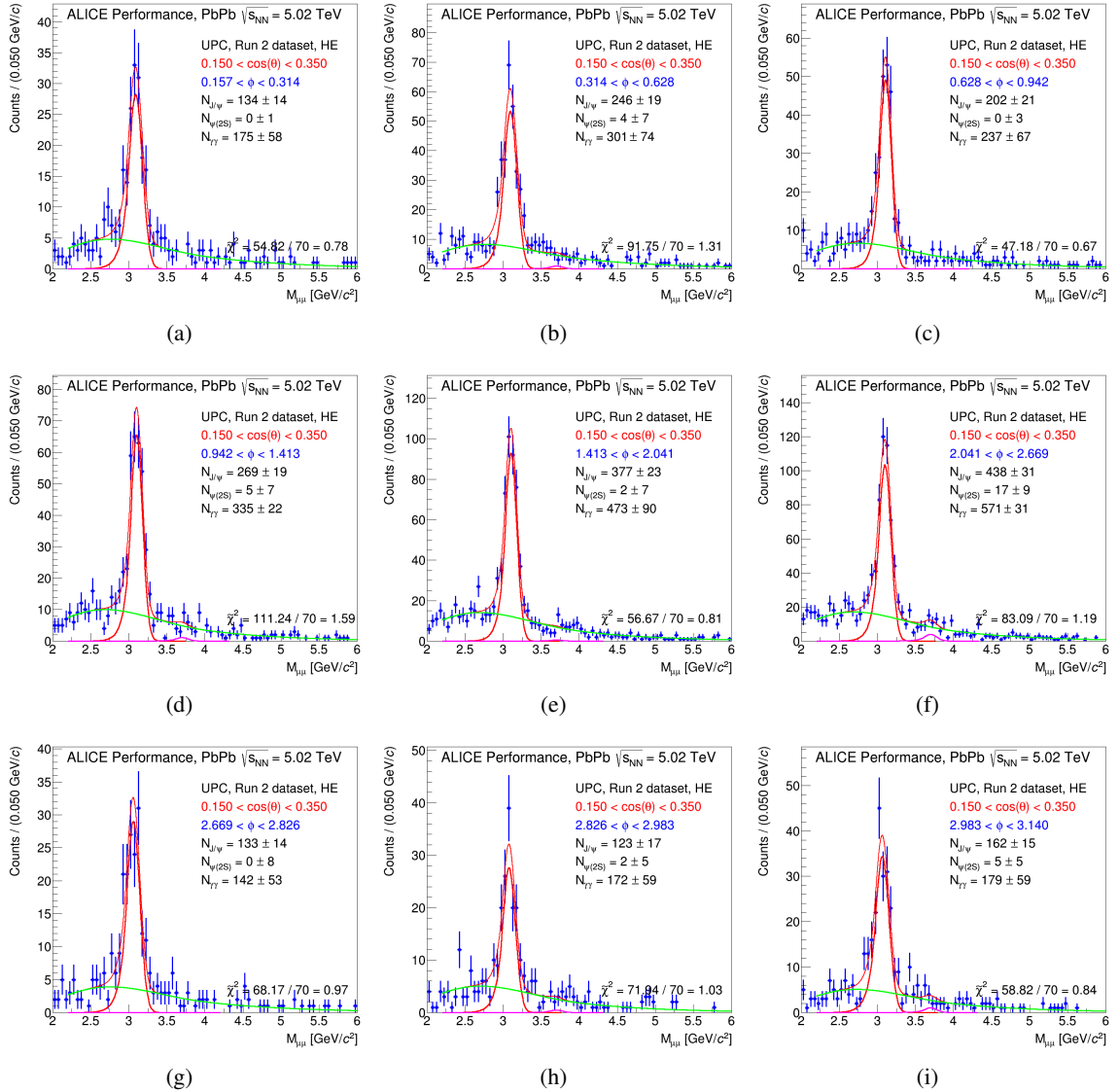


Fig. A.17: Signal extraction in the (+0.15, +0.35) bin in $\cos \theta$. From the upper left to the lower right panel, increasing bin in ϕ , from 11 to 19.

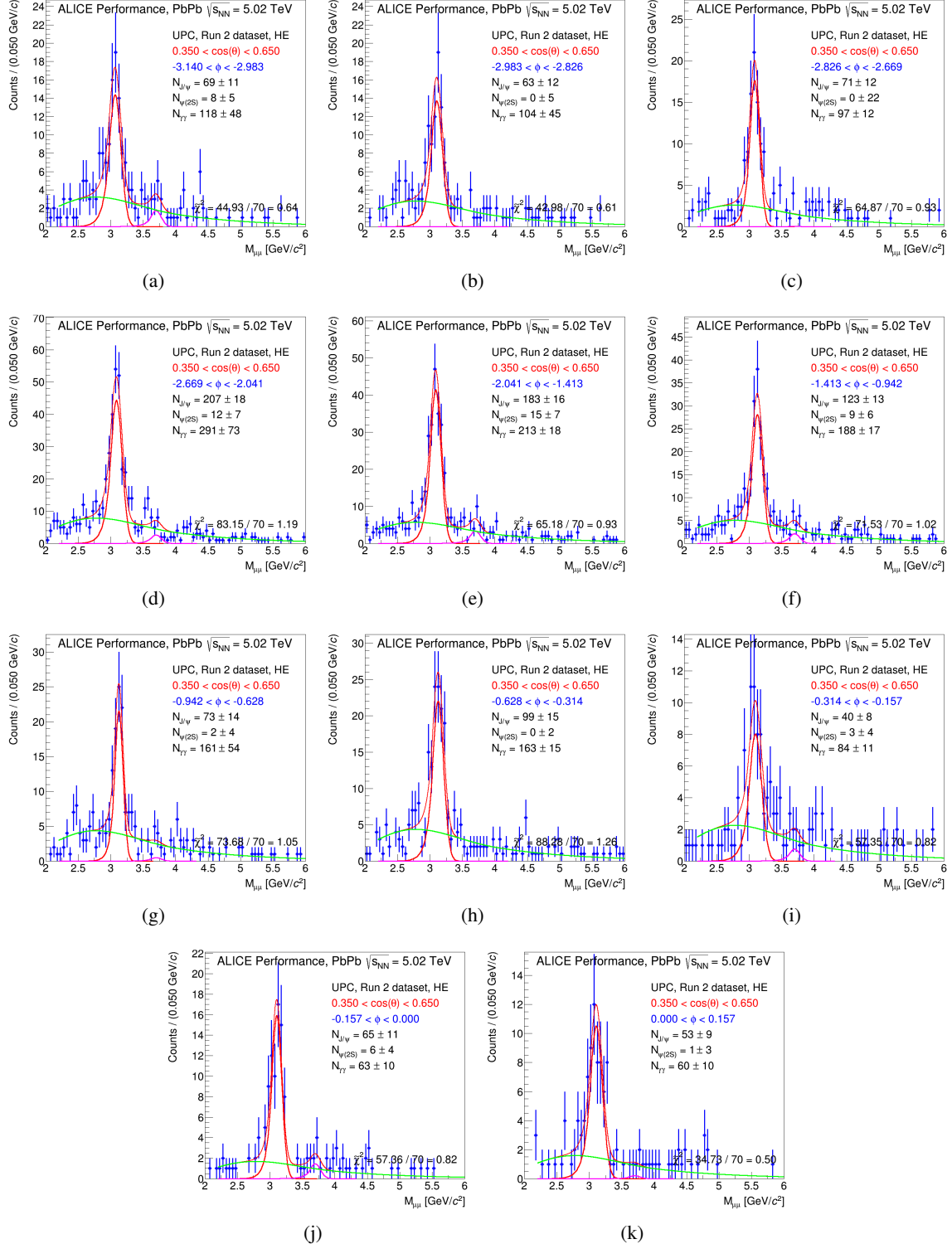


Fig. A.18: Signal extraction in the (+0.35, +0.65) bin in $\cos \theta$. From the upper left to the lower right panel, increasing bin in ϕ , from 0 to 10.

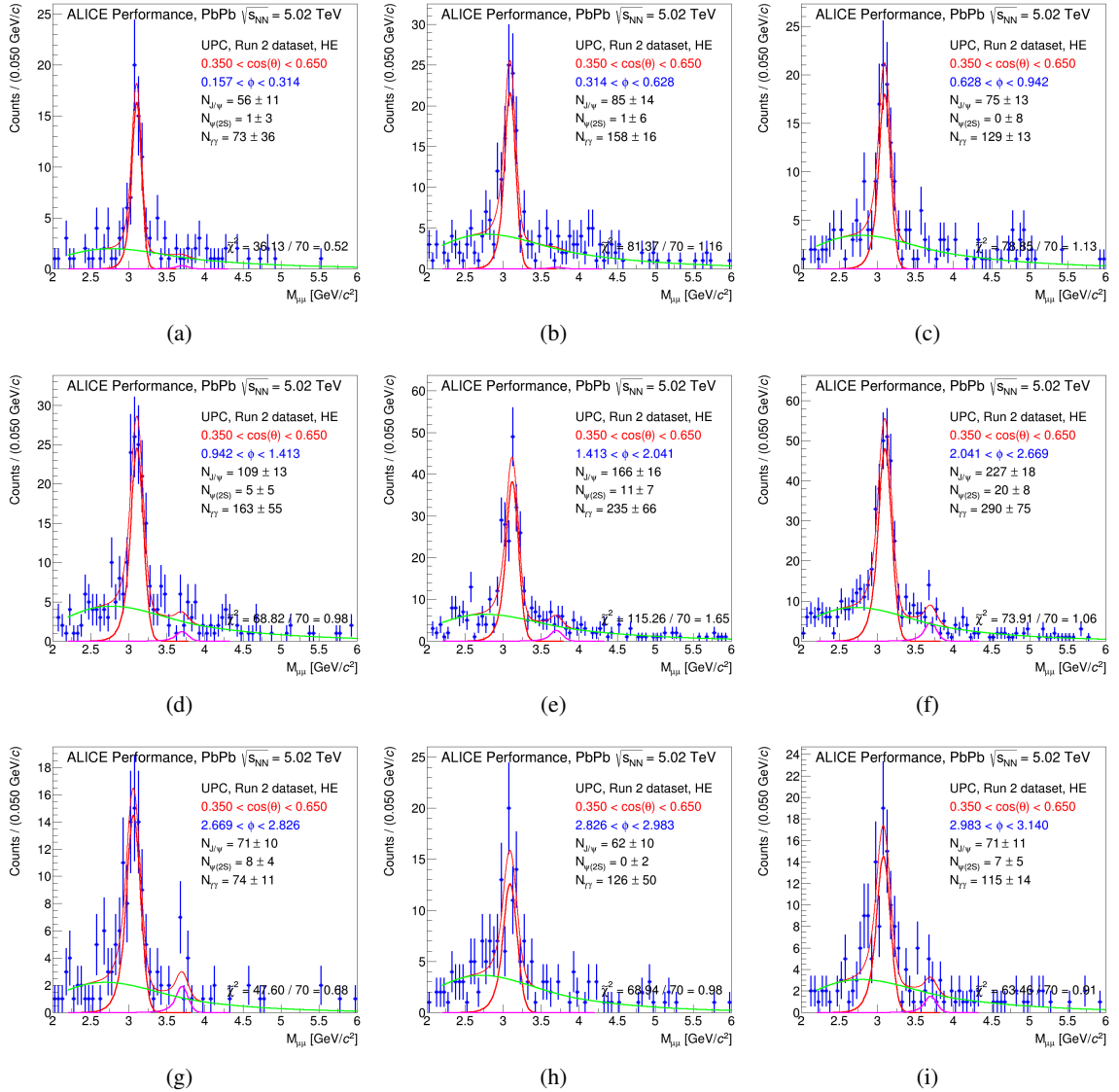


Fig. A.19: Signal extraction in the (+0.35, +0.65) bin in $\cos \theta$. From the upper left to the lower right panel, increasing bin in ϕ , from 11 to 19.

376 B Invariant Mass Fits for 2D signal extraction in the Collins-Soper frame

377 The joint $(\cos \theta, \phi)$ distribution has also been fitted in the Collins-Soper frame, using variable binning as
 378 in the case of the 2D helicity frame analysis (Appendix A). The bin boundaries are given below:

$$\begin{aligned} \cos \theta = & -0.65, -0.35, -0.15, -0.05, 0.05, 0.15, 0.35, 0.65; \\ \phi / (0.05 \times 3.14) = & -20, -19, -18, -17, -13, -9, -6, -4, -2, -1, 0, \\ & +1, +2, +4, +6, +9, +13, +17, +18, +19, +20. \end{aligned} \quad (\text{B.1})$$

379 The raw distribution is shown in Fig. B.1, the $A \times \epsilon$ correction in Fig. B.5, and the $A \times \epsilon$ corrected
 380 distribution in Fig. B.2. As in the case of the helicity frame, there are sparsely populated bins where
 381 large fluctuations can occur.

382 These distributions were fitted using both the ROOT and the native MINUIT macros. We note that the
 383 corrected distributions are asymmetric in ϕ for larger negative values of $\cos \theta$, probably because of bin
 384 fluctuations since these zones are sparsely populated. In order to investigate the effect of this, several
 385 different fitting ranges were tried. It is possible to restrict the range for a given $\cos \theta$ (or ϕ) in both ROOT
 386 and MINUIT approaches, while in addition specific $(\cos \theta, \phi)$ bins can be omitted in the MINUIT code.

387 The most satisfactory fits turn out to be the ones that can be performed with both methods. Having
 388 verified that for the same fitted range both codes give almost identical answers, we show (in the ROOT
 389 fit) a fit for $-0.35 \leq \cos \theta \leq 0.6$ (Fig. B.3), while the MINUIT fit in Fig. B.4 shows the result for the full
 390 available range, $(-0.6 \leq \cos \theta \leq 0.6)$. The parameters obtained are given in Table B.1.

Table B.1: Results from the fits for the 2D Collins-Soper frame for different angular ranges.

	λ_θ	λ_ϕ	$\lambda_{\theta\phi}$	χ^2/NDF
ROOT $-0.35 \leq \cos \theta \leq 0.6$	1.044 ± 0.165	0.002 ± 0.014	0.248 ± 0.033	1.46
TMinuit $-0.35 \leq \cos \theta \leq 0.6$	1.044 ± 0.165	0.002 ± 0.014	0.248 ± 0.033	1.47
TMinuit all bins	0.776 ± 0.125	-0.008 ± 0.014	0.086 ± 0.028	2.20
TMinuit $\cos \theta < -0.35$ $+0.314 < \phi < +0.942$ removed	0.964 ± 0.132	-0.001 ± 0.014	0.131 ± 0.029	2.03

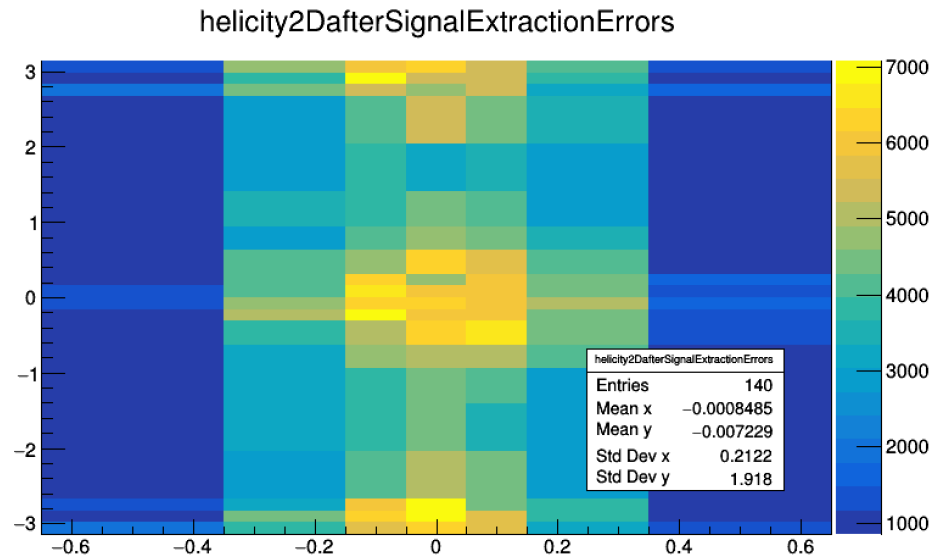


Fig. B.1: The raw distribution before correction. The x -axis shows the $\cos \theta$, while the y -axis the ϕ .

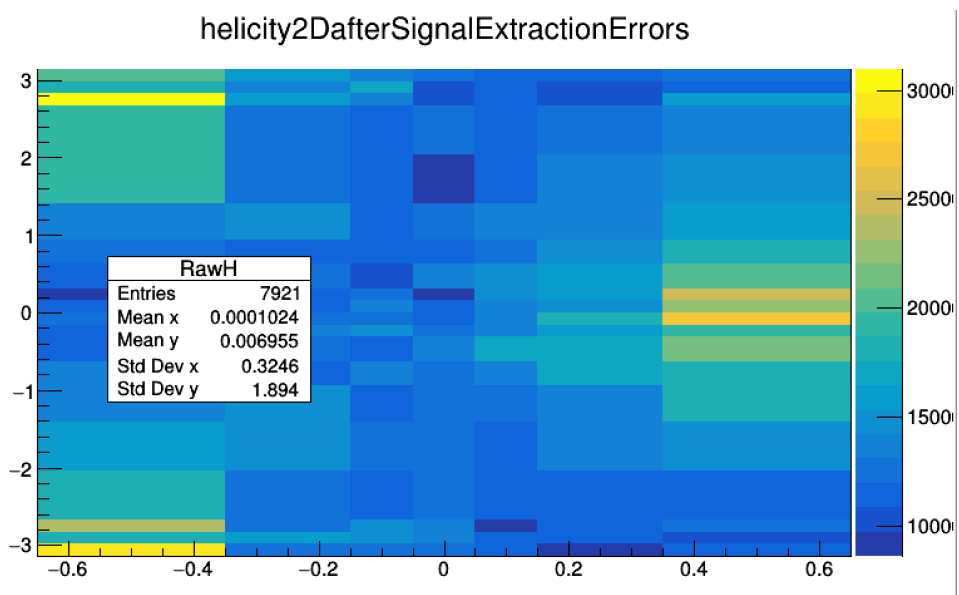


Fig. B.2: The $A \times \epsilon$ corrected 2D distribution.

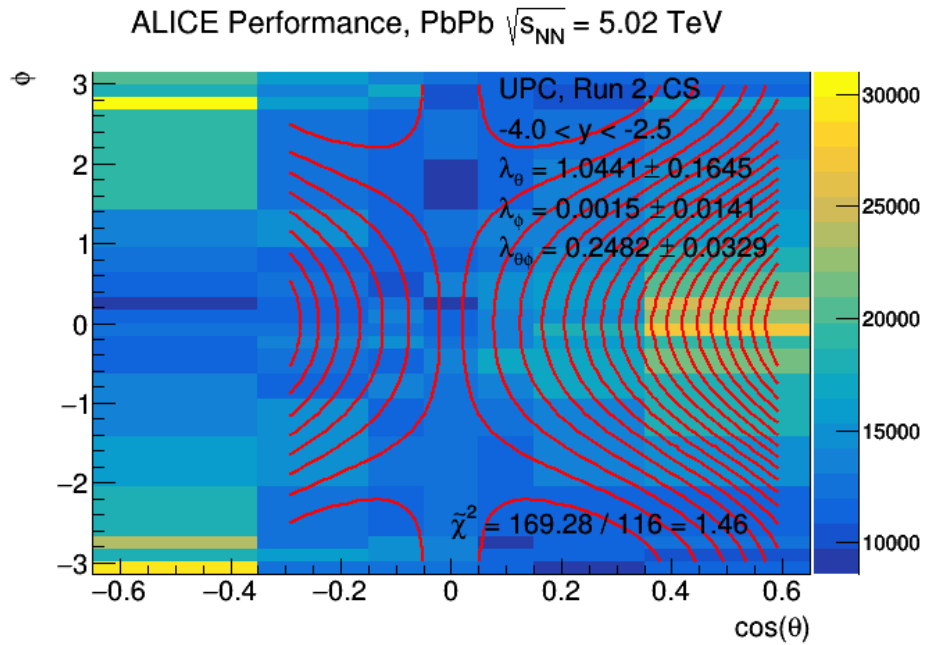


Fig. B.3: The ROOT fit to the 2D distribution.

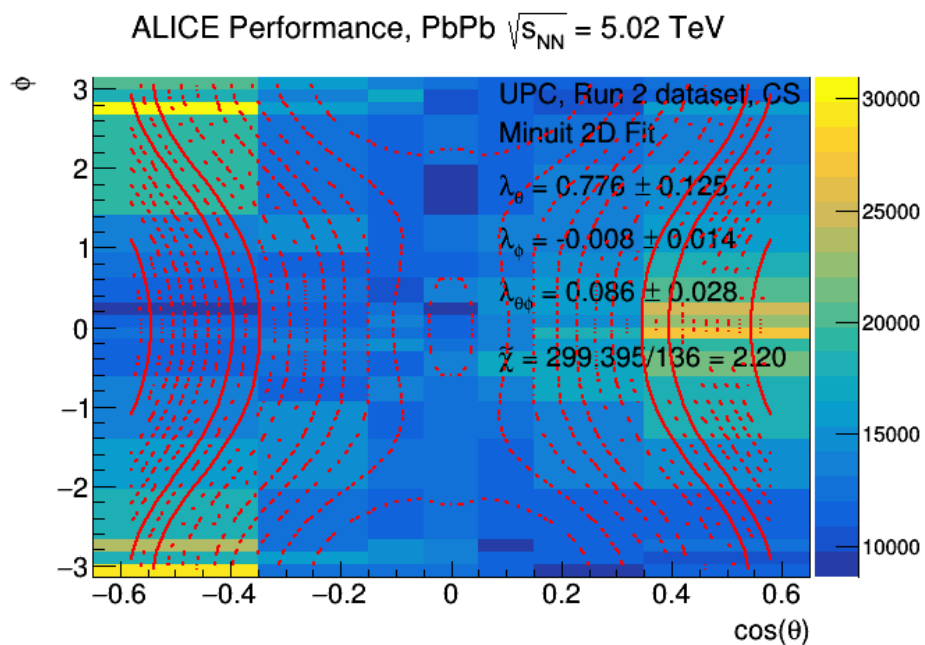


Fig. B.4: The Minuit fit to the 2D distribution.

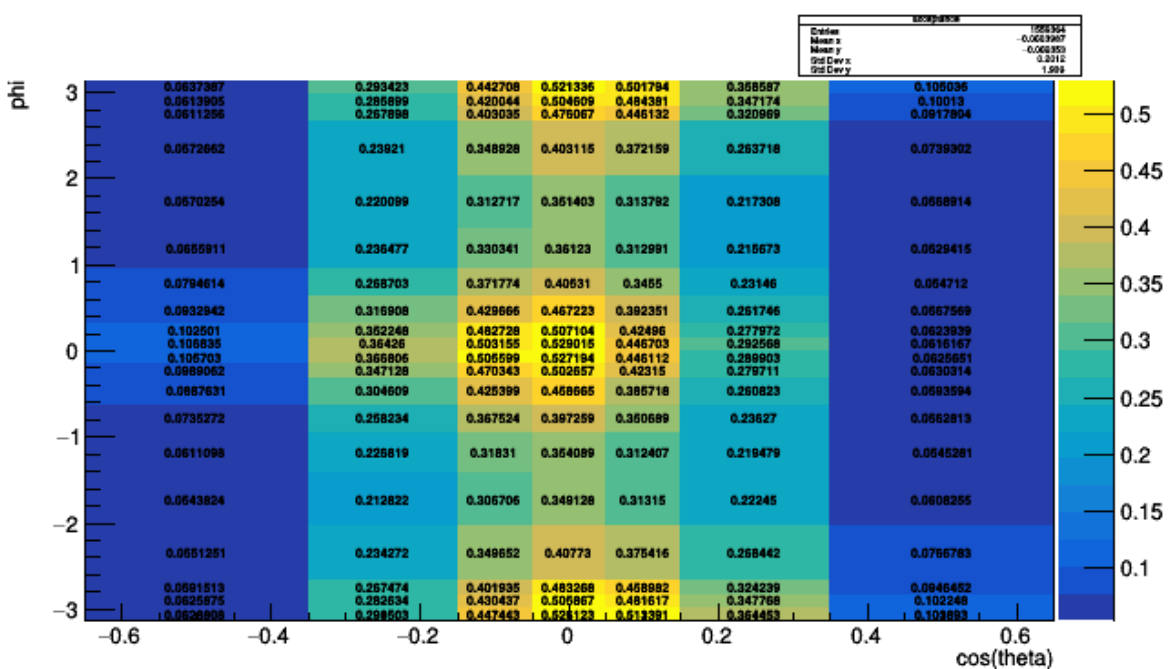


Fig. B.5: The $A \times \epsilon$ for the 2D distribution.

391 B.1 Yield extraction for the 2D analysis

392 The yields used in this 2D analysis, along with the $\cos \theta$ and ϕ bins they refer to, are shown in Figs. B.6,
 393 B.7, B.8, B.9, B.10, B.11, B.12, B.13, B.14, B.15, B.16, B.17, B.18, B.19.

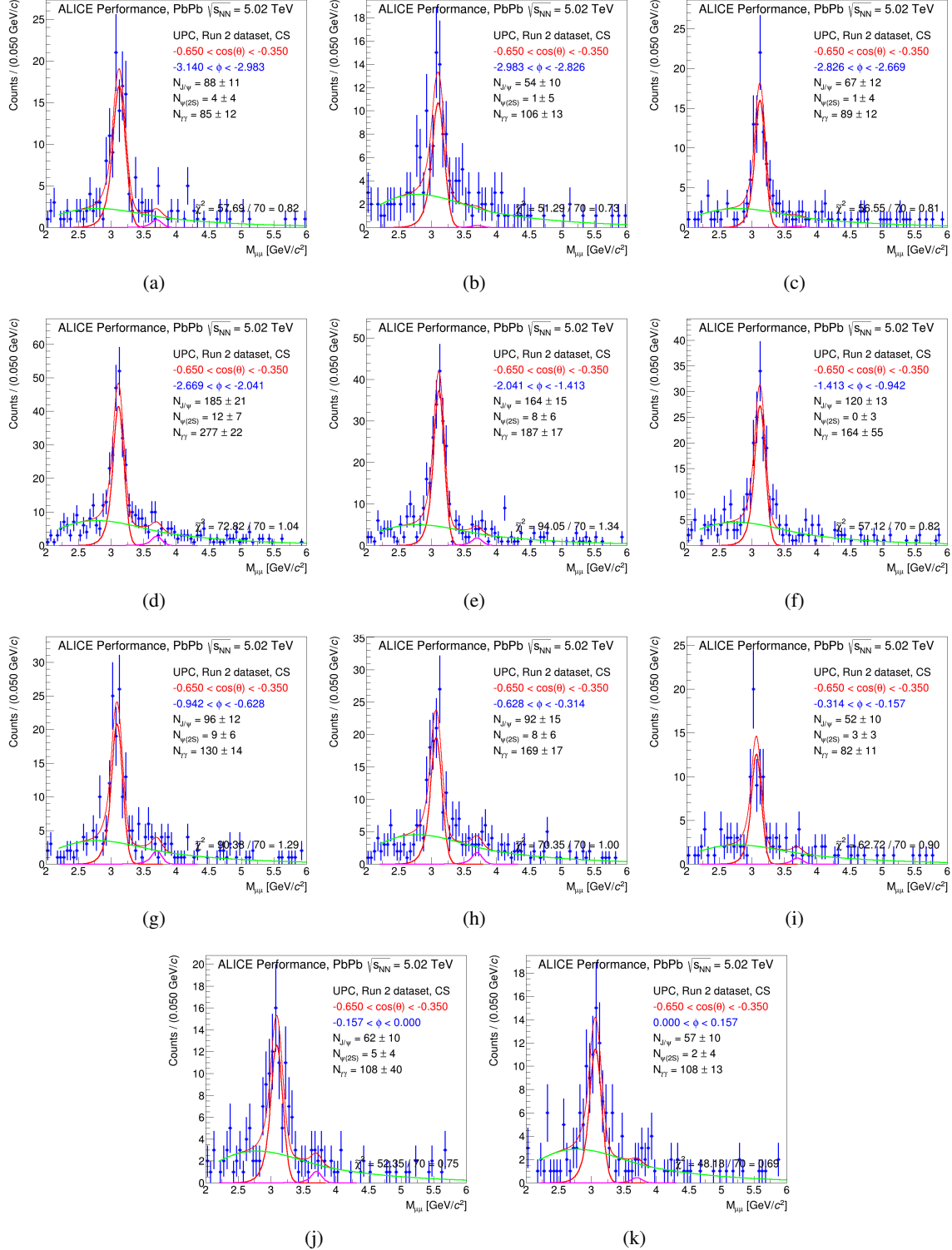


Fig. B.6: Signal extraction in the $(-0.65, -0.35)$ bin in $\cos \theta$. From the upper left to the lower right panel, increasing bin in ϕ , from 0 to 10.

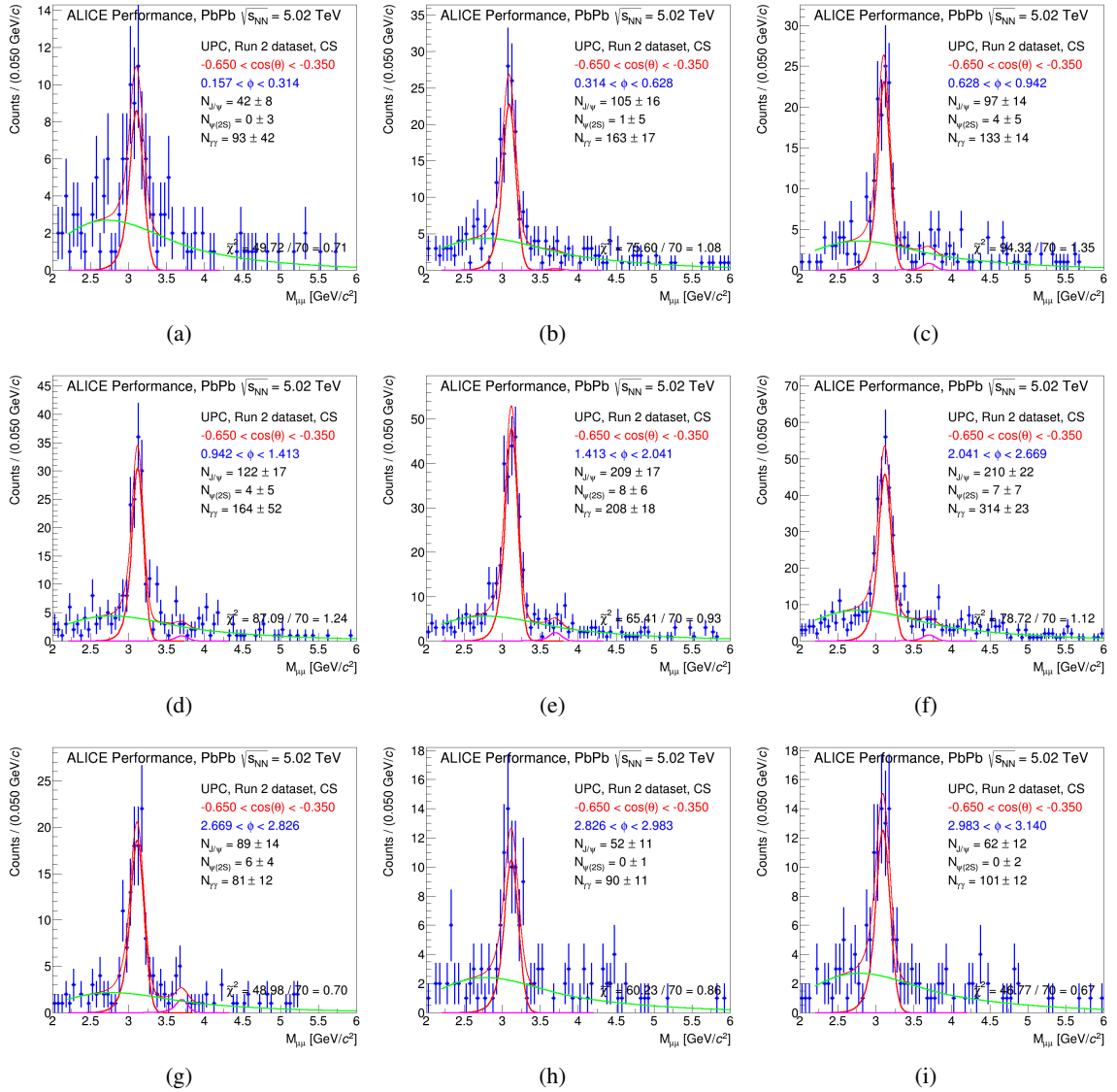


Fig. B.7: Signal extraction in the (-0.65, -0.35) bin in $\cos \theta$. From the upper left to the lower right panel, increasing bin in ϕ , from 11 to 19.

394 The purpose of the 2D fits is to serve a consistency check for the 1D fits, which constitute the primary
 395 results of the analysis. Consistency for the same angular region is demonstrated for both the helicity
 396 and the Collins-Soper measurements. For the Collins-Soper analysis an apparent asymmetry at larger
 397 negative $\cos \theta$ values (even after $A \times \varepsilon$ correction) leads to a larger χ^2/NDF than that obtained for the
 398 helicity axis case. This can be improved by restricting the range in $\cos \theta$, but this tends to increase the
 399 $\lambda_{\theta\phi}$ value somewhat. The conclusion is that the 2D analysis supports the 1D analysis.

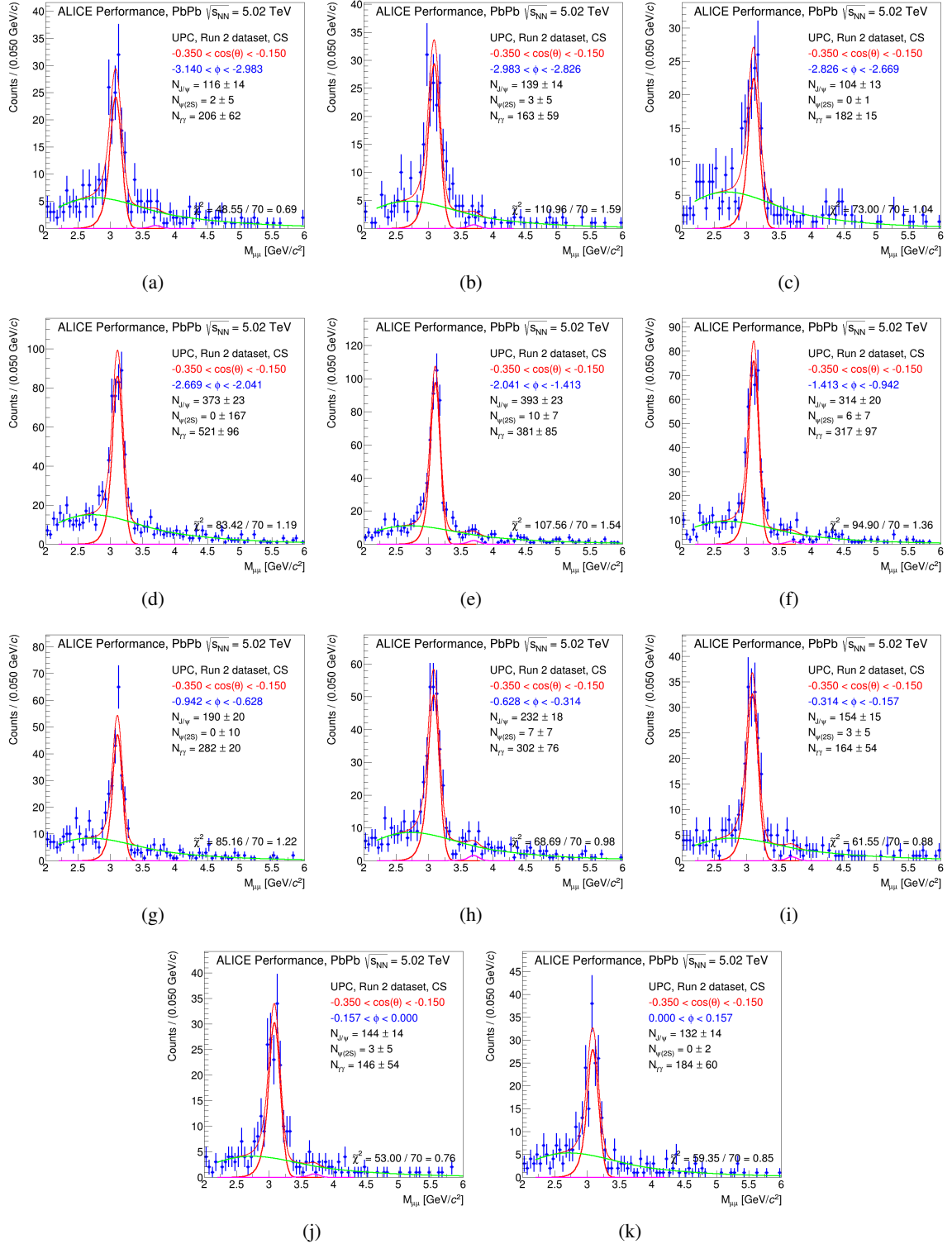


Fig. B.8: Signal extraction in the $(-0.35, -0.15)$ bin in $\cos \theta$. From the upper left to the lower right panel, increasing bin in ϕ , from 0 to 10.

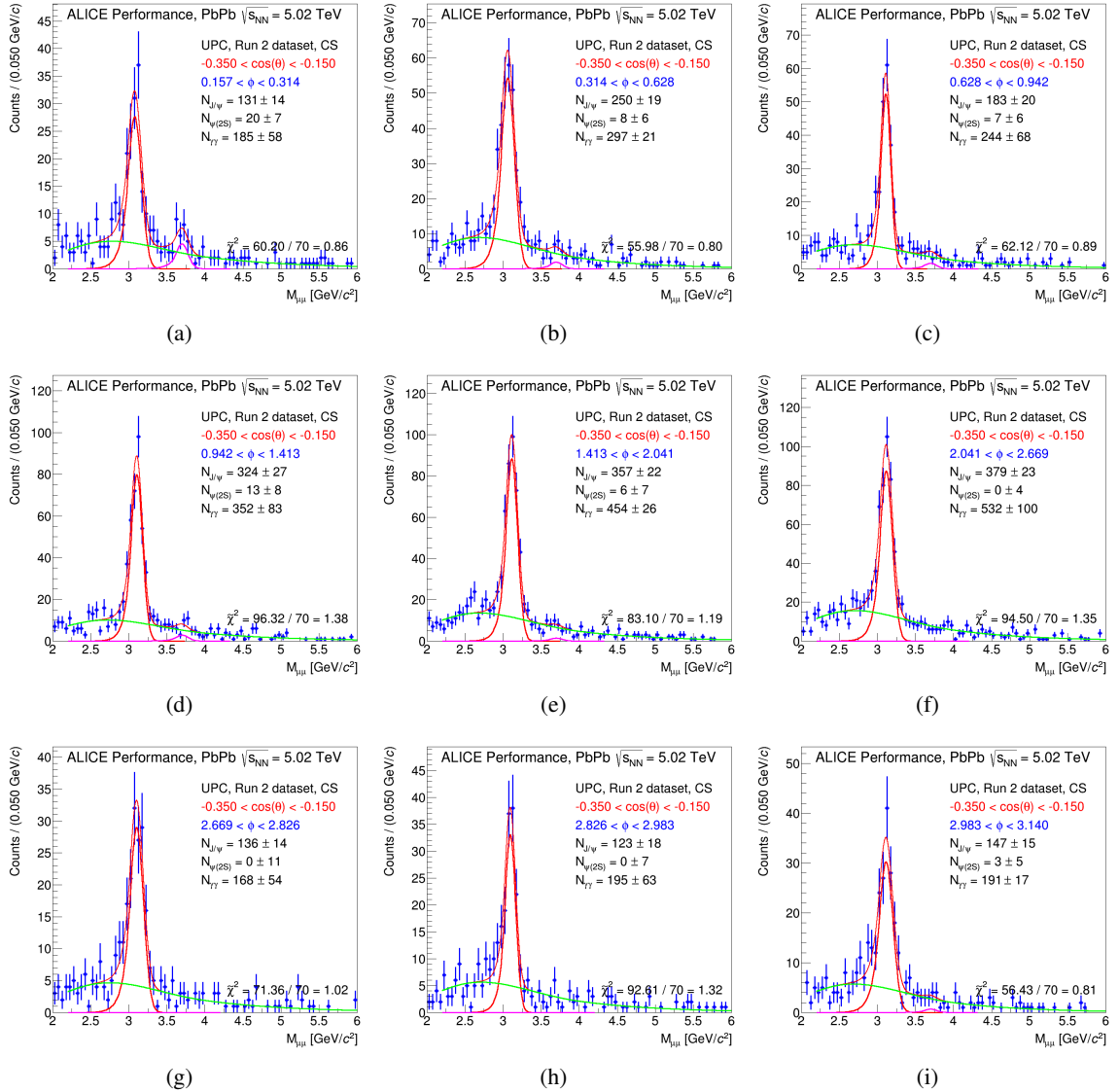


Fig. B.9: Signal extraction in the $(-0.35, -0.15)$ bin in $\cos \theta$. From the upper left to the lower right panel, increasing bin in ϕ , from 11 to 19.

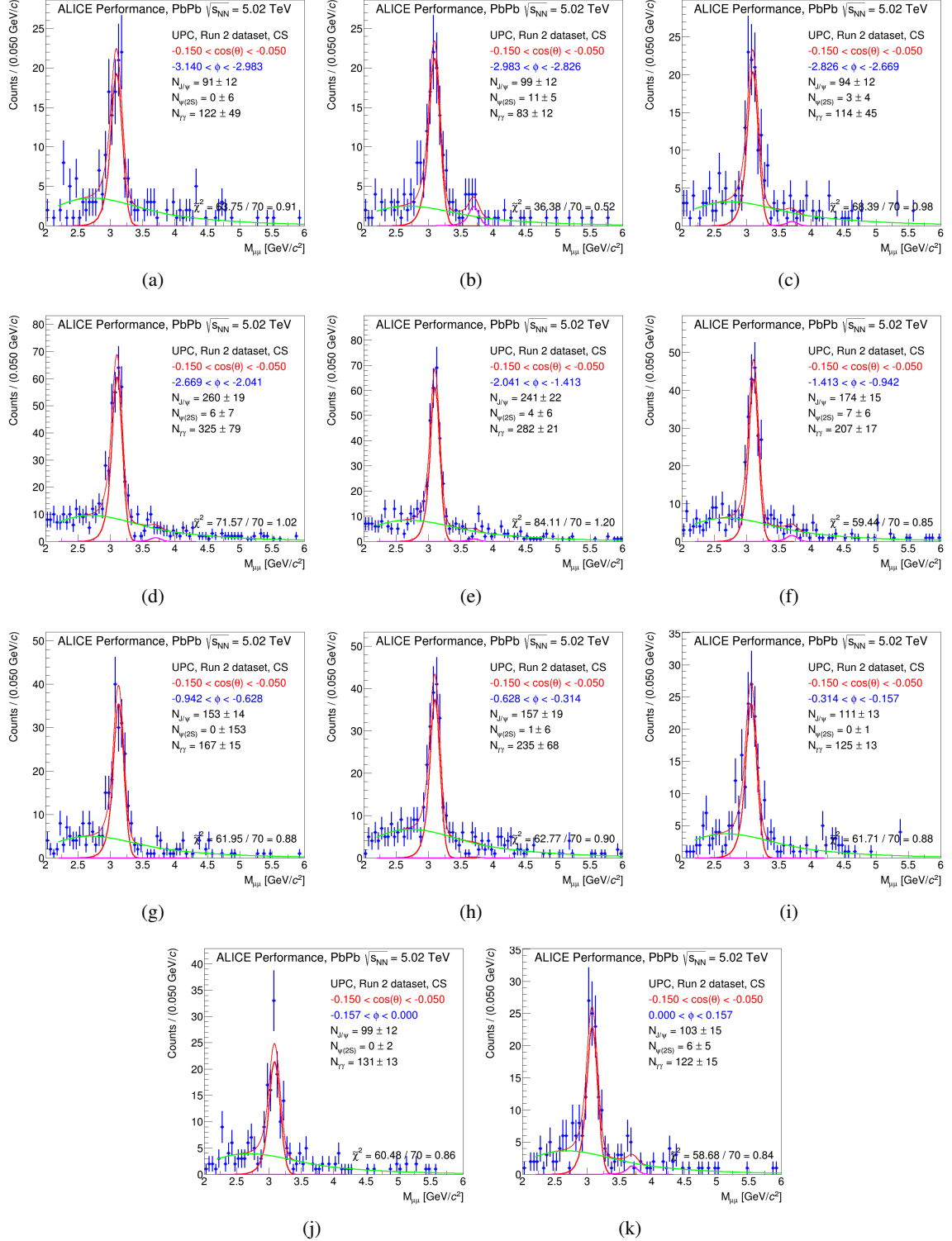


Fig. B.10: Signal extraction in the (-0.15, -0.05) bin in $\cos \theta$. From the upper left to the lower right panel, increasing bin in ϕ , from 0 to 10.

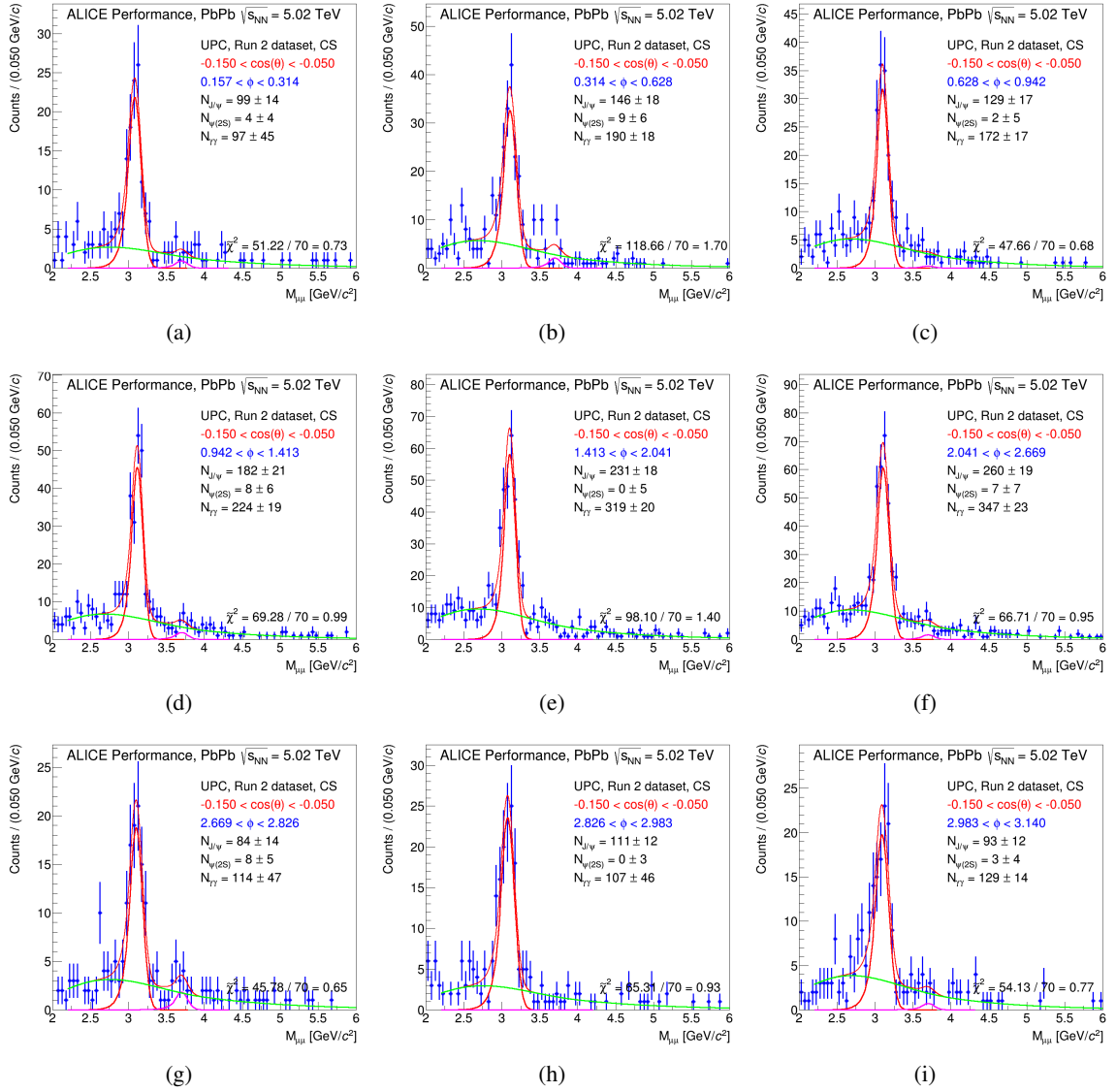


Fig. B.11: Signal extraction in the (-0.15, -0.05) bin in $\cos \theta$. From the upper left to the lower right panel, increasing bin in ϕ , from 11 to 19.

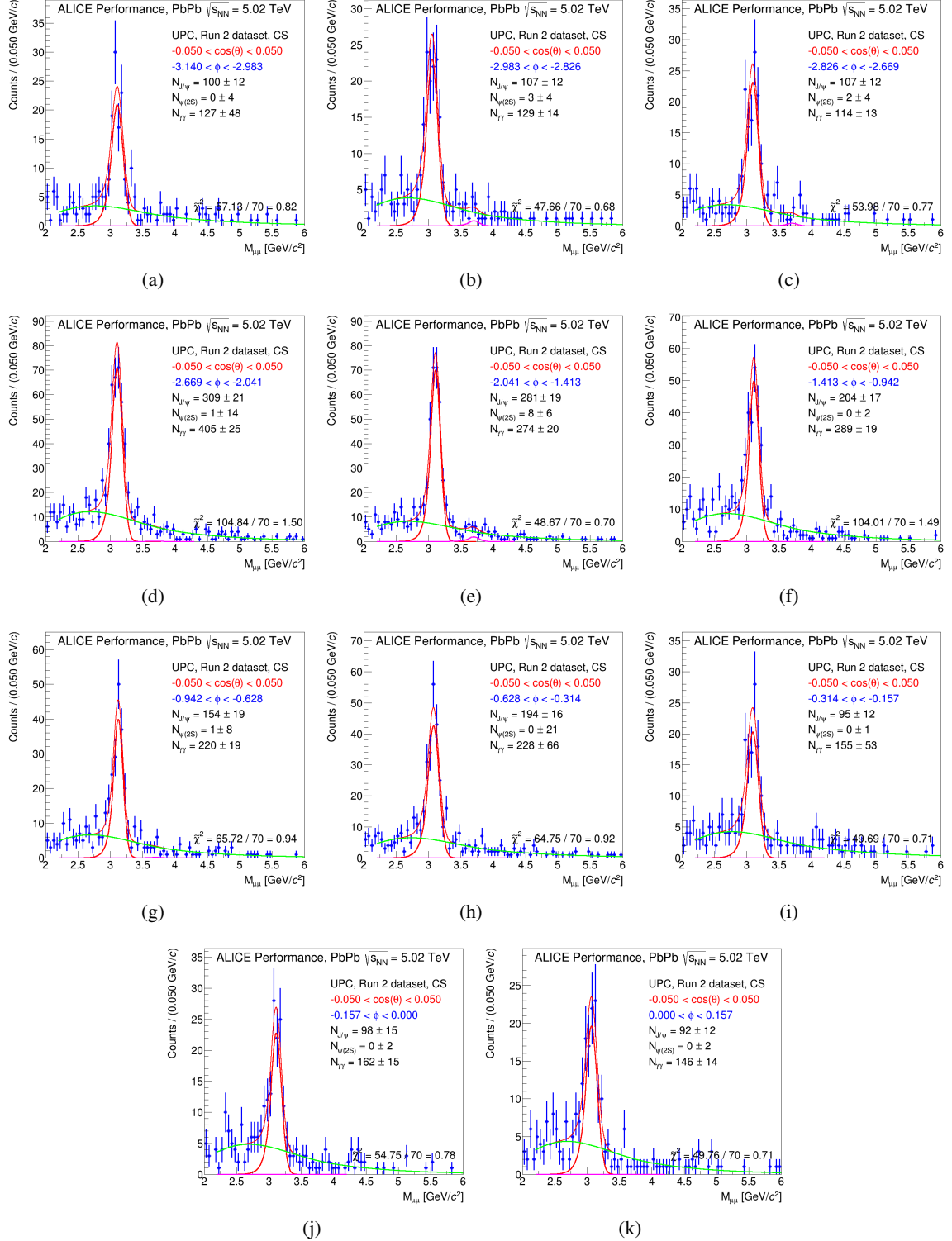


Fig. B.12: Signal extraction in the (-0.05, +0.05) bin in $\cos\theta$. From the upper left to the lower right panel, increasing bin in ϕ , from 0 to 10.

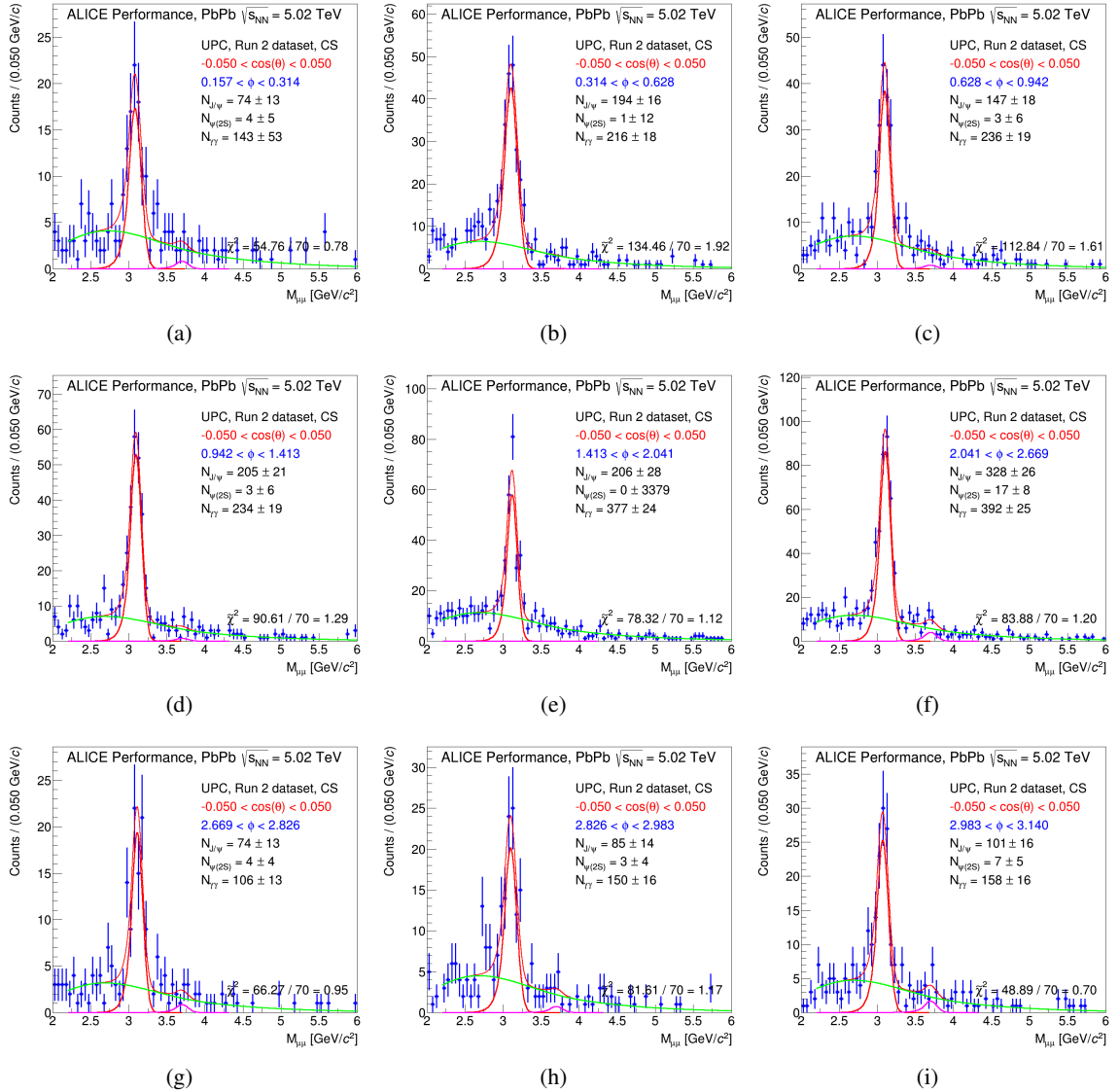


Fig. B.13: Signal extraction in the (-0.05, +0.05) bin in $\cos\theta$. From the upper left to the lower right panel, increasing bin in ϕ , from 11 to 19.

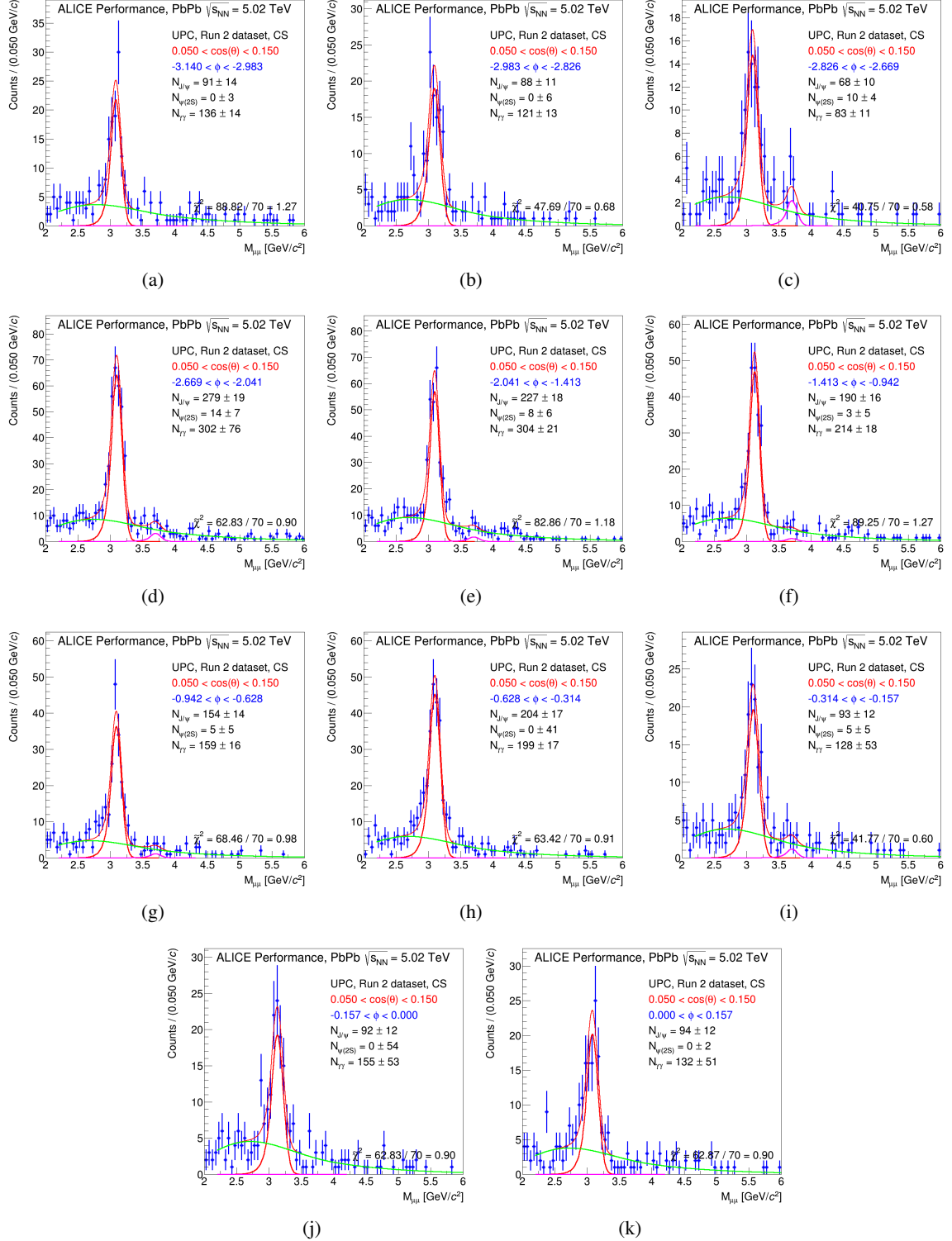


Fig. B.14: Signal extraction in the $(+0.05, +0.15)$ bin in $\cos \theta$. From the upper left to the lower right panel, increasing bin in ϕ , from 0 to 10.

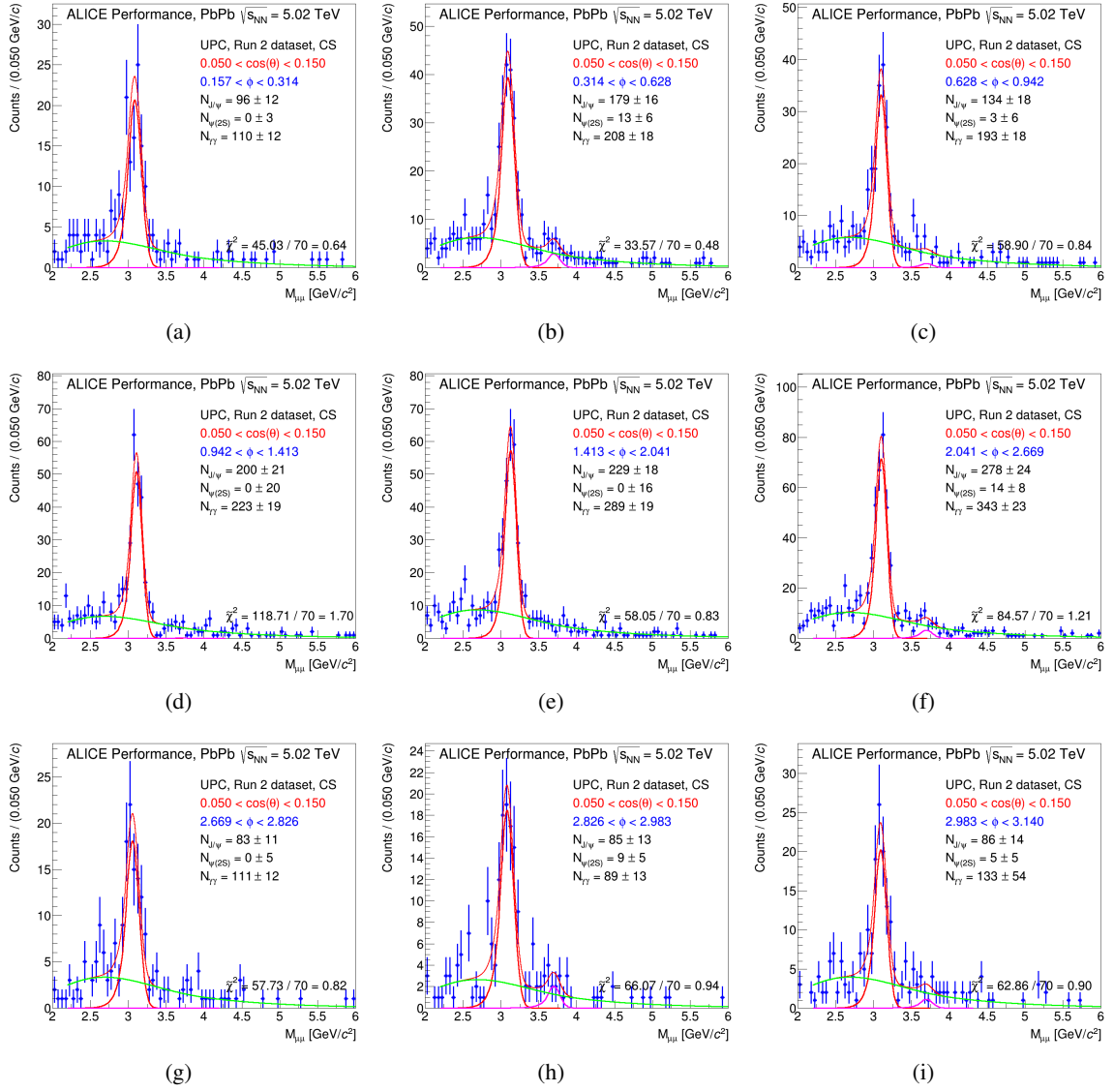


Fig. B.15: Signal extraction in the (+0.05, +0.15) bin in $\cos \theta$. From the upper left to the lower right panel, increasing bin in ϕ , from 11 to 19.

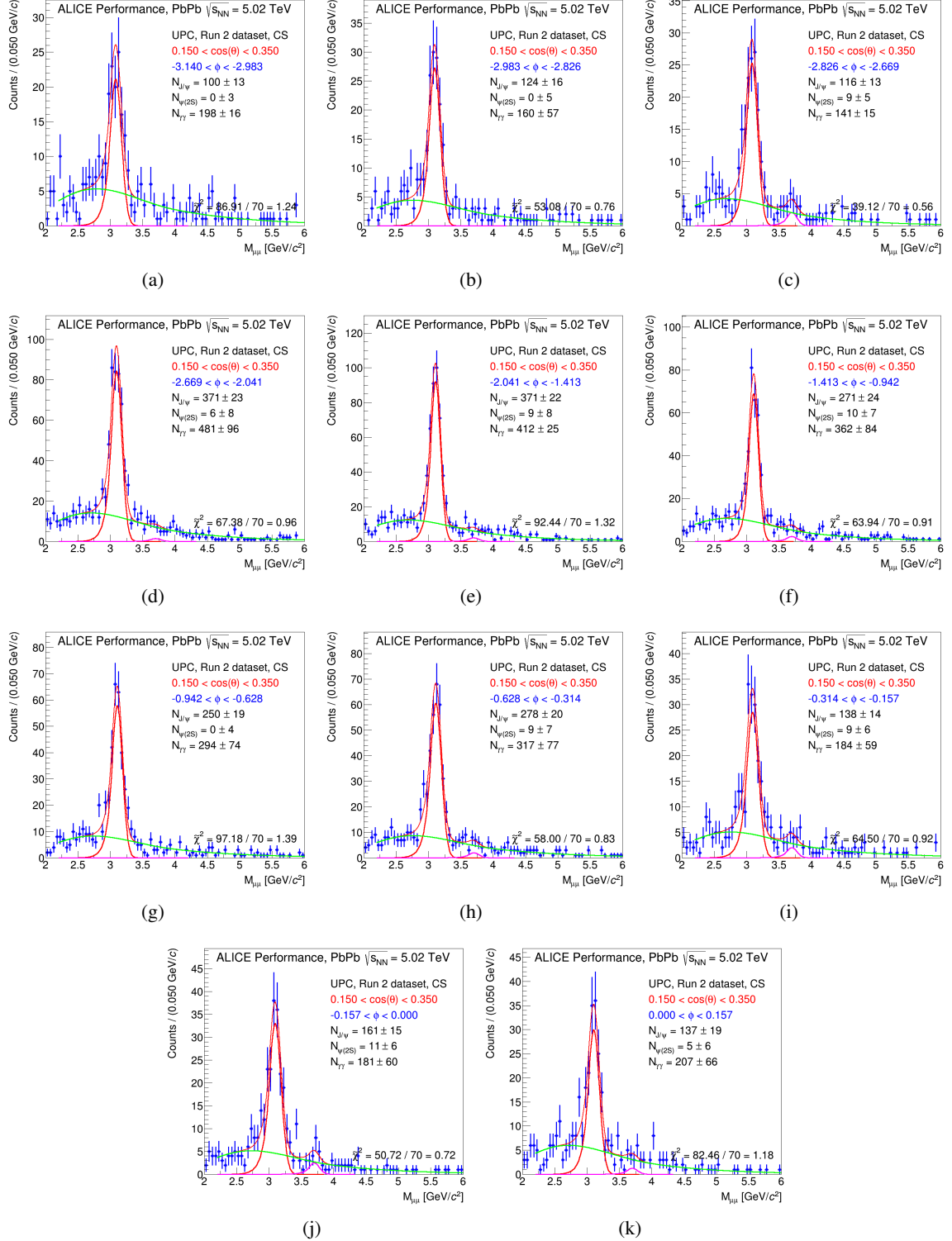


Fig. B.16: Signal extraction in the $(+0.15, +0.35)$ bin in $\cos \theta$. From the upper left to the lower right panel, increasing bin in ϕ , from 0 to 10.

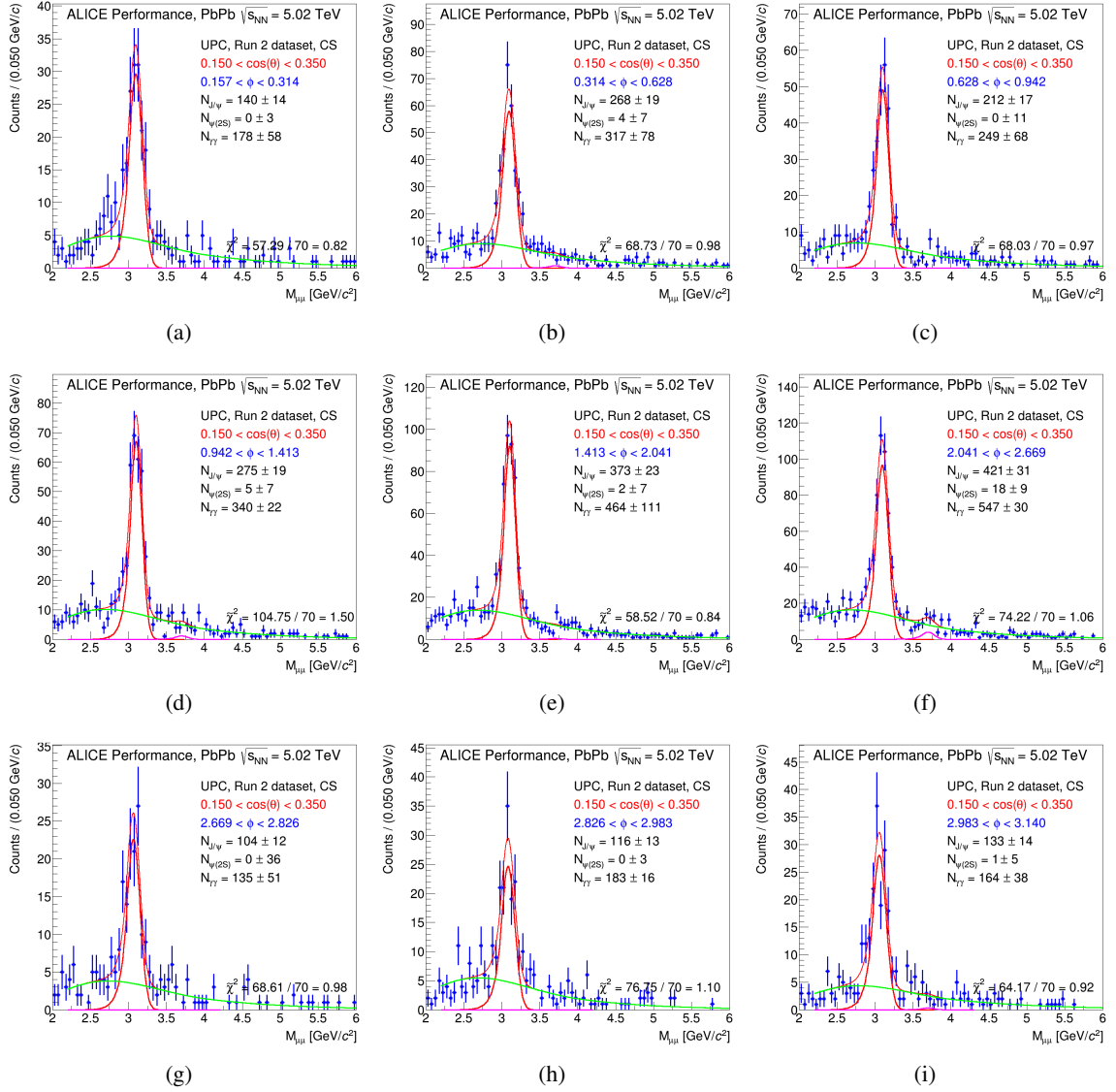


Fig. B.17: Signal extraction in the (+0.15, +0.35) bin in $\cos \theta$. From the upper left to the lower right panel, increasing bin in ϕ , from 11 to 19.

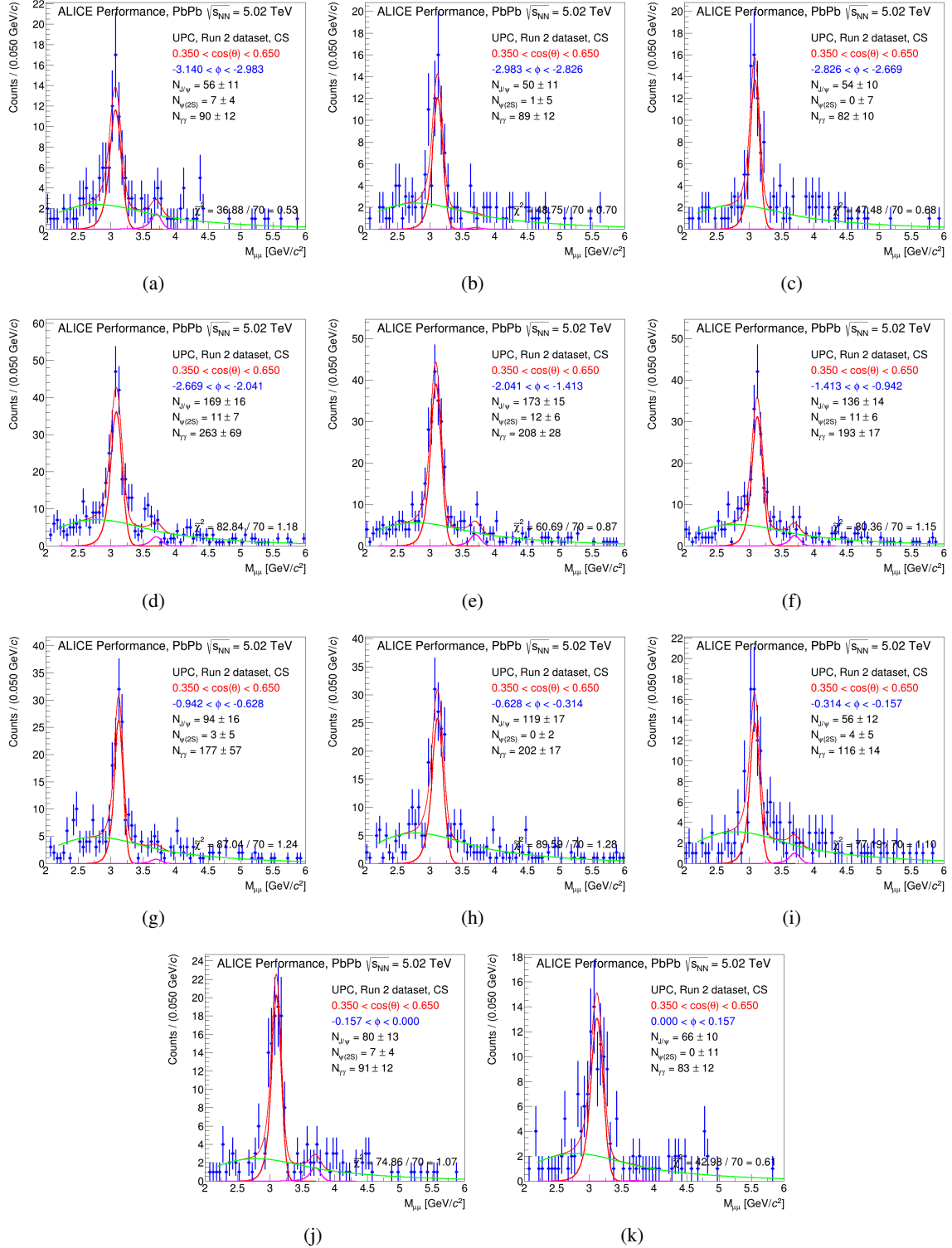


Fig. B.18: Signal extraction in the $(+0.35, +0.65)$ bin in $\cos\theta$. From the upper left to the lower right panel, increasing bin in ϕ , from 0 to 10.

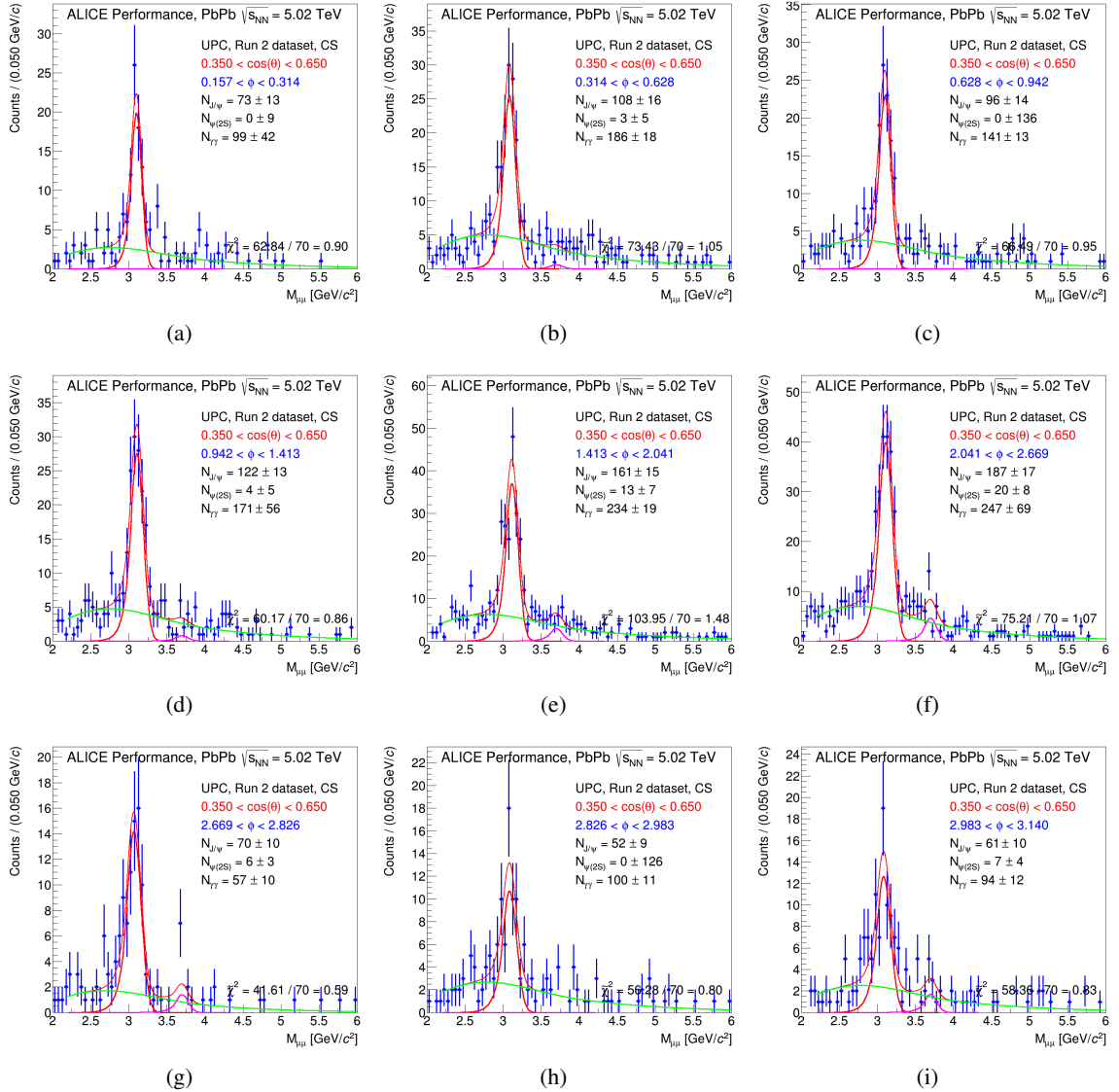


Fig. B.19: Signal extraction in the (+0.35, +0.65) bin in $\cos \theta$. From the upper left to the lower right panel, increasing bin in ϕ , from 11 to 19.

400 References

- [1] J. G. Contreras and J. D. Tapia Takaki. *Ultra-peripheral heavy-ion collisions at the LHC*. *International Journal of Modern Physics A*, 30:1542012–393, March 2015.
- [2] ALICE Collaboration, A. Shreyasi, et al. *Coherent J/Ψ photoproduction at forward rapidity in ultra-peripheral Pb-Pb collisions at $\sqrt{s_{\text{NN}}} = 5.02 \text{ TeV}$* . *arXiv preprint arXiv:1904.06272*, 2019.
- [3] Pietro Faccioli, Carlos Lourenço, Joao Seixas, and Hermine K. Wohri. Towards the experimental clarification of quarkonium polarization. *Eur. Phys. J.*, C69:657–673, 2010.
- [4] Pietro Faccioli, Carlos Lourenco, and Joao Seixas. A New approach to quarkonium polarization studies. *Phys. Rev.*, D81:111502, 2010.
- [5] Livio Bianchi. *J/ψ polarization in pp collisions at $\sqrt{s} = 7 \text{ TeV}$ with the ALICE muon spectrometer at the LHC*, Mar 2012. Presented 06 Mar 2012.
- [6] John Erthal Gaiser. Charmonium Spectroscopy From Radiative Decays of the J/Ψ and Ψ'. Technical report, 1982.